Simon Kersten

Modeling and analysis of vibroacoustic mechanisms in hearing

IHTA **Institute for Hearing Technology and Acoustics**

RWTHAACHEN UNIVERSITY

Modeling and analysis of vibroacoustic mechanisms in hearing

Von der Fakultät für Elektrotechnik und Informationstechnik der
Rheinisch-Westfälischen Technischen Hochschule Aachen
zur Erlangung des akademischen Grades eines

DOKTORS DER INGENIEURWISSENSCHAFTEN

genehmigte Dissertation

vorgelegt von

M.Sc.
Simon Kersten

aus Goch, Deutschland

Berichter:

Universitätsprofessor Dr. rer. nat. Michael Vorländer
Professor Dr. rer. nat. Bastian Epp

Tag der mündlichen Prüfung: 1. August 2025

Diese Dissertation ist auf den Internetseiten der Universitätsbibliothek online
verfügbar.

All models are wrong, but some are useful.
George E. P. Box

Abstract

Despite significant technological advancements in recent decades, users of hearing aids and hearing protection often report dissatisfaction due to an "unnatural" auditory experience. These challenges highlight gaps in our understanding of the physical mechanisms underlying hearing – a complex vibroacoustic phenomenon involving interactions between the sound field in the outer ear, the mechanics of the middle ear, and the fluid dynamics of the inner ear. Hearing not only involves the air conduction (AC) pathway via the outer and middle ear, but also various bone conduction (BC) pathways via which sound is transmitted to the inner ear. BC hearing plays a crucial role in audiological applications such as BC audiometry and BC hearing aids, where vibrations are directly induced in the skull. Another phenomenon involving both AC and BC is the occlusion effect (OE): occluding the ear canal (EC) alters own-voice perception, which is a major cause of the dissatisfaction with hearing technologies.

Experimentally assessing the physics underlying hearing poses significant ethical and technical difficulties. Therefore, modeling and numerical simulations are essential tools for advancing our understanding. These investigations also require examining the vibroacoustic behavior of the inner ear, because it serves as the sensor for all AC and BC pathways. Recent studies challenge the classical view on inner ear mechanics by highlighting the flexibility of the cochlear partition (CP), particularly the osseous spiral lamina (OSL) and cochlear partition bridge (CPB). The roles of these structures are poorly understood, because experimental data on CP motion remain sparse and spatially limited and most inner ear models consider the OSL and CPB rigid.

This thesis advances our understanding of the vibroacoustic mechanisms in AC and BC hearing by systematically separating the auditory system into subsystems. First, the structural motion of the EC is analyzed, with particular emphasis on how the motions of the EC entrance and tympanic membrane interact with the vibrations of the EC wall in generating the EC sound pressure underlying the OE. An impedance boundary condition is introduced to account for these contributions in OE models. Circuit calculations, based on an EC motion extracted from a finite element model of a human head, reveal that the motions of the EC entrance and tympanic membrane affect the EC sound pressure

at low frequencies, especially under occluded conditions. This finding may help reconcile discrepancies between OE simulations and experimental data.

Second, an anatomical finite element model of the human inner ear is introduced, allowing the OSL and CPB to be modeled as either rigid or flexible structures. When applying stimulation at the oval window – representing AC and BC transmission via this pathway – the simulations reveal that the OSL significantly influences cochlear impedances, CP stiffness, and overall CP motion. Furthermore, when incorporating the rigid body motion of the inner ear during BC, the simulations identify a compressional motion of the OSL that increases the differential volume velocity at the round window compared the oval window, offering an alternative explanation for experimental observations previously attributed to "third-window" effects in BC hearing. These findings highlight the importance of considering the flexibility of the OSL and CPB when interpreting experimental data, challenging classical concepts of inner ear function that assume a rigid OSL and neglect the CPB. Overall, the results suggest that the OSL plays a more important role in both AC and BC hearing than previously recognized.

While this work advances our understanding of hearing by focusing separately on different auditory subsystems, future work should integrate these insights into comprehensive models, such as full-head finite element simulations, to further elucidate the interactions between the AC and BC pathways and their relative importance. Ultimately, these findings will contribute to improvements in hearing technologies, including hearing devices, hearing protection, and BC hearing aids.

Kurzfassung

Trotz bedeutender technologischer Fortschritte in den letzten Jahrzehnten berichten Nutzer von Hörgeräten und Gehörschutz häufig von Unzufriedenheit aufgrund eines „unnatürlichen" Hörerlebnisses. Diese Herausforderungen verdeutlichen Lücken in unserem Verständnis der physikalischen Mechanismen, die dem Hören zugrunde liegen – ein komplexes vibroakustisches Phänomen mit Wechselwirkungen zwischen dem Schallfeld im Außenohr, der Mechanik des Mittelohrs und der Fluiddynamik des Innenohrs. Hören umfasst nicht nur den Luftschallpfad über Außen- und Mittelohr, sondern auch verschiedene Knochenschallpfade, über die Schall zum Innenohr übertragen wird. Knochenschall spielt eine wichtige Rolle in audiologischen Anwendungen wie der Knochenleitungsaudiometrie und Knochenschallhörgeräten, bei denen Schwingungen direkt in den Schädel eingeleitet werden. Ein weiteres Phänomen, das sowohl Luft- als auch Knochenschall beinhaltet, ist der Okklusionseffekt (OE): Das Verschließen des Gehörgangs verändert die Wahrnehmung der eigenen Stimme, was eine der Ursachen für die Unzufriedenheit mit Hörtechnologien ist.

Die experimentelle Untersuchung der zugrundeliegenden Physik des Hörens ist mit erheblichen ethischen und technischen Schwierigkeiten verbunden. Daher sind Modellierung und numerische Simulationen unverzichtbare Werkzeuge, um unser Verständnis zu verbessern. Diese Untersuchungen erfordern auch die Charakterisierung des vibroakustischen Verhaltens des Innenohrs, da es als Sensor für alle Luft- und Knochenschallpfade dient. Jüngste Studien stellen die klassische Sichtweise auf die Innenohrmechanik in Frage, indem sie die Flexibilität der cochleären Trennwand (engl. cochlear partition, CP) hervorheben, insbesondere von Lamina Spiralis (engl. osseous spiral lamina, OSL) und Brückenstruktur (engl. cochlear partition bridge, CPB). Die Funktionen dieser Strukturen sind kaum verstanden, da experimentelle Daten zur Bewegung der CP nach wie vor spärlich und räumlich begrenzt sind und die meisten Innenohrmodelle die OSL und die CPB als starr betrachten.

Diese Arbeit erweitert unser Verständnis der vibroakustischen Hörmechanismen beim Luft- und Knochenschall, indem sie das Gehör systematisch in Teilsysteme unterteilt. Zunächst wird die Schwingung des Gehörgangs analysiert, wobei ein besonderer Schwerpunkt auf der Wechselwirkung zwischen den Bewegungen

des Eingangs und des Trommelfells mit den Schwingungen der Gehörgangswand bei der Erzeugung des Schalldrucks im Gehörgang liegt, der dem OE zugrunde liegt. Eine Impedanzrandbedingung wird eingeführt, um diese Beiträge in Modellen des OEs zu berücksichtigen. Ersatzschaltbildberechnungen, basierend auf der Gehörgangsbewegung eines Finite-Elemente-Modells des menschlichen Kopfes, zeigen, dass die Bewegungen des Eingangs und des Trommelfells den Gehörgangsschalldruck bei niedrigen Frequenzen beeinflussen, insbesondere im verschlossenen Fall. Diese Erkenntnisse können dazu beitragen, Diskrepanzen zwischen Simulationen des OEs und experimentellen Daten zu erklären.

Anschließend wird ein anatomisches Finite-Elemente-Modell des menschlichen Innenohrs eingeführt, mit dem OSL und CPB entweder als starre oder als flexible Strukturen modelliert werden können. Bei einer Anregung am ovalen Fenster, welche die Luft- und Knochenschallpfade über diesen Weg repräsentiert, zeigen die Simulationen, dass die OSL einen signifikanten Einfluss auf die Innenohrimpedanzen, die Steifigkeit der CP und die gesamte Bewegung der CP hat. Darüber hinaus identifizieren die Simulationen bei Einbeziehung der Starrkörperbewegung des Innenohrs während des Knochenschalls eine Kompressionsbewegung der OSL, die den differentiellen Schallfluss am runden Fenster im Vergleich zum ovalen Fenster erhöht. Dies bietet eine alternative Erklärung für experimentelle Beobachtungen, die zuvor „Dritte-Fenster"-Effekten beim Knochenschall zugeschrieben wurden. Diese Ergebnisse unterstreichen, wie wichtig es ist, die Flexibilität von OSL und CPB bei der Interpretation experimenteller Daten zu berücksichtigen, und stellen klassische Konzepte zur Funktion des Innenohrs in Frage, welche von einer starren OSL ausgehen und die CPB vernachlässigen. Insgesamt deuten die Ergebnisse darauf hin, dass die OSL sowohl beim Luft- als auch beim Knochenschall eine wichtigere Rolle spielt als bisher angenommen.

Während diese Arbeit unser Verständnis des Hörens fördert, indem sie sich separat auf verschiedene Teilsysteme des Gehörs konzentriert, sollten zukünftige Arbeiten diese Erkenntnisse in umfassende Modelle integrieren, beispielsweise Finite-Elemente-Simulationen des gesamten Kopfes, um die Wechselwirkungen zwischen den Luft- und Knochenschallpfaden und ihre relative Bedeutung weiter aufzuklären. Letztendlich werden diese Erkenntnisse zu Verbesserungen in der Hörtechnologie beitragen, darunter Hörhilfen, Gehörschutz und Knochenschallhörgeräte.

Contents

1

Introduction

Hearing is a fundamental sense for human communication, allowing us to perceive and engage with those around us. Hearing loss presents a major barrier to this ability, affecting millions of people worldwide (Haile et al., 2021). For individuals with hearing impairment, hearing aids remain the most common and effective treatment (*World Report on Hearing* 2021). The choice of hearing aid depends on the type and degree of hearing loss. Air conduction (AC) hearing aids function by amplifying sound and transmitting it through the ear canal (EC) and middle ear (ME) to the inner ear (Dillon, 2012a), while bone conduction (BC) hearing aids directly stimulate the inner ear by exciting skull vibrations (Kompis and Caversaccio, 2011). Over the past decades, hearing aid technology has advanced considerably, leading to substantial improvements in performance and accessibility. As a result, more and more people are adopting hearing aids earlier in life, recognizing the clear benefits they provide in daily communication (*EuroTrack* 2020).

Advancements in hearing technologies are not limited to audiological applications. Modern "hearables" increasingly incorporate functionalities traditionally associated with hearing aids (Bennett et al., 2023; De Proost et al., 2024; Hammond and Diedesch, 2023), and BC headphones – which generate sound through structural vibrations in the head while leaving the EC open – are becoming increasingly popular as an alternative to conventional AC headphones and earbuds (Surendran et al., 2023).

Despite these advances, current hearing technology is still reaching its limitations. Although user dissatisfaction is due to various factors – including physiological, psychological, social and economic aspects (McCormack and Fortnum, 2013) – a frequently reported problem is the "unnatural" auditory experience, which affects both listening and speaking. Similar issues arise with hearing protection, where discomfort due to altered perception often leads workers to wear protective

devices incorrectly or not at all (Doutres et al., 2019). These challenges highlight gaps in our understanding of the physical mechanisms underlying hearing and require further research to improve device performance and user experience.

1.1 Vibroacoustic mechanisms in air and bone conduction hearing

When we listen, the sound field in the EC causes a mechanical motion of ME structures, which interact with the fluid dynamics within the inner ear to, ultimately, generate neural signals interpreted by the brain (Békésy, 1960). These complex interactions, illustrated by solid arrows in Figure 1.1, make AC hearing a fascinating vibroacoustic phenomenon. When we speak, the AC component – consisting of the sound transmission around the head and room reflections – is accompanied by internal sound transmission via the skull and surrounding tissue, such that the perception of one's own voice is a combination of AC and BC hearing (Pörschmann, 2000).

   Compared to AC, BC hearing adds even greater complexity, because it involves various vibroacoustic paths and mechanisms by which sound is transmitted towards the inner ear (Stenfelt, 2016; Stenfelt and Goode, 2005a; Taschke, 2005;
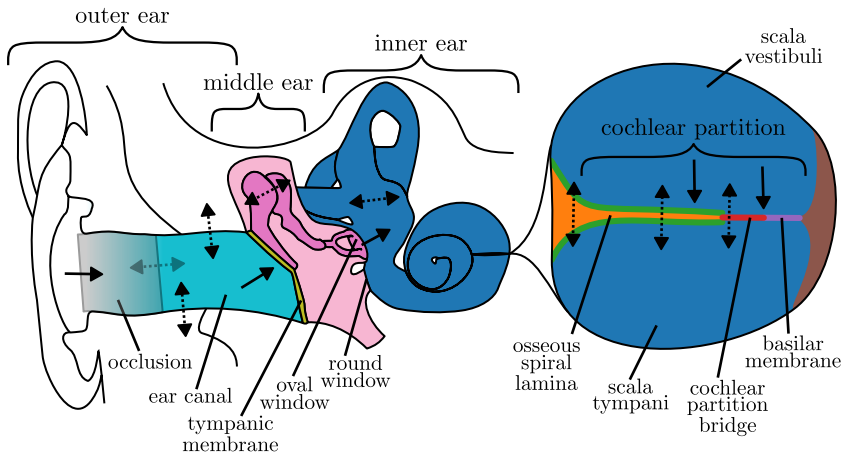
Figure 1.1: Sectional diagram of the ear and cross-sectional illustration of the cochlear partition. Solid arrows indicate vibroacoustic interactions in air conduction hearing, while dotted arrows indicate additional interactions involved in bone conduction hearing. An occluded ear canal condition is shown in semitransparent gray. In line with the macro-mechanism-focused approach in this thesis, detailed cochlear microstructures are not included.

Tonndorf, 1966, 1968), illustrated by dotted arrows in Figure 1.1. At the inner ear, the vibration of its surroundings induces inertial forces within the cochlear fluid and pressure responses due to deformation (Dobrev et al., 2025, 2023; Kim et al., 2011; Stenfelt, 2015; Tonndorf, 1962), both affected by the acoustic properties the oval window (OW), round window (RW) and cochlear partition (CP) (Tonndorf, 1966). The relative contribution of these two mechanisms is frequency-dependent. At lower frequencies, where the wavelengths in the surrounding bone are much larger than the inner ear dimensions, the inner ear primarily exhibits rigid body motion and behaves as a compact inertial object, while at higher frequencies deformation effects may become more dominant (Stenfelt, 2015). This vibrational stimulation interacts with the inner ear's response to input at the OW, which involves a relative motion of the ME and the adjacent bone due to inertia of the ossicles (Dobrev et al., 2020; Homma et al., 2009; Stenfelt et al., 2002), sound generated by the vibration of the EC (Stenfelt et al., 2003b; Surendran and Stenfelt, 2021), and components entering the ear via the EC entrance (Pörschmann, 2000; Xu et al., 2021). Additionally, an unequal fluid flow between the OW and RW (Stenfelt et al., 2004a) and sound pressure transmission from the skull interior (Dobrev et al., 2022; Freeman et al., 2000; Sohmer and Freeman, 2004) have been regarded as indicators for "third-window" mechanisms in BC hearing.

Experimentally assessing the mechanisms involved in AC and BC hearing poses significant difficulties. While the EC sound pressure can be measured in living subjects, direct measurements at healthy inner ears – which ultimately serve as sensors for all AC and BC pathways – are not feasible for ethical reasons. Even with temporal bone specimen or cadaver heads, the measurement of important quantities such as intracochlear sound pressures (e.g., Dobrev et al., 2022, 2023; Frear et al., 2018; Mattingly et al., 2020; Nakajima et al., 2009; Olson, 1999; Stieger et al., 2018) or velocities of the stapes footplate and cochlear bone (e.g., Dobrev and Sim, 2018; Lim et al., 2023; Stenfelt and Goode, 2005b) require an intervention into the vibrating system, with the risk to affect the vibroacoustic behavior. To minimize these effects, sensors need to be small and placed only at a few positions. However, these conditions result in a low spatial resolution – e.g., typically two locations for intracochlear sound pressures (Dobrev et al., 2022, 2023; Frear et al., 2018; Mattingly et al., 2020; Nakajima et al., 2009; Olson, 1999; Stieger et al., 2018) – and often impose technical constraints such as measurement noise. These experimental limitations highlight that modeling and numerical simulations are essential to improve our understanding of hearing. These approaches enable:

- three-dimensional explorations of structural vibrations and sound pressures;

- separate investigations the different components involved by splitting up the hearing system, e.g., at the tympanic membrane (TM) or OW;
- qualitative and quantitative assessments of the effects within the different subsystems, such as at the EC or within inner ear; and
- the identification of underlying mechanisms and influencing factors by varying model properties and simulation conditions, including conditions which differ to those in real ears.

1.2 Occlusion effect

Beyond its role in the perception of one's own voice, BC hearing is utilized in audiological applications such as BC audiometry (*ISO 8253-1* 2010) or BC hearing aids (Kompis and Caversaccio, 2011), where skull vibrations are directly induced by a transducer. A more familiar example may be the often surprising experience of hearing a recording of one's own voice, which misses the BC component perceived during speaking. Similarly, an altered own-voice perception occurs when the EC is occluded, whether by a finger or by devices such as earplugs or hearing aids (Figure 1.1). This effect arises because the BC sound induced by vibration of the EC is amplified at low frequencies, while the AC voice component entering at the EC entrance is attenuated at higher frequencies (Carillo et al., 2021a; Hansen, 1998; Zurbrügg et al., 2014). This phenomenon is known as occlusion effect (OE).[1] The OE is a well-documented challenge in audiology, contributing to dissatisfaction among hearing aid users (Dillon, 2012b; Hengen et al., 2020; Winkler et al., 2016) and reducing the acceptance of workers to wear hearing protection (Doutres et al., 2019).

Significant progress in understanding the fundamental physical mechanisms of the OE has been made through modeling approaches. These range from one-dimensional circuit models (e.g., Carillo et al., 2020, 2021a; Hansen, 1998; Schroeter and Poesselt, 1986; Stenfelt and Reinfeldt, 2007; Zurbrügg et al., 2014) to more advanced finite element (FE) simulations (e.g., Brummund et al., 2014, 2015; Carillo et al., 2020, 2021b; Xu et al., 2021). Identified influencing factors include:

- the frequency dependent distribution of the EC wall vibrations in magnitude and phase (Carillo et al., 2020, 2021c), which varies between the elastic soft tissue / cartilage part and the bony part of the EC (Stenfelt and Reinfeldt, 2007),

---

[1]Early descriptions of the OE date back to Wheatstone (1827), who noted that closing the EC "with the finger without pressure" alters auditory perception. The unfamiliarity with hearing one's voice "as recorded by a phonograph" was mentioned in Békésy's famous book *Experiments in Hearing* (Békésy, 1960, p. 127).

- the source of stimulation, e.g., BC transducers (Brummund et al., 2015; Reinfeldt et al., 2013; Stenfelt and Reinfeldt, 2007; J. Wang et al., 2022), one's own voice (Hansen, 1998; Saint-Gaudens et al., 2022; Zurbrügg et al., 2014), or mastication (Saint-Gaudens et al., 2022),
- the variation of the vibrating area of the wall with the occluding device's insertion (Dillon, 2012b; Stenfelt and Reinfeldt, 2007; Zurbrügg et al., 2014),
- the mechanical load of the occluding device to the vibration of the EC wall (Denk et al., 2022; Dillon, 2012b; Hansen, 1998),
- the acoustical load to the vibration of the EC wall due to the occlusion (Brummund et al., 2014),
- the boundary and loading conditions within numerical simulations, e.g., at the temporal bone and soft tissue of an outer ear model (Carillo et al., 2020), or at the base of a truncated head model (Xu et al., 2021).

Yet, accurately predicting the OE and assessing the effectiveness of measures to reduce it – such as vents (Kuk et al., 2009; Zurbrügg et al., 2014), open-fitting hearing aids (Winkler et al., 2016), active cancellation systems (Borges et al., 2013; Denk et al., 2024; Liebich et al., 2016; Mejia et al., 2008; Zurbrügg et al., 2015), earmold designs (Denk et al., 2022), or sound-absorbing earplugs (Carillo et al., 2022, 2023) – remains challenging. These difficulties primary stem from two factors: accurately predicting the EC sound pressure in open and occluded conditions, and assessing the subjective perception of the OE.

The OE is objectively evaluated by measuring the sound pressure level increase in the EC resulting from the occlusion. This increase mainly appears at frequencies below 1 kHz (Stenfelt et al., 2003b) and exhibits a low-pass characteristic (Carillo et al., 2021a; Stenfelt and Reinfeldt, 2007; Tonndorf, 1968). Comparisons between experimental data and model predictions (Brummund et al., 2014; Carillo et al., 2021b; Xu et al., 2021) indicate that models tend to overestimate the OE at lower frequencies. Experimental results also exhibit a greater variability and excitation dependence in this frequency range (Reinfeldt et al., 2013; Saint-Gaudens et al., 2022).

Beyond objective measurements, perceptual assessments suggest that sound pressures in the EC alone do not fully explain the subjective experience of the OE (Reinfeldt et al., 2013; Saint-Gaudens et al., 2022; Stenfelt and Reinfeldt, 2007). This finding likely arises from different contributions of the BC components: for the occluded condition, sound pressure in the EC may dominate the overall BC perception, while the other paths – which are not captured by the EC sound pressure – may be the main contributors with an open EC (Stenfelt and Goode, 2005a; Stenfelt et al., 2003b; Taschke, 2005). Consequently, evaluating the OE

based solely on EC sound pressures may overestimate its perception (Reinfeldt et al., 2013; Saint-Gaudens et al., 2022).

1.3 Role of the inner ear

Understanding the physics underlying the perception of one's own voice and the OE, therefore, requires an analysis of the inner ear's vibroacoustic behavior, because this is where all AC and BC pathways converge and interact.

Challenging long-held assumptions about inner ear mechanics, recent studies have highlighted the flexibility of the CP (Kerkhofs et al., 2023; Raufer et al., 2019, 2020), which is located between the scala vestibuli (SV) and scala tympani (ST) and comprises the osseous spiral lamina (OSL) and basilar membrane (BM) (Figure 1.1). Advancements in imaging techniques revealed that the OSL consists of two thin structures, known as vestibular plate (VP) and tympanic plate (TP), enveloping soft tissue and the auditory nerves (Bom Braga et al., 2023; Raufer et al., 2020). Furthermore, these anatomical studies identified the cochlear partition bridge (CPB), a soft-tissue structure located between the OSL and BM, which exhibits a width comparable to that of the BM (Raufer et al., 2019, 2020).

In classical cochlear mechanics, the OSL and CPB are considered rigid, with the BM as the primary flexible structure underlying cochlear function (Raufer et al., 2019). Most models adhere to this view. For instance, FE models used to investigate BC hearing – including BM traveling waves and the comparisons to AC (Kim et al., 2011; Lim et al., 2022; Ren et al., 2021), directional sensitivity (Kim et al., 2014), and responses to BC hearing aids (Lim et al., 2022) – typically treat the OSL as rigid and omit the CPB. However, pioneering experiments by Békésy (1960), including measurements of the CP stiffness, already suggested that CP motion is not confined to the BM but also involves the OSL. Subsequent studies extended these findings by measuring CP velocities approximately 12 mm from cochlear base (Stenfelt et al., 2003a) and radial velocity distributions in its vicinity (Raufer et al., 2019). Despite these efforts, experimental data on the OSL and the combined CP motion remain sparse and spatially limited.

Among the few studies addressing CP flexibility, Taber and Steele (1981) employed a mathematical box model to demonstrate that OSL deflection may dominate CP motion in the basal region. Building on this, Kohllöffel (1983) hypothesized that a flexible OSL could shunt the wave propagation in the cochlear fluid between SV and ST, thereby affecting the cochlear input impedance. Indeed, cochlear impedance measurements indicate resistive characteristics of both the input impedance and the differential impedance across the CP (Aibara et al., 2001; Frear et al., 2018; Nakajima et al., 2009), contrasting with the inertial characteristics associated with cochlear fluid. However, Raufer et al. (2019)

noted that the fluid volume displacements associated with the OSL and CPB may not significantly influence the tonotopic mapping on the BM.

In the context of BC hearing, the role of the CP's flexibility has also received little attention. Tonndorf (1966) highlighted the importance of the differential CP impedance in BC hearing, alongside the impedances of the OW and RW, in influencing the fluid inertial effects within the inner ear. Furthermore, Stenfelt et al. (2003a) concluded that OSL motion during BC is driven by inertial forces in the cochlear fluid, potentially affecting intracochlear sound pressures. Nevertheless, they acknowledged the difficulty in predicting the impact of this motion, suggesting its influence may be significant at higher frequencies but negligible in healthy ears.

1.4 Structure of the thesis

This thesis advances the understanding of the vibroacoustic mechanisms in AC and BC hearing through a focused modeling approach, systematically identifying and analyzing underlying physical phenomena by separating the auditory system into subsystems.

Chapter 2 investigates a more comprehensive view on the sound generation by the structural motion of the EC. The novelty of this approach lies in the complementation of EC wall vibration by the motions of the EC entrance and TM. An impedance boundary condition is proposed to include these motions in circuit and FE models used to investigate the OE and improve its prediction. Related mechanisms are illustrated based on a circuit model, utilizing an EC motion extracted from a FE model of a human head.

Following the sound propagation from the EC towards the inner ear, Chapter 3 examines the effect of the CP's flexibility on the inner ear's response to input at the OW. An anatomical FE model of the human inner ear is introduced, which allows modeling the OSL and CPB as either rigid or flexible structures. This approach enables an analysis of their effects on intracochlear sound pressures, cochlear impedances, CP stiffness, and CP motion, offering insights into the macro mechanisms within the inner ear and corresponding experimental findings.

Chapter 4 extends this investigation by additionally accounting for the rigid body motion of the inner ear during BC stimulation. Focusing on the role of the OSL in inner ear fluid dynamics, this chapter provides insights into the interplay between OW input, rigid body stimulation, and different types of OSL motion. An analysis of intracochlear sound pressure distributions and differential fluid flow at the OW, RW, and OSL establishes links to experimental findings that have previously been attributed to "third-window" effects in BC hearing.

Chapter 5 concludes this thesis, summarizing key findings and addressing critical limitations. Suggestions for future research on the vibroacoustic mechanisms in AC and BC hearing are proposed to further improve our understanding of the physics underlying own-voice perception, the OE, and BC hearing aids, ultimately contributing to advancements in hearing technologies.

2

Impact of the ear canal motion on the occlusion effect

2.1 Introduction

Researchers have employed various modeling approaches to simulate the OE, ranging from one-dimensional circuit models (e.g., Carillo et al., 2020, 2021a; Hansen, 1998; Schroeter and Poesselt, 1986; Stenfelt and Reinfeldt, 2007; Zurbrügg et al., 2014) to more advanced FE simulations (e.g., Brummund et al., 2014, 2015; Carillo et al., 2020, 2021b; Xu et al., 2021). Building on these approaches, this chapter addresses the sound pressure increase in the EC due to occlusion, which is primarily driven the vibration of the EC wall. When treated as a volume velocity source, this vibration leads to a high-pass characteristic of the TM sound pressure in the open EC (Carillo et al., 2021a; Zurbrügg et al., 2014). Blocking the EC removes this filter effect, resulting in a low-pass characteristic of the OE (Carillo et al., 2021a; Stenfelt and Reinfeldt, 2007; Tonndorf, 1968; Zurbrügg et al., 2014). Consequently, the OE is most pronounced at frequencies below approximately 1 kHz (Hansen, 1998; Stenfelt et al., 2003b). This chapter investigates whether a more comprehensive view of the three-dimensional structural motion of the EC can further improve our understanding of the vibroacoustic mechanisms involved. By doing so, it aims to provide insights that may help reconcile discrepancies between predicted and experimentally measured OEs. Some definitions of the OE may also include the attenuation of external sounds entering via the EC entrance (Zurbrügg et al., 2014), such as an own-voice component that propagates around the head (Pörschmann, 2000). However, these aspects are not specifically examined in this chapter.

Below 300 Hz, the skull undergoes rigid body motion (Stenfelt and Goode, 2005b), causing the bony part of the EC to follow. Additionally, the wavelength in the surrounding soft tissue and cartilage is comparable to or larger than the dimensions of the EC.[1] As a result, EC segments partially exhibit a rigid body motion, characterized with a displacement that is in phase, of similar magnitude, and spatially in the same direction along all points on the EC wall within a given segment. In the following, this phenomenon will be referred to as *non-deforming motion* of parts of the EC. At the EC entrance and the TM, this non-deforming motion results in a motion of the entrance plane and TM, respectively, due to their connections with the surrounding structures. The motions of these boundaries complements the vibration of the EC wall in generating sound pressure within the EC. Figure 2.1 illustrates the two scenarios: one considering the motion of the EC entrance and TM due to non-deforming motion of adjacent EC segments, and the other accounting solely for the vibration of the EC wall.

To incorporate this phenomenon into OE modeling, it is important to recognize that OE models typically represent the EC entrance and TM as impedance boundaries. At the open EC entrance, the impedance accounts for the outward sound radiation (Brummund et al., 2014, 2015; Carillo et al., 2020, 2021a, 2021b; Hansen, 1998; Schroeter and Poesselt, 1986; Stenfelt and Reinfeldt, 2007). For an occluded ear, the impedance instead represents the properties of the blocking device, differing from the open-ear case (Brummund et al., 2014, 2015; Carillo et al., 2020, 2021a; Hansen, 1998; Schroeter and Poesselt, 1986; Stenfelt and Reinfeldt, 2007). At the TM, the impedance accounts for the load from the membrane, the ME cavity, the ME ossicles, and inner ear (Hudde and Engel, 1998a, 1998b, 1998c; Shaw and Stinson, 1983). This approach eliminates the need for detailed modeling of the ME structures, making it the most common method in OE models (Brummund et al., 2014, 2015; Carillo et al., 2020, 2021a, 2021b; Hansen, 1998; Schroeter and Poesselt, 1986; Stenfelt and Reinfeldt, 2007; Xu et al., 2021; Zurbrügg et al., 2014).

Conceptually, the impedance-based approach assumes a piston-like motion at both the EC entrance and the TM (Stinson et al., 1982). This simplification is justified because, within the relevant frequency range up to 2 kHz, the wavelength in air remains significantly larger than the radial dimensions of the EC and the TM.[2] Furthermore, experimental observations suggest a simple vibration pattern

---

[1] For instance, when employing the material parameters referred to as "Reference" in Xu et al. (2021) the wavelength of shear waves in soft tissue at 100 Hz exceeds the EC dimensions by a factor of three. In cartilage, the wavelength surpasses the EC dimensions even by a factor of twenty to forty at this frequency.

[2] For example, with a sound speed of 343 m/s, the wavelength at 2 kHz exceeds a typical TM diameter of 9 mm (Stinson, 1985) by a factor of 19.

(a) Sketch of the ear canal

(b) Including motions of entrance
and tympanic membrane

(c) Wall vibration only
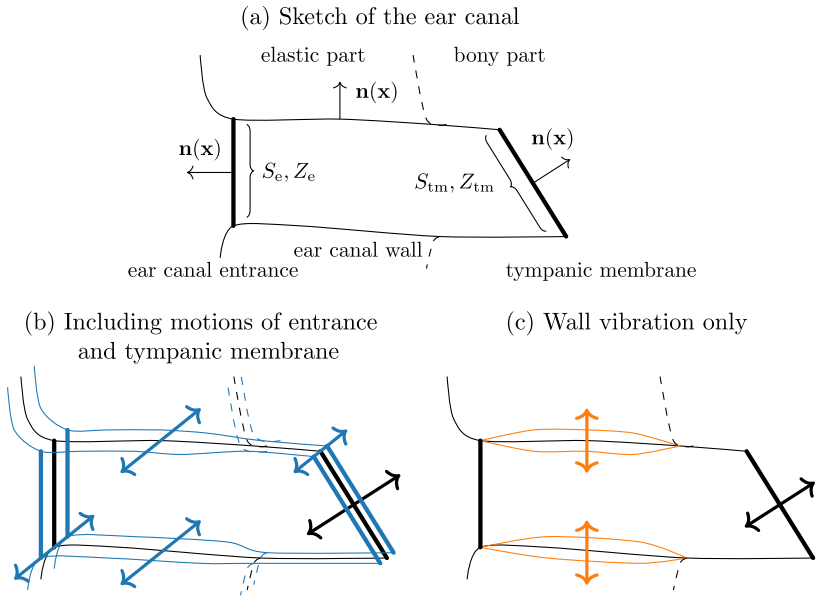
Figure 2.1: Sketch of the EC and its structural motion during BC stimulation. In panel (b), the EC motion includes motions of the EC entrance and TM. These motions are caused by non-deforming motions of the attached EC segments (blue double arrows), which complement the EC wall vibration. For comparison, panel (c) depicts an EC motion where the wall vibration is the sole source of the sound pressure acting on the TM.

of the TM below 2 kHz (Rosowski et al., 2009). This allows using a volume velocity to describe its motion instead of considering spatially distributed point velocities (Rosowski et al., 2009; Tonndorf and Khanna, 1972). Within the frequency range of interest, the sound pressure level close to the TM varies spatially by about 1 dB (Hudde and Schmidt, 2009). The TM acoustic impedance can then be defined as the average sound pressure across the TM divided by its volume velocity during AC stimulation (Stinson, 1985). For BC stimulation, the TM may radiate sound originating from the ME into the EC. However, experimental data suggests that this reverse excitation does not significantly contribute to the EC sound pressure, except around the EC resonance at approximately 3 kHz (Stenfelt et al., 2003b).

This chapter aims to investigate the impact of the motions of the EC entrance and TM due to non-deforming motion of the adjacent structures on the simulation of the OE, specifically focusing on effects related to the impedance boundary

conditions. To examine influencing factors and underlying mechanisms, circuit calculations are presented using examples in which an EC motion is extracted from a FE model of a human head.

2.2 Methods

2.2.1 Formulation of the impedance boundary condition

Because the mechanism underlying the OE is the complex interaction of the vibrations of the EC structure with the sound field in the EC, OE models can be methodologically considered as fluid-structure problems.[3] Let z be the specific acoustic impedance of a boundary attached to a moving structure, the impedance boundary condition is (Marburg and Anderssohn, 2011; Suzuki et al., 1989)

$$v = p/z + v_\mathrm{s}, \text{ or } z = \frac{p}{v - v_\mathrm{s}} \qquad (2.1)$$

with p denoting the sound pressure, and v the normal acoustic particle velocity. v_s is the associated velocity of the surrounding structure in normal direction to the boundary, which is often omitted (Marburg and Anderssohn, 2011). Equation 2.1 states that v_s is to be superimposed on the reaction term p/z to obtain the particle velocity v when solving a fluid-structure problem. From another perspective, it states that the *relative, differential velocity* $v - v_\mathrm{s}$ between the air and its surrounding structure is to be incorporated to obtain the sound pressure p.

Two examples highlight the validity of Equation 2.1. For an acoustically rigid boundary ($z \to \infty$), $v = v_\mathrm{s}$, which means it moves with the adjacent solid. Neglecting v_s would misleadingly cause v to be zero in this case, implying that the acoustic boundary is fixed in position regardless of the surrounding structure's motion. If the structure is fixed ($v_\mathrm{s} = 0$), Equation 2.1 leads to the specific acoustic impedance definition $z = p/v$, which is commonly used within previous OE models.

2.2.2 Application to occlusion effect modeling

As depicted in Figure 2.1, the two boundaries often assigned with acoustic impedances for the simulation of the OE are the EC entrance and the TM (e.g., in (Brummund et al., 2014, 2015; Carillo et al., 2020, 2021a, 2021b; Hansen, 1998; Schroeter and Poesselt, 1986; Stenfelt and Reinfeldt, 2007; Zurbrügg et al., 2014)). The question is how to implement the impedance boundary condition

---

[3]General information on fluid-structure problems can be found, e.g., in Atalla and Sgard (2015)
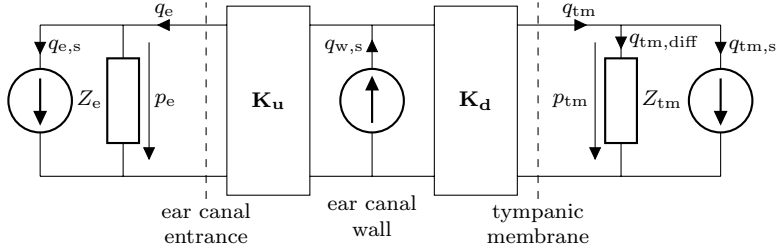
Figure 2.2: Circuit model of the EC. The impedance Z_e represents an occluding device or the exterior radiation of sound in case of the open ear, respectively. Z_{tm} denotes the TM impedance. The sources $q_{e,s}$ and $q_{tm,s}$ parallel to Z_e and Z_{tm} account for the motion associated with these boundaries due to their connections with the attached structures. The vibration of the EC wall is represented by the volume velocity source $q_{w,s}$. It splits up the EC air volume into an upstream segment towards the EC entrance, and a downstream segment terminated by the TM. For the circuit calculations presented in this chapter, the EC segments are modeled as acoustical transmission lines represented by two-port matrices $\mathbf{K_u}$ and $\mathbf{K_d}$.

from Equation 2.1 into these models to account for a non-deforming motion of the surrounding structures. Since it is a general phenomenon of structure-fluid inter-action, it may affect both numerical approaches, e.g., using the FE method, and simplified approaches such as equivalent circuit calculations. The investigation begins with employing the circuit model shown in Figure 2.2 to provide a "visual image of the system" (Zwislocki, 1962). The circuit provides an overview of the physical mechanisms involved and allows separating the different contributions to the TM sound pressure. Subsequently, an application of Equation 2.1 to FE models is proposed.

Circuit modeling

In Figure 2.2, the sound generation by the motion of the EC structure is divided into three volume velocity sources $q_{w,s}$, $q_{e,s}$ and $q_{tm,s}$. Each of the sources corresponds to a specific boundary with distinct acoustic properties, necessitating their separate treatment. $q_{w,s}$ characterizes the volume velocity induced by the vibration of the EC wall,

$$q_{w,s} = -\iint_{S_w} \mathbf{v}_s(\mathbf{x}) \cdot \mathbf{n}(\mathbf{x}) \, dS. \tag{2.2}$$

Here, S_w represents the surface of the EC wall, while $\mathbf{v}_s(\mathbf{x})$ is the complex-valued, three-dimensional structural velocity distribution along positions denoted as $\mathbf{x}$

on this surface. $\mathbf{n}(\mathbf{x})$ is the unit vector perpendicular to S_{w} at $\mathbf{x}$ in outward direction of the EC, as indicated in Figure 2.1. Accordingly, the dot product $\mathbf{v}_{\mathrm{s}}(\mathbf{x}) \cdot \mathbf{n}(\mathbf{x})$ captures the local normal component of the velocity. The negative sign in Equation 2.2 accounts for the vector component to be defined outwards while $q_{\mathrm{w,s}}$ is here considered to be positive inwards.

Note that Equation 2.2 accounts for the vibration of the EC wall in general, which could include non-deforming motion of the parts. Yet, a non-deforming motion of an EC segment does not contribute to $q_{\mathrm{w,s}}$. For such a motion, $\mathbf{v}_{\mathrm{s}}$ remains constant across all positions on the wall within that segment. Consequently, the contributions of opposing boundaries within this segment to the overall volume velocity cancel each other due to the differing signs of $\mathbf{v}_{\mathrm{s}}(\mathbf{x}) \cdot \mathbf{n}(\mathbf{x})$. One should be aware that describing the EC wall vibration as source using the integral quantity $q_{\mathrm{w,s}}$ is only valid as long as the wavelength in air is much larger than the dimensions of the radiating wall area. This is the case at least in the considered frequency range below $1\,\mathrm{kHz}$.

The source of strength $q_{\mathrm{e,s}}$ represents the volume velocity corresponding to the motion with the surrounding structure of the EC entrance plane (see Figure 2.1). The source is in Figure 2.2 parallel to the impedance Z_{e}, which represents the occluding device ($Z_{\mathrm{e}}^{\mathrm{occl}}$), or the exterior radiation of sound out of the open ear ($Z_{\mathrm{e}}^{\mathrm{open}}$). The resulting equation regarding the total acoustic volume velocity q_{e} towards the EC entrance is

$$q_{\mathrm{e}} = p_{\mathrm{e}}/Z_{\mathrm{e}} + q_{\mathrm{e,s}}, \tag{2.3}$$

with p_{e} denoting the sound pressure at the EC entrance. Equation 2.3 is closely related to Equation 2.1, but expressed with volume velocities instead of point velocities and with the impedance Z_{e} in $\mathrm{Pa\,s/m^3}$ based on the conception of a piston-like, one-dimensional motion of the boundary (see Section 2.1). Note that $q_{\mathrm{e,s}}$ refers to the passive motion of the EC entrance plane, which neglects the sound radiated into the EC from the outside, or the sound radiated by the occluding device (in that sense, the volume velocity imposed by the earplug as defined by Carillo et al. (2021b) represents both contributions). If desired, the radiation of an occluding device could be included by a second volume velocity source parallel to Z_{e} in the circuit in Figure 2.2.

The volume velocity source $q_{\mathrm{tm,s}}$ in Figure 2.2 incorporates the motion of the TM due to the non-deforming motion of the surrounding bone (see colored arrows in Figure 2.1). $q_{\mathrm{tm,s}}$ establishes the boundary condition for the total acoustical volume velocity q_{tm} towards the TM,

$$q_{\mathrm{tm}} = p_{\mathrm{tm}}/Z_{\mathrm{tm}} + q_{\mathrm{tm,s}}, \tag{2.4}$$

analogously to Equation 2.1 and Equation 2.3. Here, p_{tm} denotes the sound pressure at the TM. Equation 2.4 states that the motion of the TM with the surrounding bone – represented by $q_{tm,s}$ – is superimposed with the relative motion between the ossicles and the surroundings due to the sound transmission from the TM to the inner ear – depicted by the term p_{tm}/Z_{tm}. Z_{tm} corresponds to the impedance that would be measured on human subjects using classical acoustical methods, when there is no structural motion of the EC. Accordingly, it incorporates the complex deformation of the TM itself and the inertia of the ME ossicles (Hudde and Engel, 1998a, 1998b, 1998c; Stinson, 1985; Stinson and Lawton, 1989; Zwislocki, 1962). The formulation in Equation 2.4 conceptually implies the ME and inner ear to move together with the TM and the surrounding temporal bone, so BC sound transmitted from the ME into the EC via the TM (Schroeter and Poesselt, 1986; Stenfelt et al., 2003b) is not accounted for. A second source could be added for this purpose, if desired.

Finite element modeling

Equation 2.1 already gives the boundary condition for acoustic impedances within FE models, and a more detailed formulation is, e.g., presented by Marburg and Anderssohn (2011). However, implementing Equation 2.1 raises the question on how to obtain the structural velocity v_s.

Within such models, the TM is represented by its surface in contact with the air and assigned with the TM impedance, rather than including it as a solid structure. In this case, a reasonable approach is to determine a vector $\langle \mathbf{v} \rangle_{tm,s}$ as the component-wise average of the structural velocity over the mutual edge of the TM surface with the adjacent bone. The structural velocity $v_{tm,s}$, which is included in the boundary condition, is then calculated locally as the normal component of $\langle \mathbf{v} \rangle_{tm,s}$,

$$v_{tm,s}(\mathbf{x}) = \langle \mathbf{v} \rangle_{tm,s} \cdot \mathbf{n}(\mathbf{x}) \qquad (2.5)$$

Here, $\mathbf{n}(\mathbf{x})$ is the unit vector perpendicular to the TM surface at position $\mathbf{x}$ in outward direction of the EC (see Figure 2.1). Including $v_{tm,s}$ in this manner in the acoustic boundary condition conceptually accounts for a piston-like motion of the TM surface, which follows the average structural motion of its edge. As already argued with regard to circuit models in Section 2.2.2, this formulation implies that the ME and inner ear structures align with this motion.

Obtaining the corresponding structural velocity $v_{e,s}$ at the EC entrance is feasible following the same approach by averaging via the mutual edge of the entrance plane with the surrounding structures. For instance, with a rigid impedance representing the occluding device, the resulting acoustic boundary condition in Equation 2.1 locally accommodates the piston-like motion of the device with

its surroundings. Thus, non-rigid devices and the open-ear radiation just result in different impedance terms p/z in Equation 2.1, but the method for determining $v_{e,s}$ remains unchanged. However, it is essential to acknowledge that Equation 2.1 solely accounts for sources inside the EC. To also encompass the BC-excited radiation from the head into the EC via the EC entrance (Xu et al., 2021), an additional term would need to be incorporated.

The structural velocities in FE models and the volume velocities in the circuit approach are for both the open and occluded ear cases related as

$$
\begin{aligned}
q_{e,s} &= \iint_{S_e} v_{e,s}(\mathbf{x})\, dS, \\
q_{tm,s} &= \iint_{S_{tm}} v_{tm,s}(\mathbf{x})\, dS.
\end{aligned}
\tag{2.6}
$$

Here, S_e and S_{tm} denote the surfaces of the entrance plane and TM, as indicated in Figure 2.1. Note that, with the convention used here, $q_{e,s}$ is defined in outward direction normal to the entrance plane, and $q_{tm,s}$ is defined in direction towards the ME. The complex-valued relation of $q_{w,s}$, $q_{e,s}$ and $q_{tm,s}$ depends on the actual three-dimensional motion of the EC and the orientation of the corresponding boundaries. Hence, a certain EC motion is implied implicitly or explicitly when conducting OE simulations. Given the relationship between the modeling approaches from Equation 2.6, the circuit model from Figure 2.2 is employed in the following to further elucidate the underlying mechanisms and discuss corresponding effects.

2.2.3 Effect on the simulation of the occlusion effect

To investigate the effect of the consideration of the structural EC motion within the impedance boundary conditions at EC entrance and TM, a formulation is now derived which explicitly reveals the dependency of the OE on the EC motion. This formulation is developed using the circuit model shown in Figure 2.2, where the EC motion finds representation through $q_{w,s}$, $q_{e,s}$, and $q_{tm,s}$. To accomplish this, the differential volume velocity $q_{tm,diff}$ is scrutinized,

$$
q_{tm,diff} = q_{tm} - q_{tm,s}.
\tag{2.7}
$$

It signifies the resulting *relative motion* between the TM and the surrounding bone, determining the TM pressure

$$
p_{tm} = Z_{tm} q_{tm,diff}.
\tag{2.8}
$$

This pressure is transmitted through the ME to the inner ear, thereby representing the auditory perception in a manner analogous to AC sound. Extending the approach of Carillo et al. (2021a), volume velocity transfer functions T_{w}, T_{e}, and T_{tm} are defined to quantify the specific contributions of $q_{\mathrm{w,s}}$, $q_{\mathrm{e,s}}$ and $q_{\mathrm{tm,s}}$ to $q_{\mathrm{tm,diff}}$, respectively, so that

$$q_{\mathrm{tm,diff}}^{k} = T_{\mathrm{w}}^{k} q_{\mathrm{w,s}}^{k} + T_{\mathrm{e}}^{k} q_{\mathrm{e,s}}^{k} + T_{\mathrm{tm}}^{k} q_{\mathrm{tm,s}}^{k}, \ k \in \{\mathrm{open, occl}\}. \tag{2.9}$$

The volume velocity transfer functions account for the observation that the induced volume velocities are divided into the branches of the circuit in Figure 2.2 according to the impedance relations, so only a part is transmitted to the TM. Consequently, as indicated in Equation 2.9, their characteristics depend on whether the EC is open or occluded, due to the corresponding impedance change at the EC entrance. The transfer functions may also encompass variations of the EC volume resulting from the insertion of an occluding device, as indicated by the dependency on the occlusion condition in Equation 2.9. This dependency is also denoted for $q_{\mathrm{w,s}}$ to accommodate the factors outlined in Section 1.2, such as a variation of the radiating wall area (Dillon, 2012b; Stenfelt and Reinfeldt, 2007), and for $q_{\mathrm{e,s}}$ and $q_{\mathrm{tm,s}}$ to account for changes of motion or different surfaces of the occluding device and the open EC entrance.

Using Equation 2.9, the OE for a structural motion of the EC considering both the vibration of the EC wall and the motions of the EC entrance plane and TM is

$$\begin{aligned}
\mathrm{OE} &= 20 \log_{10} \left| \frac{p_{\mathrm{tm}}^{\mathrm{occl}}}{p_{\mathrm{tm}}^{\mathrm{open}}} \right| \\
&= 20 \log_{10} \left| \frac{T_{\mathrm{w}}^{\mathrm{occl}} q_{\mathrm{w,s}}^{\mathrm{occl}} + T_{\mathrm{e}}^{\mathrm{occl}} q_{\mathrm{e,s}}^{\mathrm{occl}} + T_{\mathrm{tm}}^{\mathrm{occl}} q_{\mathrm{tm,s}}^{\mathrm{occl}}}{T_{\mathrm{w}}^{\mathrm{open}} q_{\mathrm{w,s}}^{\mathrm{open}} + T_{\mathrm{e}}^{\mathrm{open}} q_{\mathrm{e,s}}^{\mathrm{open}} + T_{\mathrm{tm}}^{\mathrm{open}} q_{\mathrm{tm,s}}^{\mathrm{open}}} \right|.
\end{aligned} \tag{2.10}$$

Equation 2.10 expresses the OE directly as a function of the sources representing the EC motion caused by BC stimulation. It highlights the two main influencing factors for the impact of the EC motion at the TM and EC entrance on the OE: (1) the volume velocity transfer towards the TM, expressed by T_{w}, T_{e}, and T_{tm}, and (2) the relation and magnitudes of the different boundaries' motion, expressed by the volume velocities $q_{\mathrm{w,s}}$, $q_{\mathrm{e,s}}$, and $q_{\mathrm{tm,s}}$.

Accordingly, modeling assumptions regarding the EC motion – or the contributions of $q_{\mathrm{w,s}}$, $q_{\mathrm{e,s}}$, and $q_{\mathrm{tm,s}}$ – are in principle necessary for the simulation of the sound pressure at the TM and the resulting OE. However, the OE is commonly understood in a way that the vibration of the EC wall predominantly induces the sound pressure in the EC during the BC stimulation. This is a valid assumption when the magnitude of the wall's volume velocity, $|q_{\mathrm{w,s}}|$, greatly surpasses the

contributions of the EC entrance and TM, $|q_{e,s}|$ and $|q_{tm,s}|$ (see Figure 2.1 for illustration). In this case, Equation 2.10 simplifies to

$$\text{OE} \approx 20 \log_{10} \left| \frac{T_w^{occl} q_{w,s}^{occl}}{T_w^{open} q_{w,s}^{open}} \right|. \tag{2.11}$$

If it is additionally assumed that the fictive entrance plane of the open EC and the surface of the occluding device are aligned (approximating a "shallow insertion" of an earplug), and that the influence of the change in acoustical load caused by the occlusion on the vibration of the EC wall is negligible (Brummund et al., 2014), $q_{w,s}$ is independent of the occlusion condition. Consequentially, the cancellation of $q_{w,s}$ in Equation 2.11 results in an OE which depends only on the alteration of the volume velocity transfer function T_w (Carillo et al., 2021a).

2.2.4 Circuit calculations for bone-conducted stimulation at the ipsilateral mastoid

The effect of considering both the EC wall vibration and the motions of the EC entrance and TM on the simulation of the OE is now demonstrated using the circuit model in Figure 2.2. The problem, however, is that each specific contribution of the boundaries involved depend on the type of excitation. As no general data on the spatially distributed motion of the EC for BC stimulation and the corresponding volume velocities is available yet, an example is taken as a case study.

The motions were extracted from the FE model of a human head presented by Xu et al. (2021). The excitation was a BC stimulation of 1 N at the ipsilateral mastoid similar to a BC transducer (Brummund et al., 2015; Reinfeldt et al., 2013; Stenfelt and Reinfeldt, 2007). The head base was fixed, and the tissue material properties denoted as "Reference" in Xu et al. (2021) were applied. Despite the adjustments at the EC entrance and TM described in Appendices A.1 and A.2, which serve the purpose of ensuring the circuit calculations to be representative in highlighting the mechanisms involved, the FE model was kept as documented in detail by Xu et al. The volume velocities $q_{w,s}$, $q_{e,s}$, and $q_{tm,s}$ were extracted from the FE simulations following Equation 2.2 and Equation 2.6 as reported in Appendix A.1. Subsequently, the volume velocity transfer functions were calculated based on the circuit in Figure 2.2. Using the extracted volume velocities as input then allowed to calculate the terms $T_w q_{w,s}$, $T_e q_{e,s}$, and $T_{tm} q_{tm,s}$ from Equation 2.9 as well as the resulting OE according to Equation 2.10 and Equation 2.11.

To obtain the volume velocity transfer functions, the sound propagation within the EC needs to be considered. Therefore, the EC acoustics was modelled

using a simplified circular cross-section, cylindrical geometry with an EC length, l_{ec}, of 27.7 mm and radius, r_{ec}, of 3.85 mm. These dimensions lead to the same length and volume of the cylinder as the EC in the FE model (Xu et al., 2021). The cylindrical geometry neglects the variability of the radius along the EC axis. The comparison between the circuit- and finite-element-calculated sound pressure in Appendix A.2 shows that the circuit calculations can be considered to appropriately represent the mechanisms related to the motions of the EC entrance plane and TM.

As indicated in Figure 2.2, the motion of the EC wall is represented by a point source with the volume velocity $q_{w,s}$ splitting up the EC air volume into an upstream segment towards the EC entrance, and a downstream segment terminated by the TM (Carillo et al., 2020, 2021a; Hansen, 1998; Schroeter and Poesselt, 1986). The EC segments were modeled as lossless acoustical transmission lines represented by two-port matrices $\mathbf{K}_u$ and $\mathbf{K}_d$ (Hansen, 1998). The entries in $\mathbf{K}_u$ were obtained as (Lampton, 1978)

$$\mathbf{K}_u = \begin{pmatrix} \cos kl_u & jZ_0 \sin kl_u \\ \frac{j}{Z_0} \sin kl_u & \cos kl_u \end{pmatrix}, \tag{2.12}$$

with wave number $k = 2\pi f/c_0$, characteristic impedance $Z_0 = \rho_0 c_0/(\pi r_{ec}^2)$, the speed of sound in air $c_0 = 343$ m/s, and the density of air $\rho_0 = 1.2$ kg/m^3. The length of the upstream and of the downstream segments, l_u and l_d, were set to 8 mm and 19.7 mm, which led to an appropriate agreement of the circuit-calculated TM pressure with corresponding FE results (see Appendix A.2). $\mathbf{K}_d$ was calculated according to Equation 2.12 with l_d instead of l_u. It is worth noting that using lossless transmission lines to model the EC acoustics assumes the air's inertia or compliance effect to be dominant compared to the viscous and thermal losses. Carillo et al. (2020) showed that these losses do not significantly influence the sound pressure and volume velocity flow in the EC within the considered frequency range. The volume velocity transfer in direction to the wall due to its vibration is accounted for by $q_{w,s}$ according to Equation 2.2.

At the TM, the impedance Z_{tm} was taken from Shaw and Stinson (1983). It was implemented according to the values given in Schroeter and Poesselt (1986). Z_{tm} exhibits a resonance at about 900 Hz, below it acts as a compliance. Two occlusion conditions were considered at the EC entrance. For the first condition, a perfect occlusion was modeled with setting Z_e^{occl} to infinity. The second occluding condition represents a vented earplug with a hole of 0.9 mm radius and 21 mm length. This condition was already used for the circuit calculations by Carillo et al. (2021a) for comparison with experimental data by Hansen (1998) (the here called "vented" condition is termed "partially occluded" in Carillo et al. (2021a)).

The air in the vent, the air in the EC, and the TM compliance form a Helmholtz resonator with a resonance frequency of about $900\,\mathrm{Hz}$ (Carillo et al., 2021a). For the corresponding calculations, the same volume velocities $q_{\mathrm{w,s}}^{\mathrm{occl}}$, $q_{\mathrm{e,s}}^{\mathrm{occl}}$, and $q_{\mathrm{tm,s}}^{\mathrm{occl}}$ as for the perfectly occluded case were used.

The radiation impedance $Z_{\mathrm{e}}^{\mathrm{open}}$ at the EC entrance for the open ear was obtained from the FE model by an accompanying simulation with a piston-like excitation at the entrance plane towards the exterior of the head. For this simulation, the "perfectly matched layer", which allows a free field radiation without reflection, was used as described in Xu et al. (2021), and the head surfaces were modelled as acoustically rigid. $Z_{\mathrm{e}}^{\mathrm{open}}$ is inertia dominated within the inspected frequency range.

2.3 Results

In Figure 2.3, the OE calculations for an EC motion, which accounts for both the vibration of the EC wall and the motions of the EC entrance and TM, and when only considering the EC wall contribution are shown for (a) a perfectly occluded and (b) a vented EC. In Figure 2.4, to illustrate the influence on the sound pressure at the TM itself, the level differences between the calculations of the sound pressure including both mechanisms and exclusively accounting for the wall vibration are presented. These level differences were computed from the ratio $q_{\mathrm{tm,diff}}/(T_{\mathrm{w}}q_{\mathrm{w,s}})$ for (a) the open, (b) perfectly occluded and (c) vented EC entrance conditions. In Figure 2.5, the relative contributions $T_{\mathrm{w}}q_{\mathrm{w,s}}$ (orange), $T_{\mathrm{e}}q_{\mathrm{e,s}}$ (green), and $T_{\mathrm{tm}}q_{\mathrm{tm,s}}$ (purple) are shown normalized to their sum $q_{\mathrm{tm,diff}}$ (see Equation 2.9). These curves represent the contributions of the motion associated with the wall, the EC entrance, and the TM to the sound pressure at the TM.

The narrowband data extracted from the FE simulations exhibit strong resonances, especially at the lowest frequencies below $300\,\mathrm{Hz}$ (see Figure A.1 in Appendix A.1). To better illustrate the general trends, the results were calculated from third octave band averages of the overall volume velocities $q_{\mathrm{tm,diff}}^{\mathrm{open}}$ and $q_{\mathrm{tm,diff}}^{\mathrm{occl}}$ in Figure 2.3 (the numerator and denominator in Equation 2.10), and of the contributors $T_{\mathrm{w}}q_{\mathrm{w,s}}$, $T_{\mathrm{e}}q_{\mathrm{e,s}}$, and $T_{\mathrm{tm}}q_{\mathrm{tm,s}}$ as well as of their sum $q_{\mathrm{tm,diff}}$ in Figure 2.4 and Figure 2.5. The center frequencies were chosen according to *IEC 61260-1* (2014).

2.3.1 Wall vibration only

The results for the OE only based on the vibration of the EC wall depicted in Figure 2.3 (orange lines) were calculated according to Equation 2.11. The curves
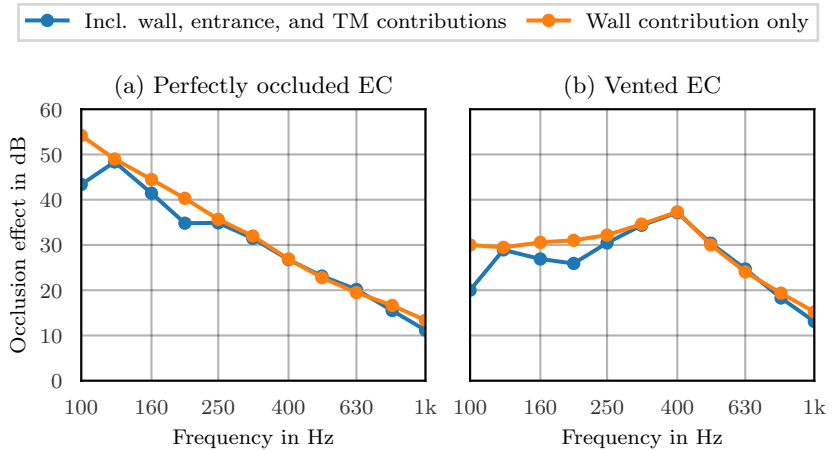
Figure 2.3: OE calculations for an EC motion including both the vibration of the EC wall and the motions of the EC entrance and TM according to Equation 2.10 (blue), and the OE calculated solely from the vibration of the EC wall according to Equation 2.11 (orange). The OE is computed based on third octave band averages, and given for the perfectly occluded and vented EC entrance.
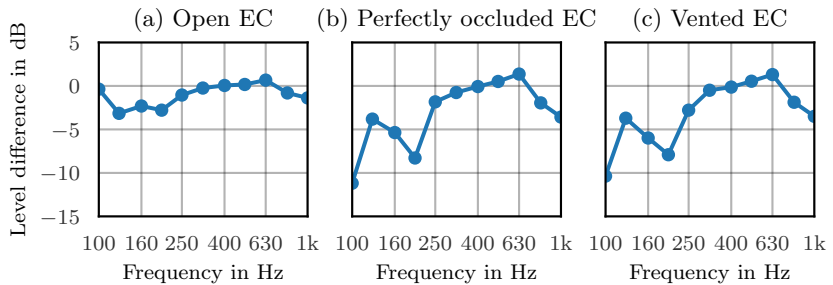

Figure 2.4: TM sound pressure level difference between the calculation for an EC motion, which accounts both for the vibration of the EC wall and the motions of the EC entrance and TM, and the calculation exclusively considering the wall's contribution. The level differences are computed from third octave band averages and is provided for the open, perfectly occluded and vented EC entrance conditions.
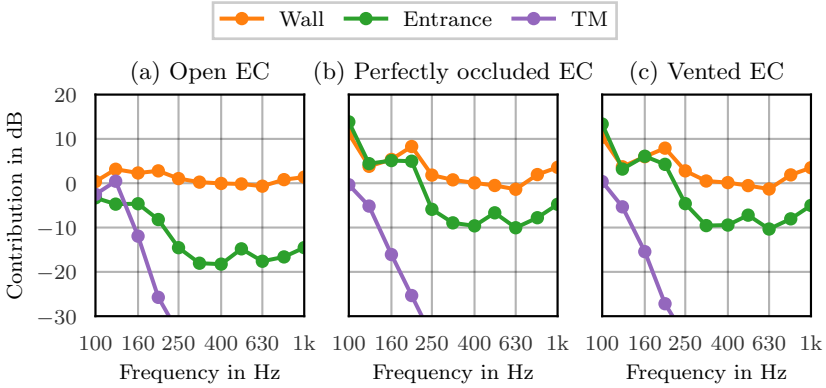
Figure 2.5: Volume velocity contributions of the EC wall, entrance and TM the TM sound pressure. Following Equation 2.9, the figure illustrates the three terms $T_{\mathrm{w}}q_{\mathrm{w,s}}$ (orange), $T_{\mathrm{e}}q_{\mathrm{e,s}}$ (green), and $T_{\mathrm{tm}}q_{\mathrm{tm,s}}$ (purple) normalized to their sum $q_{\mathrm{tm,diff}}$ for the open (left), perfectly occluded (center), and vented EC (right) scenarios. These ratios are based on third octave band averages, respectively.

resemble the results in Carillo et al. (2021a, Figure 5) with the small distinction that here the difference between the volume velocities $q_{\mathrm{w,s}}^{\mathrm{open}}$ and $q_{\mathrm{w,s}}^{\mathrm{occl}}$, which was below 2 dB throughout the whole frequency range of interest, is accounted for. The related mechanisms are briefly summarized in the following. This will help to understand the additional effects when the contributions of the EC entrance and TM are accounted for in the subsequent section.

For the perfectly occluded EC in Figure 2.3 (a), the OE exhibits the well known second order low-pass filter characteristic (Carillo et al., 2021a). It can be explained by the variation of the volume velocity transfer from the wall towards the TM, which determines the OE according to Equation 2.11 for the case of $q_{\mathrm{w,s}}^{\mathrm{open}} \approx q_{\mathrm{w,s}}^{\mathrm{occl}}$ given here. In the open case, the wall's volume velocity is mainly transferred towards the EC entrance due to the low impedance of the inertia of the air in the upstream section and of the EC entrance. With increasing frequency, this transfer is reduced due to the increase of the inertial impedance, and the decreasing impedance of the TM and downstream air compliance. In the occluded case, the transfer of the volume velocity towards the TM is constant with frequency due to the pressure chamber effect of the compliant EC volume, resulting in the low-pass characteristic of the OE (Carillo et al., 2021a).

The vent at the EC entrance causes a reduction of the OE compared to the perfect occlusion, because it allows for a volume velocity transfer from the EC

wall through the vent instead of towards the TM below the Helmholtz resonance [cf. Figure 2.3 (b)]. The OE is constant with frequency within this frequency range. Above the resonance, the air in the vent occludes the EC entrance, so the OE for vented EC entrance and for the case of perfect occlusion follow a similar trend.

2.3.2 Including contributions of the entrance plane and tympanic membrane

The OE results in Figure 2.3 (blue lines) represent an illustrative example with considering both the wall vibration and the motions of the EC entrance plane and the TM. In contrast to the prevalent assumption in OE simulations, which predominantly considers wall vibration alone (orange lines), the OE is reduced in the 100 Hz, 160 Hz and 200 Hz third octave bands, while the curves are similar at other frequencies. This OE reduction can in principle be attributed to changes in the open or occluded ear sound pressure. Therefore, Figure 2.4 shows the effect of the contributions of the EC entrance and TM to the TM sound pressure itself, examined for the scenarios with (a) open EC, (b) perfectly occluded EC, and (c) vented EC. In contrast to sound pressure calculated solely from the vibration of the EC wall, a reduction is observed in the lowest frequency range. However, this reduction is more pronounced in the occluded conditions compared to the open ear, which results in the reduction of the OE shown in Figure 2.3.

   Figure 2.5 helps to identify the underlying mechanisms which explain the difference of the effect between the open and occluding conditions on the TM sound pressure. Figure 2.5 shows the relative contributions of the three distinct volume velocities associated with the wall (depicted in orange), the EC entrance (green), and TM (purple) to the resulting sound pressure at the TM. In the case of the open ear, the wall's contribution predominantly influences the TM pressure above 250 Hz [as shown in Figure 2.5 (a)], as it closely approaches 0 dB. In the 125 Hz, 160 Hz and 200 Hz third octave bands, the wall's contribution exhibits a magnitude slightly greater than 0 dB, which indicates a partial cancellation by the TM's contribution at 125 Hz and by the entrance's contribution at 160 Hz and 200 Hz. Interestingly, the entrance's and TM's contribution cancel each other at 100 Hz, resulting in the wall's contribution to be dominant. Consequently, the difference in Figure 2.4 (a) is relatively small except between 125 Hz and 200 Hz, where accounting for motion of EC entrance and TM reduces the TM sound pressure by approximately 3 dB.

   For the perfectly occluded and vented conditions, the wall's contribution predominates only for frequencies higher than approximately 250 Hz [Figure 2.5 (b) and (c)]. Below 250 Hz, the entrance's and the wall's contributions are similar in

magnitude. What is noteworthy here is that both contributions exhibit a magnitude greater than 0 dB, signifying their partial cancellation in this frequency range. Conceptually, this can be visualized as the rigid EC entrance plane moving together with the attached wall, but with different surface orientations. This type of motion leads to an overall reduction of the volume velocity when these contributions are summed (see also explanations on Equation 2.2). Consequentially, the occluded TM pressure is reduced. This phenomenon is very similar for the two cases of perfect occlusion and a vented EC entrance considered here. Accordingly, when only accounting for the wall's contribution for the OE (orange line in Figure 2.3), this effect, stemming from the reduction of the wall's contribution due to the motion of the entrance plane, is omitted. This omission leads to an overestimation of the predicted occluded sound pressure.

Notably, in all three cases, the contribution linked to the motion of the TM with the surrounding bone remains small, except at the lowest considered frequencies below 125 Hz (purple lines in Figure 2.5). This phenomenon can be attributed to the different materials surrounding the EC. At the lowest frequencies inspected, the EC exhibits a rigid-body motion as a whole. But already above approximately 125 Hz, the EC section surrounded by soft tissue and cartilage exhibits a higher amplitude of the motion than the bony part attached to the TM. Consequently, the resulting volume velocity associated with the TM remains significantly smaller in magnitude when compared to the volume velocities linked to the wall and the EC entrance plane. The only exception is the 125 Hz band with open ear, where the volume velocity associated with the motion of the TM partially cancels the effect of the wall vibration on the TM pressure.

Another illustration of the mechanisms is provided with the help of the circuit in Figure 2.2. The three sources are connected to two branches each, with one portion of the volume velocity flowing towards the TM – encompassed by the volume velocity transfer functions – and another portion directed towards the EC entrance. The high impedance at the EC entrance for the two occluding conditions causes the portion towards the EC entrance to be relatively small. This leads to $|T_\mathrm{w}^\mathrm{occl}| \approx |T_\mathrm{e}^\mathrm{occl}| \approx |T_\mathrm{tm}^\mathrm{occl}|$, allowing the partial cancellation of the wall's contribution by the entrance's contribution below 250 Hz, due to their phase difference related to the surface orientations. In contrast, for the open-ear condition, the air in the EC is divided into an upstream and a downstream section (Carillo et al., 2020, 2021a; Hansen, 1998; Schroeter and Poesselt, 1986) connected to the low radiation impedance at the EC entrance. This division results in different ratios of the volume velocity portions transmitted towards the EC entrance and TM for each of the sources. Most significantly, it leads to $|T_\mathrm{e}^\mathrm{open}| < |T_\mathrm{w}^\mathrm{open}|$. Consequently, the effect of the entrance's contribution to

cancel the wall's contribution is smaller for the open compared to the occluded conditions, illustrated by comparing the green lines in Figure 2.5.

2.4 Discussion

2.4.1 Comparison to experimental findings

The differences for both the perfectly occluded and vented EC entrance highlight that the magnitude and filter characteristic of the OE potentially varies depending on the EC motion. Especially, the considered example indicates that a reduction of the OE towards the lowest frequencies compared to the second order low-pass filter characteristic (Carillo et al., 2021a) can be related to non-deforming motion of parts of the EC (cf. Figure 2.3) – which was not accounted for at the EC entrance and TM in previous studies of the topic. Indeed, comparisons between experimental data obtained from EC sound pressure measurements and OE simulations (Brummund et al., 2014; Carillo et al., 2021b; Xu et al., 2021) reveal an overestimation of the OE in particular at frequencies below 250 Hz.

Reinfeldt et al. (2013) found a higher variance of the OE obtained from EC sound pressure measurements for ipsilateral mastoid stimulation with a BC transducer at lowest frequencies compared to other positions on the skull, and stated that this could be related to the elastic part of the EC being closer to the ipsilateral position. Saint-Gaudens et al. (2022) reported the same effect comparing ipsi- and contralateral stimulation, while the variance was comparable with mastication as BC stimulation. The OE calculation with stimulation at the mastoid reveals the influence in the same frequency range where the higher variance is observed in the measurements. It is likely that the numerous factors listed in Section 1.2 result in variations of the EC motion. Accordingly, it is plausible that the mechanisms considered within this chapter, which are related to the EC motion, contribute to the observed variance of the open or occluded sound pressure (cf. Figure 2.4) and of the OE (cf. Figure 2.3).

2.4.2 Simulation of the occlusion effect

Figure 2.3 highlights the effect of considering the motions of the EC entrance and TM on the OE simulation. Accordingly, additional parameters $q_{e,s}$ and $q_{tm,s}$ (cf. Equation 2.10) could improve the prediction of the sound pressure in the EC and the OE with circuit models. However, the values of $q_{w,s}$, $q_{e,s}$ and $q_{tm,s}$ depend on

- the EC geometry,
- the orientation and magnitude of the excitation,

- the areas associated with the volume velocity sources, and
- the material properties of the EC surroundings.

More experimental and numerical studies are needed to investigate the EC motion in more detail in the future, e.g., in terms of the spatially distributed EC wall vibration (as already pointed out by Carillo et al. (2021b)). This is also indicated by a remaining difference of the open-ear pressure between the FE simulation and circuit calculation given in Figure A.2 in the appendix. This difference can potentially be mitigated by considering the frequency-dependent nature of the velocity distribution, particularly in terms of its centroid position (Carillo et al., 2021b). For the circuit calculations conducted within this chapter, a constant centroid position with frequency was assumed.

Within numerical models, one should be aware that applying the TM impedance locally as specific acoustic impedance deviates from the original one-dimensional formulation (see detailed discussion by Hudde and Engel (1998a)). Furthermore, the pressure distribution in the EC – especially close to the TM (Hudde and Schmidt, 2009; Rabbitt and Holmes, 1988) – and the deformation of the TM is generally complex at higher frequencies than about 1–1.5 kHz (Rosowski et al., 2009; Tonndorf and Khanna, 1972). Therefore, it is reasonable to replace the impedances, for example, by accounting for the coupling of the EC with the external air at the EC entrance (Xu et al., 2021) or by including middle and inner ear structures at the TM (Lim et al., 2022). Though this allows extending the frequency range of the OE simulations, it increases the model complexity and the computational effort. Yet, both circuit and FE models have been shown to be useful to investigate the OE using acoustic impedances (see, e.g., Carillo et al. (2020) for a comparison). The proposed extension of the impedance boundary condition could help to improve such OE simulations by accounting for non-deforming motion of parts of the EC.

2.4.3 Limitations and suggestions for future work

In the FE simulations and circuit calculations presented in this chapter, an impedance was applied at the EC entrance plane instead of modeling an occluding device as solid material. This approach excluded effects unrelated to impedance, such as variations in the radiating area (Dillon, 2012b; Stenfelt and Reinfeldt, 2007), mechanical loading on the EC wall (Denk et al., 2022; Dillon, 2012b; Hansen, 1998), and radiation from the medial surface of the occluding device (Carillo et al., 2021b). While this simplification limits this work's ability to predict the exact occluded sound pressure in the EC, it enables a focused investigation of the motion of the occluding device due to its connection with surrounding structures. Similarly, the open EC entrance was considered using

a radiation impedance. However, using the same FE model of a human head as for this investigation, Xu et al. (2021) compared OE simulations between a setup with a radiation impedance at the EC entrance and an infinite surrounding acoustic domain directly coupled to the EC cavity (see their Figure 8). Additional simulations incorporating the impedance boundary condition according to Equation 2.1 confirmed their finding that the sound radiation of head vibrations into the open EC can contribute to TM sound pressure, especially at the lowest frequencies (refer to Appendix A.3 for more details).

Accordingly, the present considerations highlight that at least three influencing factors that contribute to the deviation of the OE from a second order low-pass filter characteristic:

- vents of the occluding device or leaks at the EC entrance,
- radiation of BC-stimulated sound into the open EC, and
- non-deforming motion of parts of the EC.

Additional mechanisms influencing TM sound pressure include sound radiation from the earplug (Carillo et al., 2021b) and BC sound transmission through the ME into the EC (Stenfelt et al., 2003b). These effects were excluded here to focus on the role of the structural motion of the EC. The present example underscores the importance to distinguish between these mechanisms. However, it remains challenging to predict their effect on the resulting EC sound pressure and OE in advance, because the contributions of these mechanisms vary depending on whether the EC is open or occluded, as exemplified in Figure 2.5. Moreover, the analysis considered the EC motion only in a specific head model for a particular BC stimulation at the mastoid. The variability of these mechanisms in relation to factors such as the type of stimulation or the individual EC geometry remains unexplored. A more comprehensive investigation into these complexities could be a valuable pursuit for future research.

2.5 Summary

This chapter highlights the impact of a non-deforming motion of parts of the EC on the sound pressure at the TM and the resulting OE. This type of motion causes the EC entrance and at the TM to move with their surrounding structures. As a result, these boundaries' contributions complement the vibration of the EC wall in serving as the source of the BC stimulated sound pressure in the EC, particularly at the lowest frequencies. An impedance boundary condition was proposed, which incorporates this phenomenon by including a term to consider the structural motion of the adjacent solids at EC entrance and TM. When applied to OE models, the effect of this motion depends on two key factors:

firstly, the volume velocity transfer from the boundaries represented by acoustic impedances to the TM, which varies based on the open or occluded condition at the EC entrance, and secondly, the frequency-dependent, three-dimensional motion of the EC itself. To illustrate the related mechanisms, an example motion with BC stimulation at the mastoid was extracted from a FE model of a human head. This motion was employed as input for circuit calculations, considering perfectly occluded and vented EC scenarios.

The results revealed that the motions of the EC entrance and TM due to non-deforming adjacent EC parts – which is addressed by the proposed extension – can contribute to a reduction of the TM sound pressure at the lowest frequencies compared to when solely accounting for the vibration of the EC wall. This impact was found to be more pronounced when the EC is occluded, leading to a concurrent reduction of the OE. The mechanisms associated with the motions of the occluding device and the TM offer a plausible explanation of the higher variance of experimental OE data, and may contribute to deviations between OE simulations and experimental data below 250 Hz.

The considered EC motion highlights the importance of discerning between multiple mechanisms that contribute to the sound pressure at the TM in open or occluded scenarios. Yet, a more detailed knowledge on the EC motion and its influencing factors is needed to determine the relative contributions of the various effects and their degree of variability. Moreover, the objective assessment of the OE in the EC does not fully capture its subjective experience, due to the additional BC pathways involved in perception. Therefore, further investigations into the AC and BC pathways and their interactions within the inner ear are necessary.

<div style="text-align: right; font-size: 3em; font-weight: bold;">3</div>

Influence of the cochlear partition's flexibility for input at the oval window

3.1 Introduction

The previous chapter focuses on the vibroacoustic mechanisms underlying sound generation in the EC. Along with AC sound and the ME component of BC, these sounds enter the inner ear via the OW, where they interact with the inner ear's response to vibrations of its surrounding structures (Tonndorf, 1968), collectively generating neural signals that give rise to the sensation of hearing. Understanding the perception of sound, therefore, requires an analysis of the inner ear's vibroacoustic behavior, as it serves as the sensor for all AC and BC pathways. To contribute to this understanding, the following two chapters investigate cochlear macro mechanisms using a numerical, anatomical model of the human inner ear, illustrated in Figure 3.1

A central focus of these investigations is the flexibility and motion of the CP, which comprises the OSL, BM and CPB (cf. Figure 3.1). Despite the potential impact of CP flexibility and motion on AC and BC hearing (Békésy, 1960; Kohllöffel, 1983; Raufer et al., 2019; Stenfelt et al., 2003a; Taber and Steele, 1981), most existing models of the inner ear oversimplify these structures. For example, anatomical FE models of human inner ears (Böhnke and Arnold, 1999; Kim et al., 2014; Lim et al., 2022; Ren et al., 2021; Taschke, 2005) have typically assumed a rigid OSL and neglected the presence of the CPB, thereby aligning with the classical view of cochlear mechanics (Raufer et al., 2019). Additionally, experimental data on the OSL and the combined CP motion are sparse and spatially limited. Consequently, the role of CP's flexibility remains largely unexplored, leaving a gap in our understanding of hearing.

The numerical simulations presented here model the OSL and CPB as either rigid or flexible structures, enabling an identification and three-dimensional analysis of the associated macro mechanisms. This chapter focuses on stimulation via the OW, with the surrounding structures of the inner ear held fixed. This approach offers insights into cochlear impedances (Frear et al., 2018), CP stiffness (Békésy, 1960), and CP motion (Gundersen et al., 1978; Raufer et al., 2019; Stenfelt et al., 2003a). The subsequent Chapter 4 extends this analysis to also include vibrational stimulation of the cochlear surroundings, focusing on the role of OSL in affecting inner ear fluid flow (Stenfelt et al., 2004a).

3.2 Methods

3.2.1 Finite element model

Geometry

The geometry of the inner ear model, depicted in Figure 3.1, includes fluid-filled domains (blue) representing the vestibule, semicircular canals, helicotrema, SV, and ST. In this model, the scala media is encompassed by the SV, assuming negligible effects from Reissner's membrane, which separates the SV and scala media, consistent with common modeling approaches (e.g., Gan et al., 2007; Kim et al., 2011, 2014; Koike et al., 2012; Motallebzadeh et al., 2018; Ren et al., 2021; Stenfelt, 2015). The CP separates SV and ST, with the CPB (red) and BM (purple) boundary surfaces connecting the OSL with the SL (brown). The OSL was modelled as a sandwich-like structure, with the VP and TP (green) represented as two thin solid plates separated by a solid core (orange) with soft tissue properties. In real ears, small, randomly distributed bony pillars connect the VP and TP (Bom Braga et al., 2023; Raufer et al., 2019). This feature was approximated by connecting the plates along their lateral edge. On the medial side, the OSL domain is bounded by a surface aligned with the innermost part of the SV and ST (refer to Figure 3.1). The entire inner ear geometry, except for the OW and RW, is embedded in a surrounding block of solid material [depicted as the gray area in Figure 3.1 (b)].

The widths of the BM and CPB each range from approximately 120 μm at the base to around 470 μm at the helicotrema, while the OSL width reaches values of 1000–1300 μm in the basal region and narrows to 250–470 μm near the apex. These values align well with those obtained from histological sections by Raufer et al. (2020, Figure 2 and Table 1). To integrate the material properties and thicknesses of the BM, the CPB, the VP, and the TP, shell physics was assigned to these boundaries, allowing for the independent specification of these parameters relative to the adjacent domains.
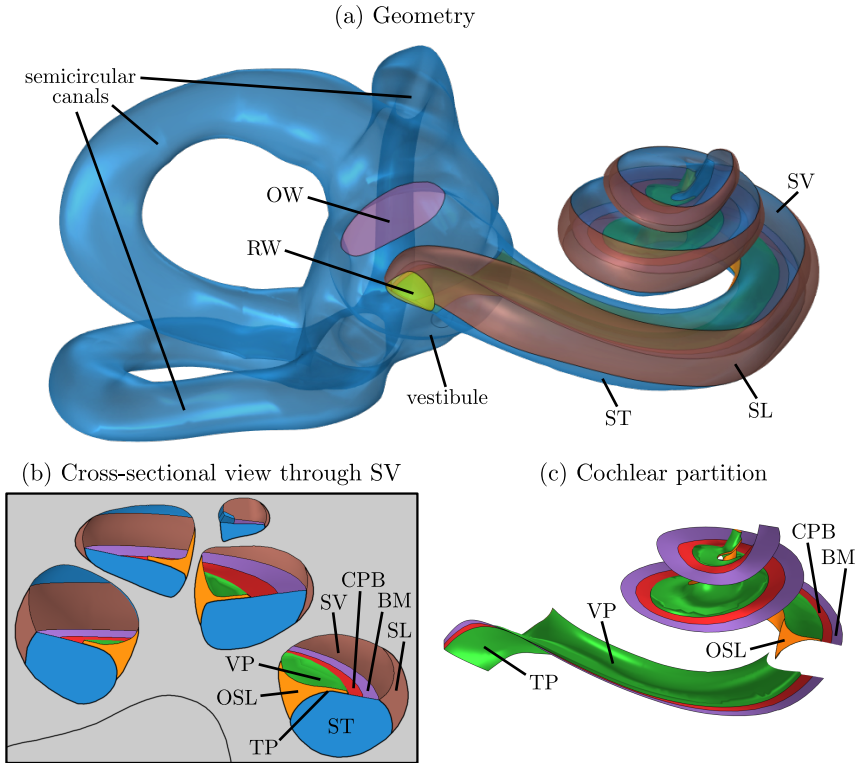
(a) Geometry

(b) Cross-sectional view through SV   (c) Cochlear partition

Figure 3.1: Geometry of the inner ear model and its CP. The vestibule, semicircular canals, SV, and ST were considered as fluid domains (blue). The OSL (orange/green) and spiral ligament (SL) (brown) were modeled as solid domains. Shell physics was assigned to the RW (olive), VP and TP (green), CPB (red), and BM (purple). The OW is shown in pink. Panel (c) includes a cutout of the CP to reveal its cross-sectional structure. For detailed views of CPs with cochlear microstructures not fully represented in this model, refer to Raufer et al. (2020).

The geometry of the model was originally created as part of the work by Taschke (2005) using a dataset of an inner ear, which included 75 grayscale images from serial sections of a temporal bone specimen with a slice thickness of 20 µm, each with a resolution of approximately 40 µm in the image plane and spaced 20–100 µm apart (cf. Taschke, 2005, p. 36). These images were provided by the Department of Otorhinolaryngology, Head and Neck Surgery at the University Hospital Zürich. Contours of the scalae, vestibule, and semicircular canals were segmented in the slices and reconstructed as non-uniform rational B-spline (NURBS) models, commonly used in computer graphics and computer-aided design (CAD). Uncertainties related to the unknown postmortem time, specimen conservation, and partial structural damage caused by slicing were mitigated by integrating prior anatomical knowledge (Anson and Donaldson, 1981; Gray and Lewis, 1918), as described in Taschke (2005, Section 4.2). For the investigations presented in this thesis, the original geometry was refined to incorporate more recent detailed anatomical information (Agrawal et al., 2018; Atturo et al., 2014a, 2014b; Bom Braga et al., 2023; Cohen et al., 2005; Li et al., 2007; Raufer et al., 2019, 2020; Wright and Roland, 2018). These adjustments included enhancements at the helicotrema, cochlear base, RW, OSL, and CPB.

Material properties

The material properties of the model, along with their respective references, are summarized in Table 3.1. These parameters were derived from experimental sources and other models where possible, and reasonable values were assumed where no references were available.

Soft tissues were assigned a density of $1000\,kg/m^3$ (Kim et al., 2014) and a Poisson's ratio of 0.45, reflecting their nearly incompressible nature. The VP and TP were assigned a Young's modulus and density of $8\,GPa$ and $1800\,kg/m^3$, considering average data for temporal bone (Auperrin et al., 2014), and a Poisson's ratio of 0.3. The thickness of the plates ($10\,µm$) was determined based on the anatomical images by Raufer et al. (2020) and Bom Braga et al. (2023). For the OSL core (orange in Figure 3.1), a Young's modulus of $30\,kPa$ was assumed to reflect soft tissue properties (Akhmanova et al., 2015), accounting for the tissue and nerve fibers between the two plates (Bom Braga et al., 2023; Raufer et al., 2020). In real ears, the OSL is semi-permeable, with varying porosity of the VP and TP depending on lateral and longitudinal position and differing across specimens (Bom Braga et al., 2023). Since including these complexities was not feasible, the material properties were assigned to approximate these characteristics. However, the findings should be interpreted considering this simplified representation of the OSL.

Material	Property	Value		Reference
VP and TP	E	8000	MPa	Auperrin et al. (2014) (temporal bone)
	ρ	1800	kg/m^3	Auperrin et al. (2014) (temporal bone)
	ν	0.3		Chang et al. (2016) (cortical bone)
	η	0.3		Lim et al. (2022) (cortical bone)
	d	10	µm	images in Bom Braga et al. (2023) and Raufer et al. (2020)
OSL	E	0.03	MPa	assumed, cf. Akhmanova et al. (2015)
	ρ	1000	kg/m^3	
	ν	0.45		
	η	0.5		
BM/CPB	E_r	3500×0.5^{u_s}	MPa	assumed, cf. Yang et al. (2008)
	E_s	$E_r/100$		
	G_{rt}	$E_s/10$		
	ν_{rs}, ν_{st}	0.45		
	ρ	1000	kg/m^3	
	η	0.1		
	d_{bm}	$6.3 \times \exp(-5.8u_s) + 0.8$	µm	Bhatt et al. (2001) (fit of average)
	d_{cpb}	$20 - [20 - d_{\mathrm{bm}}(u_s)] \times 2u_r$	µm	cf. images in Raufer et al. (2020)
RW	E	0.2	MPa	matching Z_{rw} (Frear et al., 2018)
	ρ	1000	kg/m^3	Koike et al. (2012) and Ren et al. (2018)
	ν	0.45		
	η	0.3		matching Z_{rw} (Frear et al., 2018)
	d	70	µm	Goycoolea and Lundman (1997)
SL	E	E_r		
	ρ	1000	kg/m^3	
	ν	0.45		
	η	0.5		
Cochlear fluid	c	1500	m/s	Kim et al. (2011)
	ρ	1000	kg/m^3	Kim et al. (2011)

Table 3.1: Material properties assigned to the domains and boundaries in the model. E: Young's modulus, ρ: density, ν: Poisson's ratio, η: structural loss factor, d: thickness, c: speed of sound. The longitudinal and radial CP coordinates u_s and u_r are illustrated in Figure A.4 in Appendix A.4.

The mechanical characteristics of the BM and CPB, primarily determined by the radial collagen II fibers (Békésy, 1960; Liu et al., 2015; Raufer et al., 2020), were represented by the properties of the shell structure. The inhomogeneity, the anisotropy, and the varying thickness were implemented by adjusting the material properties and thickness of the shell along the CP (Gan et al., 2007; Kim et al., 2011, 2014; Koike et al., 2012; Ren et al., 2021) as functions of curvilinear longitudinal and radial coordinates (u_s and u_r), which were obtained by numerically solving differential equations (see Appendix A.4 for details). Assuming the radial fibers to be transversely isotropic requires specifying five parameters (Fleischer et al., 2010; Ren et al., 2021). To cover the audible frequency range, the Young's modulus E_r in the direction of the fibers was made a function of distance along the CP (Kim et al., 2011; Taschke, 2005) by utilizing the coordinate u_s (see Figure A.4 (a) in Appendix A.4 for an illustration of u_s). The values of E_r fall within reported ranges for collagen fibers (Heim et al., 2006; Yang et al., 2008). E_s (radial to the fibers' orientation) was set to $E_r/100$, the shear modulus G_{rt} to $E_s/10$, the Poisson's ratios ν_{rs} and ν_{st} to 0.45 (similar to Fleischer et al. (2010)), and the isotropic loss factor to 0.1. BM and CPB width were approximately equal (Raufer et al., 2020). Given spatially sparse data on the BM thickness (Bhatt et al., 2001; Liu et al., 2015; Meenderink et al., 2019), approximations were made based on values from Bhatt et al. (2001). CPB thickness was set to linearly increase from the BM thickness at the CPB-BM edge to 20 µm at the OSL-CPB junction. The thickness functions are given in Table 3.1. As it will be shown in Section 3.3, these parameters yielded plausible traveling wave propagation and tonotopic mapping (Greenwood, 1990), and BM velocities similar to measured curves (Raufer et al., 2019; Stenfelt et al., 2003a).

At the lateral side of the CP, the BM fibers fan out into the SL (Raufer et al., 2020), therefore the BM's radial Young's modulus E_r was assigned to the SL. The RW membrane thickness was set to 70 µm (Goycoolea and Lundman, 1997), with its properties determined to match experimental impedance data (Frear et al., 2018). The cochlear fluid was modeled as nearly incompressible with water-like properties (Kim et al., 2011).

To evaluate the impact of the OSL and CPB flexibility, either the OSL alone or both the OSL and CPB were rendered rigid by applying fixed boundary conditions to these structures in subsets of the simulations.

Active cochlear mechanisms (Dallos, 1992; Robles and Ruggero, 2001) and fluid viscosity, which has been shown to influence these active mechanisms and cochlear micromechanics (Motallebzadeh and Puria, 2021; Y. Wang et al., 2016), were not accounted for. However, since the results are compared with experimental data obtained from human cadaver ears, a linear modeling approach is considered appropriate. Additionally, this work focuses on cochlear macromechan-

ics, with microstructures associated with the BM and CPB effectively represented using shell physics. Consequently, the assigned loss factors (Table 3.1) should be interpreted as encompassing losses both in the fluid near the BM and CPB and within these structures themselves.

Given the specific geometry and set of material properties, it is important to consider that the numerical model used here should be viewed as representative of an individual specimen rather than a predictive model for average data when comparing the simulation results to experimental data in the following.

3.2.2 Stimulation and boundary conditions

A unit inward velocity was applied to the OW, approximating a piston motion of the stapes. The surroundings of the inner ear [gray in Figure 3.1 (b)] were assigned fixed boundary conditions. This normalized stimulation condition represents both AC sound and BC components entering through the OW, as both correspond to relative motion between the stapes footplate and the adjacent bone.

To determine the stiffness of the CP, a uniform sound pressure of $1\,\mathrm{Pa}$ at a frequency of $1\,\mathrm{Hz}$ was applied to the CP surfaces from the ST side. The pressure acoustics physics was deactivated in the model in this case, removing the load imposed by the fluid. This is equivalent to applying a uniform differential pressure across the CP, allowing for CP motion to be determined by its structural properties only. The frequency of $1\,\mathrm{Hz}$ was chosen to ensure excitation far below the resonance frequencies of the BM to obtain stiffness.

3.2.3 Evaluation quantities

Following experimental setups, such as those by Olson (1998), Nakajima et al. (2009) and Frear et al. (2018), intracochlear sound pressures p_{sv} and p_{st} were assessed using virtual sound probes at the corresponding locations in the SV and the ST, respectively. The differential sound pressure was then computed as $p_{\mathrm{diff}} = p_{\mathrm{sv}} - p_{\mathrm{st}}$ (Frear et al., 2018; Nakajima et al., 2009). Volume velocities q_{ow} and q_{rw} were determined by integrating the normal component of the acoustic particle velocity over the OW and RW boundaries, respectively. The impedance definitions followed Frear et al. (2018),

$$Z_{\mathrm{diff}} = p_{\mathrm{diff}}/q_{\mathrm{ow}}, \tag{3.1}$$

$$Z_{\mathrm{rw}} = p_{\mathrm{st}}/q_{\mathrm{ow}}, \tag{3.2}$$

$$Z_{\mathrm{c}} = p_{\mathrm{sv}}/q_{\mathrm{ow}} = Z_{\mathrm{diff}} + Z_{\mathrm{rw}}. \tag{3.3}$$

These definitions assumed $q_{ow} \approx q_{rw}$ and were evaluated similarly to facilitate comparison with experimental data, except for the method for obtaining q_{ow} and q_{rw}.

The CP velocity v_{cp} was assessed at the ST boundary of the CP (Raufer et al., 2019; Stenfelt et al., 2003a). Specifically, longitudinal velocity distributions were evaluated via linear interpolation of the simulation results at the radial BM center ($u_r = 0.75$) and the OSL-CPB junction ($u_r = 0$). Additionally, radial velocity profiles were examined at relative longitudinal distances of 0.03 and 0.3, which correspond to locations with available experimental data (Raufer et al., 2019; Stenfelt et al., 2003a), as well as at an additional position closer to the apex at 0.7 relative distance. The differential velocity between the BM center and OSL-CPB junction was assessed as the component-by-component difference between the velocity vectors at the same longitudinal distances u_s. The three complex-valued components of the CP and differential velocity vectors were condensed into single quantities by calculating the magnitude and phase of their maximum per unit cycle (Dobrev and Sim, 2018). Velocities were normalized to p_{diff}, viewed as the pressure initiating the traveling wave, or q_{ow}, regarded as the cochlear input, to enable comparison with experimental data (Gundersen et al., 1978; Raufer et al., 2019; Stenfelt et al., 2003a).

CP stiffness was calculated as $-\omega \, \mathrm{Im}\,(p_{cp}/\,[\mathbf{v}_s(\mathbf{x}) \cdot \mathbf{n}(\mathbf{x})])$ for the corresponding stimulation with a homogeneous pressure $p_{cp} = 1\,\mathrm{Pa}$ on the ST side of the CP at $\omega = 2\pi \times 1\,\mathrm{Hz}$. $\mathbf{v}_s(\mathbf{x}) \cdot \mathbf{n}(\mathbf{x})$ represents the local normal component of the structural velocity $\mathbf{v}_s(\mathbf{x})$ in the direction of the load at a position $\mathbf{x}$ on the CP.

3.2.4 Simulation parameters and post-processing

The simulations were conducted using Comsol Multiphysics® version 6.2, covering frequencies from 100 Hz to 10 kHz with a resolution of 24 frequencies per octave. Utilizing the software's default quadratic shape functions, the maximum element size of the triangular mesh on the BM/CPB boundary was set to 40 µm. The maximum element size of the remaining tetrahedral mesh was adjusted to ensure at least 5 elements per wavelength for 10 kHz, considering the bending wave speed on the shell boundaries, shear wave speed in the solid domains, and the speed of sound in the fluid domain. The mesh was kept the same for all frequencies. The total number of degrees of freedom for the full model with flexible OSL and CPB was approximately 3.2 million, the number was slightly reduced when these structures were considered fixed.

The evaluation quantities (see Section 3.2.3) were exported in .csv format and analyzed using custom Python scripts. The FE model, simulation results, and

Python code used for the analysis are provided at https://doi.org/10.5281/zenodo.13897016.

3.3 Results

3.3.1 Cochlear impedances

In Figure 3.2, cochlear impedance results are shown for the three conditions: flexible OSL and CPB (solid lines), rigid OSL and CPB (dashed lines), and rigid OSL alone (dash-dotted lines). These results are compared to experimental data from Frear et al. (2018) (individual data and mean for Z_{diff} and Z_{rw}), Aibara et al. (2001) (mean $\pm$ standard deviation for Z_{c}), and Nakajima et al. (2009) (mean $\pm$ standard deviation for Z_{c}).

Z_{diff} (left column) displays inertia-dominated behavior up to approximately 4 kHz for the rigid OSL and CPB condition (dashed line) and up to 3 kHz for the rigid OSL alone (dash-dotted line). Below 3 kHz, the curves are similar for both
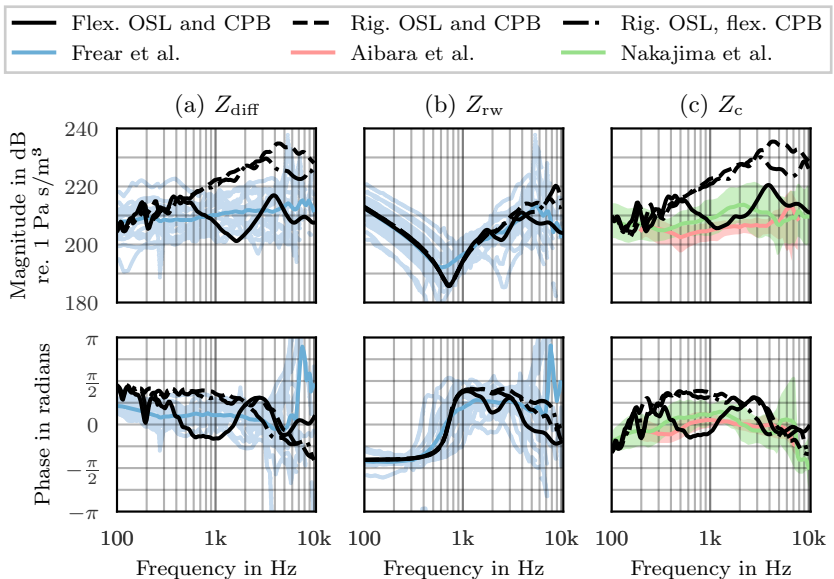
Figure 3.2: Magnitude and phase of cochlear impedances with flexible versus rigid OSL and CPB. For comparison, mean and individual data from Frear et al. (2018) are shown for Z_{diff} and Z_{rw}. Z_{c} is compared to experimental data by Aibara et al. (2001) and Nakajima et al. (2009) (mean $\pm$ standard deviation).

conditions. In both cases, the magnitude of Z_{diff} exceeds the experimental data between 800 Hz and 4 kHz. Experimental investigations have revealed that, on average, Z_{diff} exhibits resistive behavior with an additional inertial component at low frequencies (Frear et al., 2018). However, unlike a pure resistance, both the magnitude and phase of individual measured impedances vary with frequency (Frear et al., 2018; Nakajima et al., 2009). These characteristics observed in individual experimental data are replicated with flexible OSL and CPB (solid line), where Z_{diff} shows frequency-dependent variability in magnitude within a range of 15 dB and a phase alternating around zero with a tendency towards positive values at the lowest frequencies.

At frequencies below approximately 400 Hz, Z_{diff} exhibits similar behavior across all three conditions. However, between 400 Hz and 500 Hz, the presence of a zero crossing in the phase and a change in the slope of the magnitude with flexible OSL and CPB indicates a mass-spring resonance. The absence of this resonance in the two scenarios with rigid OSL suggests that it is primarily driven by the flexibility of the OSL rather than the CPB. At around 1.5 kHz, Z_{diff} undergoes another characteristic change, leading to a minimum in magnitude. This phenomenon is linked to a shift in the radial motion of the OSL at the base, as discussed in Section 3.3.3.

Z_{rw} in Figure 3.2 (b) resembles the experimental data, demonstrating the behavior of a spring-mass resonator (Frear et al., 2018). Above approximately 2 kHz, the variation in magnitude and phase among the individual experimental data becomes more pronounced. While positive phase values are observed with a rigid OSL and CPB, introducing flexibility to the OSL results in negative phase values. Notably, all three curves remain within the range of the experimental data.

The cochlear input impedance Z_{c} [Figure 3.2 (c)] is essentially a series connection of Z_{diff} and Z_{rw} [(a) and (b), respectively]. Since Z_{c} is primarily dominated by Z_{diff}, the differences between the flexible and rigid CP conditions correspond to those observed for Z_{diff}. With flexible OSL and CPB (solid line), Z_{c} generally aligns with the range of the experimental data reported by Aibara et al. (2001) and Nakajima et al. (2009). In contrast, for the two conditions with rigid OSL, the importance of the cochlear fluid is predicted to be high, as indicated by the phase being close to $\pi/2$ and the magnitude exceeding the experimental data range, particularly above 500 Hz.

3.3.2 Cochlear partition stiffness

Figure 3.3 shows the stiffness of the CP obtained by applying a uniform pressure on the CP at a frequency of 1 Hz while evaluating the normal velocity at the
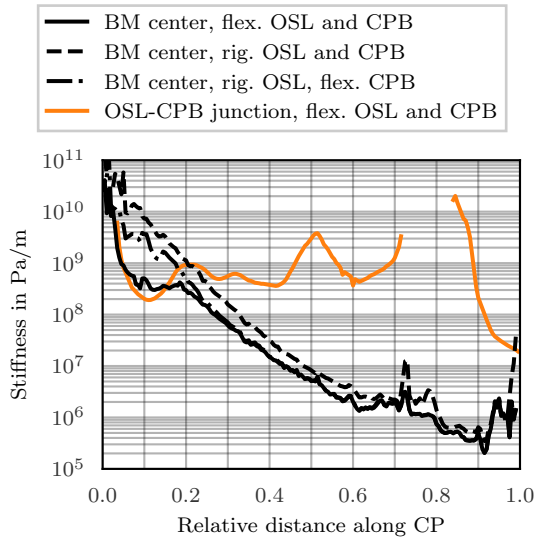
Figure 3.3: CP stiffness evaluated at radial BM center with flexible OSL and CPB (solid black line), rigid OSL and rigid CPB (dashed black line), and rigid OSL/flexible CPB (dash-dotted black line) along the CP. For comparison, the stiffness at the OSL-CPB junction with flexible OSL and CPB is shown in orange (note that it approaches infinity for the scenarios with rigid OSL).

radial center of the BM. The results are shown with flexible OSL and CPB (solid black line), rigid OSL and rigid CPB (dashed black line), and rigid OSL with flexible CPB (dash-dotted black line). For comparison, the CP stiffness at the OSL-CPB junction with flexible OSL is depicted in orange. Unlike the BM and CPB, the OSL does not react purely locally to the uniform pressure. Instead, it sometimes exhibits a lever-like motion, resulting in velocity in the opposite direction of the load for relative distances around 0.8, leading to non-meaningful stiffness values. Consequently, Figure 3.3 presents stiffness values at the OSL-CPB junction only where physically meaningful results were obtained under the pressure load. Note that for the scenarios with rigid OSL, the stiffness at this junction approaches infinity.

With both the OSL and CPB rigid (dashed line), the stiffness at the center of the BM is governed solely by the stiffness of the BM itself. Introducing the CPB as a flexible structure slightly reduces this stiffness at the BM center across all distances (dash-dotted line). In both scenarios, the stiffness gradually decreases from the base to the apex due to the increasing width and decreasing Young's

modulus of the BM/CPB section, along with the decreasing BM thickness (see
Section 3.2).

Interestingly, the flexibility of the OSL does not significantly influence BM
stiffness beyond positions apical to a relative distance of approximately 0.3 along
the CP (cf. black solid and dash-dotted lines). However, noticeable differences
emerge in the basal region, where BM stiffness (solid black line) resembles the
stiffness at the lateral edge of the OSL (orange line). This suggests that in this
region, CP stiffness is primarily influenced by the flexibility of the OSL rather
than the properties of the BM and CPB.

With flexible OSL and CPB, CP stiffness predominantly falls within the range
of 1×10^6–5×10^8 Pa/m. This aligns reasonably well with the range of 4×10^6–
1×10^8 Pa/m reported by Olson et al. (2012), derived from human cochlear data
at nine CP positions from Békésy (1960). In contrast, for the conditions with
rigid OSL, CP stiffness near the base reaches significantly higher values than
those observed with flexible OSL.

3.3.3 Cochlear partition motion

Velocity at specific positions

Figure 3.4 depicts the magnitude and phase of the CP velocity v_{cp} evaluated at
the radial center of the BM (black) and OSL-CPB-junction (orange), normalized
to the differential intracochlear pressure p_{diff} [(a)–(c)] and to the OW volume
velocity q_{ow} [(d)–(f)] at relative distances of 0.03, 0.3, and 0.7 along the CP.

Raufer et al. (2019) presented CP velocity data close to the cochlear base
for several radial positions normalized to the sound pressure in the vestibule.
As the sound pressure in the SV exceeds that in the ST at most frequencies
($Z_c > Z_{rw}$ in Figure 3.2), their data can be compared to the simulation results
regarding v_{cp}/p_{diff}. The blue line in Figure 3.4 (a) represents their data at the
radial center of the BM (specimen #16), with their position of 1 mm from the
base corresponding to a relative distance of about 0.03. The sign of the phase
was adjusted, so that a positive v_{cp} refers to a motion in the direction from SV
to ST following the definition of p_{diff} (refer to Section 3.2.3).

The results with flexible OSL and CPB (solid black line) are in reasonable
agreement with the experimental data at this position (blue), particularly when
considering the sensitivity of velocity magnitude to slight variations in both radial
and longitudinal directions near the base (see below for details). The magnitude
of the velocity consistently increases across the inspected frequency range, with
slopes of approximately 20 dB per decade below 1 kHz and above 1.5 kHz. This
increase suggests that the characteristic frequency for this position is above the
maximum inspected frequency of 10 kHz, consistent with Raufer et al. (2019),
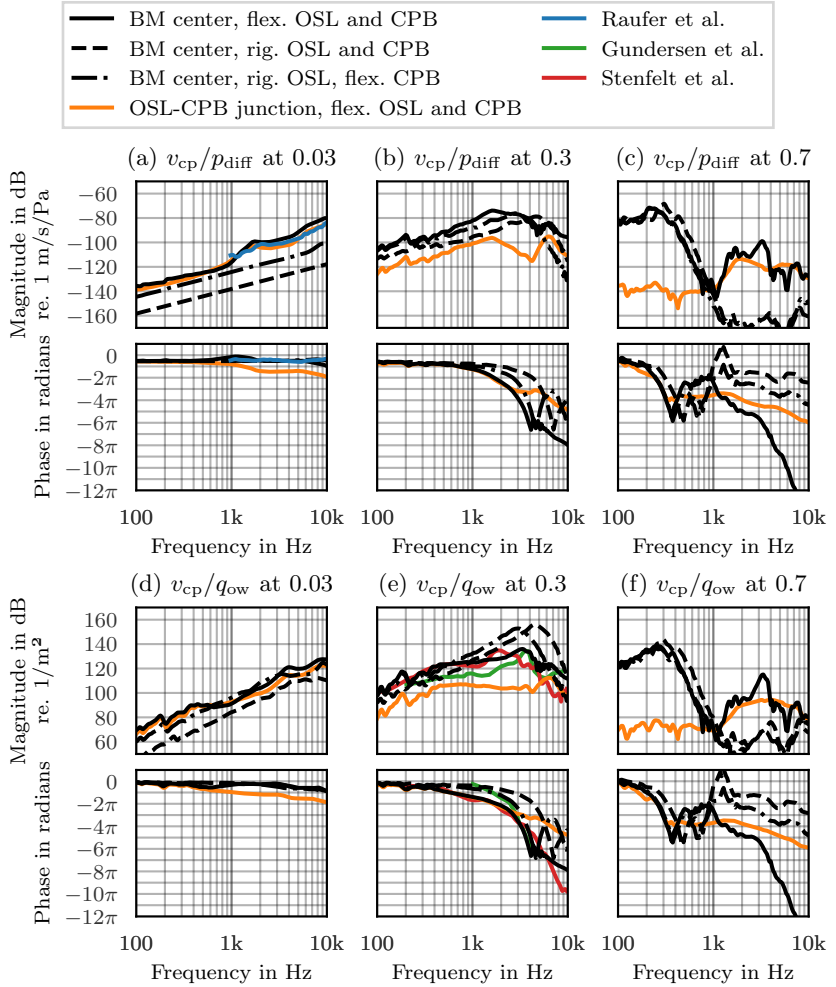
Figure 3.4: CP velocity v_{cp} normalized to differential cochlear pressure p_{diff} (top row), and OW volume velocity q_{ow} (bottom row) evaluated at relative distances of 0.03 (left), 0.3 (center), and 0.7 (right) along the CP. Solid black lines indicate results with a flexible OSL and CPB, dashed black lines with a rigid OSL and rigid CPB, and dash-dotted black lines with a rigid OSL and flexible CPB, each evaluated at the radial BM center. Solid orange lines indicate the velocity at the OSL-CPB junction with a flexible OSL (note that it equals zero in the scenarios with rigid OSL). The experimental data from Raufer et al. (2019) in (a) was measured close to the base at the radial center of the BM. The data from Gundersen et al. (1978) and Stenfelt et al. (2003a) at a distance 12 mm from base (corresponds to approximately 0.3 relative distance in the model) in (e) was recalculated following the method in Frear et al. (2018).

who reported characteristic frequencies between 9.5–14.4 kHz for this location in six temporal bone specimens. The curve with a rigid OSL and a flexible CPB (dash-dotted) is about 5 dB lower than the curve with flexible OSL and CPB below 1 kHz, and 15–20 dB lower above 1.5 kHz. This curve is about 15 dB higher than the curve with both rigid OSL and rigid CPB (dashed). Both curves with a rigid OSL show a constant slope with an increase of 20 dB per decade. The velocity at the junction of the flexible OSL with the CPB (orange) is nearly equal in magnitude to the velocity at the BM center for this condition below 1 kHz and about 5 dB lower above 1.5 kHz.

The nearly constant phase of about $-\pi/2$ in the experimental and simulation results at the BM center (black and blue lines) indicate a spring-like behavior at this position within the inspected frequency range. The phase difference of about π between the BM center and OSL-CPB junction above about 1 kHz indicates a change in radial motion with frequency at this position (see Section 3.3.3).

At a relative distance of 0.3 in Figure 3.4 (b), the magnitude curves for the rigid OSL (dashed and dash-dotted black lines) display a nearly constant slope of 20 dB per decade, increasing steadily before reaching peaks at approximately 5 kHz and 3 kHz, respectively, followed by a sharp decline. With a flexible OSL (solid black line), the magnitude exhibits a similar overall pattern, though with a slightly steeper increase between about 400 Hz and 1.5 kHz, a section of highest magnitude between 1.5–3 kHz, and an additional local maximum around 6.5 kHz approximately 10 dB below the overall maximum. The magnitude of the velocity at the OSL-CPB junction (solid orange line) shows an alternating slope with frequency, characterized by an increase below approximately 1.5 kHz and within the 4–6 kHz range, and a decrease in between and above these ranges.

For all three conditions, the rapid decrease in phase, particularly above 1 kHz, indicates traveling wave propagation in the BM (Zweig et al., 1976) and at the OSL edge (Stenfelt et al., 2003a). Comparing the phase response between the three scenarios, the lowest phase lag is achieved with both rigid OSL and rigid CPB. Including these structures as flexible each increases the phase lag. Compared to the radial BM center, the phase lag at the OSL-CPB junction (orange) is similar below the characteristic frequency, while the curves differ by about 4π above. In the two conditions with a rigid OSL, partial phase increases in phase are observed above approximately 4.5 kHz and 7 kHz. These increases result from the phase being too steep to be unwrapped accurately, given the frequency resolution of the simulation in this range.

At a relative distance of 0.7 in Figure 3.4 (c), the maximum magnitudes in BM velocity (black lines) are reached between 200–300 Hz, with an increase at lower frequencies and a sharp decrease above. When both the OSL and CPB are rigid (dashed line), the maximum shifts slightly towards higher frequencies compared

to the conditions with a flexible CPB. Accompanied by a decrease in phase up to approximately 400 Hz, these characteristics indicate the presence of a BM traveling wave in all three conditions. A distinct influence of the OSL becomes evident above 1 kHz, where its flexibility results in BM velocities 40 dB higher compared to the other two conditions. In this frequency range, the velocities at BM center and OSL-CPB junction (orange line) show similar curve shapes, while the velocity at the OSL edge remains approximately 60 dB below the BM velocity at low frequencies.

Between approximately 400–500 Hz and 1–2 kHz, the steepness of the phase data at the BM center causes inaccuracies in phase unwrapping for all three conditions. Above 2 kHz, with rigid OSL (dashed and dash-dotted black lines), the reduction in slope of the phase indicates a complete decay of the BM traveling wave (Zweig et al., 1976), corresponding to the magnitude fluctuating around 100 dB below the maxima. In contrast, the decrease in phase at both the BM center (solid black line) and OSL edge (orange line) in this frequency range indicates that traveling-wave behavior within the OSL significantly contributes to BM motion. Additionally, the phase difference between the positions is related to complex radial velocity patterns, inspected in more detail below.

While Figure 3.4 (a)–(c) show the ratio v_{cp}/p_{diff}, normalizing to the differential pressure that initiates the traveling wave, (d)–(f) depict the ratio v_{cp}/q_{ow}, where the CP velocity is divided by the OW volume velocity, considered as the cochlear input. This is equivalent to multiplying v_{cp}/p_{diff} by Z_{diff}. Consequently, the results in panels (d)–(f) not only reflect the CP velocities shown in (a)–(c) but also incorporate the frequency-dependent effects of the OSL and CPB flexibilities already present in Z_{diff}.

For comparison, experimental BM velocity data from Gundersen et al. (1978) and Stenfelt et al. (2003a) at a distance 12 mm from base are included in Figure 3.4 (e). This data was normalized to OW volume velocity by multiplying the stapes velocity by a factor of $3.22 \, mm^2$ based on the approach in Aibara et al. (2001), Nakajima et al. (2009), Frear et al. (2018). Similar curves in magnitude and phase were observed with flexible OSL and CPB (solid black line) at the relative distance of 0.3, which approximately matches their position.

With a rigid OSL (dashed and dash-dotted black lines), the magnitudes increase with frequency at a slope of 40 dB per decade, reaching maxima at the same frequencies as in panel (b). This increase results from the combined 20 dB slopes of the curves in panel (b) and Z_{diff}. Below 500 Hz, the magnitudes are similar between the three simulation conditions. However, with flexible OSL and CPB (solid black line), as well as in the experimental data (green and red), the magnitudes exhibit a nearly constant section between the initial at low-frequency rise and a second increase towards the maxima between 3 kHz

and 4 kHz, respectively, before sharply decreasing. By comparing the simulation results with the differential impedance in Figure 3.2 (a) and the CP velocity normalized to the differential pressure in Figure 3.4 (b), it is evident that the constant slope and the maximum observed between 3–4 kHz result from the characteristics of Z_{diff}, which combine with the traveling-wave characteristics evident in the BM velocity in Figure 3.4 (b). Particularly, the maximum in Figure 3.4 (e) corresponds closely to the peak at approximately 3.5 kHz in Z_{diff} seen in Figure 3.2 (a). The magnitude of the velocity at the OSL-CPB junction (solid orange line) is approximately 10 dB below the velocity at the BM center, following a similar slope except around the peak in BM velocity. Consistent with the phase of Z_{diff} remaining within $\pm\pi/2$ [Figure 3.2 (a)], the phase data in panel (e) mostly follows the phase of (b), indicating traveling wave propagation in both the BM and at the OSL edge (Stenfelt et al., 2003a).

At a relative distance of 0.03 in Figure 3.4 (d), the influence of Z_{diff} results in a nearly constant slope in the magnitude of the BM velocity with flexible OSL and CPB (solid black line) between 400 Hz and 1 kHz. The magnitudes are approximately 5 dB higher than those with rigid OSL and flexible CPB (dash-dotted black line) below 500 Hz, and similar above this frequency. Since Z_{diff} is similar for the two conditions with rigid OSL below 3 kHz [Figure 3.2 (a)], the 15 dB difference between the corresponding curves in Figure 3.4 (d) is consistent with (a) in this frequency range, reducing to less than 10 dB at higher frequencies. At a relative distance of 0.7 in Figure 3.4 (f), the curve characteristics remain consistent with those in Figure 3.4 (c).

Following the results for $v_{\mathrm{cp}}/p_{\mathrm{diff}}$ in Figure 3.4 (a)–(c), the curves in (d)–(f) indicate the presence of traveling wave in both the BM and OSL (Stenfelt et al., 2003a), highlighting that the impact of the OSL and CPB varies with frequency and distance along the CP.

Radial velocity profiles

The CP velocity results from Figure 3.4 at relative distances of 0.03 (left column), 0.3 (center column), and 0.7 (right column) from the base are extended in Figure 3.5, which shows radial profiles of the velocity for the condition with flexible OSL and CPB. The radial locations where the velocities were evaluated in Figure 3.4 are indicated by vertical black (BM center) and orange lines (OSL-CPB junction). The dotted lines depict the CPB-BM connection. Panels (a)–(c) show the magnitudes of v_{cp} normalized to the differential cochlear pressure p_{diff}, and panels (g)–(i) normalized to the maximum per frequency. Panels (d)–(f) and (k)–(l) illustrate these velocity profiles color-coded, respectively, with frequencies indicated along the y-axis.
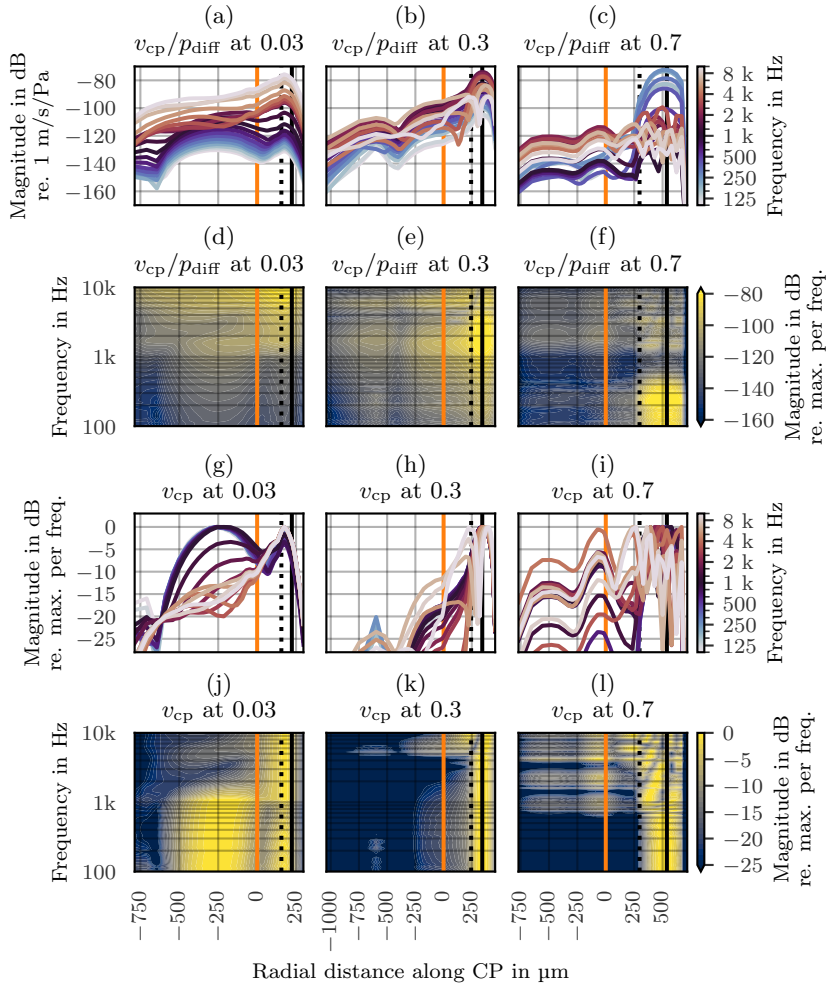
Figure 3.5: Profiles of CP velocity v_{cp} with flexible OSL and CPB along radial locations (x-axis), evaluated at relative longitudinal distances of 0.03 (left), 0.3 (center), and 0.7 (right). The vertical black solid lines indicate the BM center, and the orange lines indicate the OSL-CPB junction, corresponding to the radial positions in Figure 3.4. The dotted black lines indicate the CPB-BM connection. Panels (a)–(c) depict the magnitudes of v_{cp} normalized to the differential cochlear pressure p_{diff} from 100 Hz to 10 kHz (bright blue to bright red, with 1 kHz in black). Panels (d)–(f) display v_{cp}/p_{diff} in terms of the color-coded magnitude, with frequencies indicated on the y-axis. Panels (g)–(i) and (j)–(l) show the magnitudes of v_{cp} normalized to the maximum per frequency, following the same formats as panels (a)–(c) and (j)–(l), respectively.

Consistent with Figure 3.4, changes in magnitude with frequency are evident as horizontal variations at the radial BM center (solid black vertical line) for all three longitudinal positions in Figure 3.5 (a)–(c). At a relative distance of 0.03, the velocity magnitudes of the OSL, CPB and BM in (a) and (d) generally increase with frequency, however at different rates, leading to variations in velocity profiles with frequency. At higher frequencies [red shades in (a) and (g)], the simulation results show the maxima close to the CPB-BM junction. The velocity at the OSL-CPB junction (orange vertical line) stays 6–10 dB below the maximum in this frequency range. These results align with experimental observations by Raufer et al. (2019, Fig. 2), which were limited to frequencies of 784 Hz and above. Conversely, at lower frequencies [blue shades in (a) and (g)], the OSL portion of the CP exhibits bending with the maximum velocity occurring in the center of the OSL rather than near the CPB. These maxima reach the same velocity magnitudes as those at the BM. Indeed, the measured motions for some of the specimens reported in the supplementary material of Raufer et al. (2019, e.g., Fig. S3 B and F) show a similar characteristic at lower frequencies. The velocities normalized to the maximum per frequency in panels (g) and (j) indicate that the similarity in magnitude between the OSL and BM/CPB section persists up to about 1.5 kHz, coinciding with the characteristic change in Z_{diff} at this frequency [Figure 3.2 (a)]. Above this frequency, the maximum of the radial velocity distribution is reached at the BM-CPB junction.

The situation differs further from the cochlear base. Panels (k) and (l) indicate characteristic changes in the velocity profiles for relative distances of 0.3 and 0.7 between 6–7 kHz and 800–900 Hz, respectively, above the characteristic frequencies for these positions (cf. Figure 3.4). Below these frequencies, some degree of bending is still observed in the OSL at 0.3 relative distance in (h) and (k), particularly in its section close to the CPB, though the radial maximum velocity is reached at the BM. At 0.7 relative distance in (f), the maxima in OSL velocity are more than 25 dB lower than those at the BM. In Figure 3.4 (b) and (c), the decay of the BM traveling wave is visible above the characteristic frequencies, indicated by a sharp decrease in BM velocity with increasing frequency. This decay results in similar velocity magnitudes across the OSL, CPB, and BM, as shown in the upper parts of Figure 3.5 (k) and (l). At a relative distance of 0.7, this decay is further accompanied by a radial break-up of the BM/CPB section into a pattern with several maxima instead of a single one. Figure 3.5 (c) and (f) show that the decay also coincides with an increased motion across the OSL above approximately 1.5 kHz, as already observed at the OSL-CPB junction in Figure 3.4 (c) and (f).
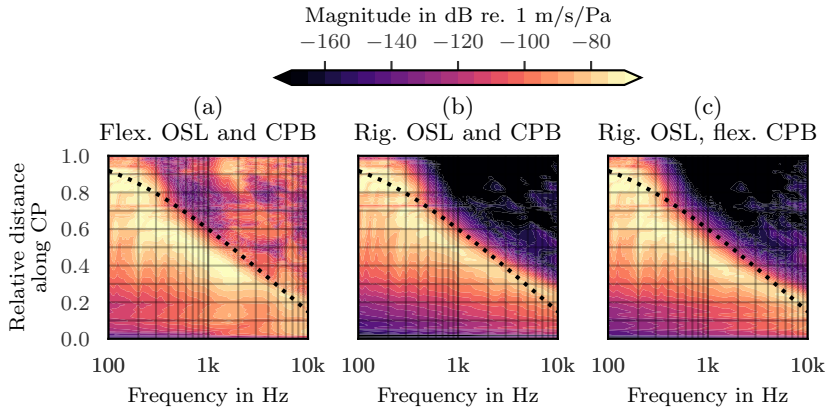
Magnitude in dB re. 1 m/s/Pa

−160 −140 −120 −100 −80

| (a) | (b) | (c) |
| Flex. OSL and CPB | Rig. OSL and CPB | Rig. OSL, flex. CPB |

Figure 3.6: Magnitude of CP velocity at the radial BM center normalized to differential cochlear pressure p_{diff} with flexible OSL and CPB (left), rigid OSL and CPB (center), and rigid OSL/flexible CPB over frequency (x-axes) and relative distance along the CP (y-axes). The tonotopic map after Greenwood (1990) is provided for reference (dashed line).

Longitudinal velocity distributions

The CP velocity results in Figure 3.4 and Figure 3.5 are restricted to specific relative distances of 0.03, 0.3 and 0.7 along the CP. To provide a more comprehensive view, Figure 3.6 presents the CP velocity at the radial BM center normalized to p_{diff} in terms of its color-coded magnitude across frequency (x-axes) and along the CP (y-axes) for the three conditions with flexible OSL and CPB (left), rigid OSL and CPB (center), and rigid OSL with flexible CPB (right). The results from Figure 3.4 (a)–(c) reappear in this representation as horizontal profiles at the corresponding frequencies. For additional context, the tonotopic map after Greenwood (1990) is included. The region left and below the Greenwood curve is characterized by BM traveling wave motion, which decays in the region above and to the right of the curve.

With rigid OSL in Figure 3.6 (b) and (c), the predominantly diagonal color gradient illustrates the increasing envelope of the BM traveling wave over frequency and distance, reaching a maximum before sharply decreasing. Dark colors in the upper right part of these panels signify the decay of the traveling wave, consistent with observations from Figure 3.4 under these conditions.

In contrast, Figure 3.6 (a) shows that the flexibility of the OSL results in a significant increase in BM motion in the upper right part of the plot, coinciding with the decay of the traveling wave, and also evident in Figure 3.4 (c) and (f).
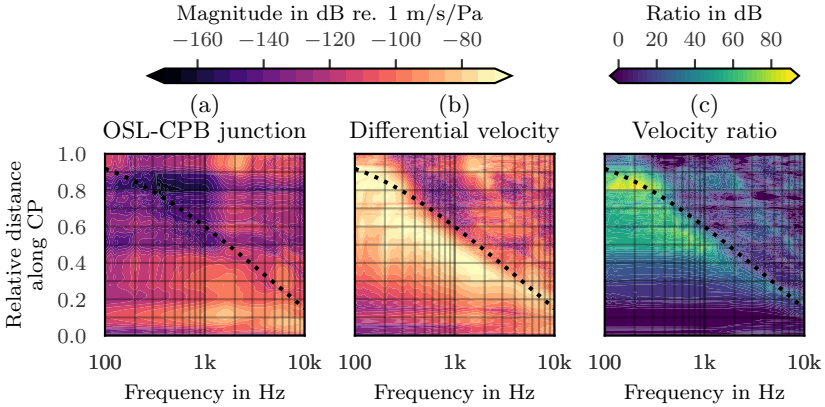
Figure 3.7: (a) CP velocity at the OSL-CPB junction and (b) differential velocity between BM center and OSL-CPB junction, both normalized to the differential pressure p_{diff} over frequency (x-axes) and relative longitudinal distance along the CP (y-axes). These results are given for the condition with flexible OSL and CPB. The color ranges correspond to those in Figure 3.6. In (c), the ratio of the velocity at the BM center to the velocity at the OSL-CPB junction is illustrated. The tonotopic map after Greenwood (1990) is provided for reference (dashed line).

Furthermore, comparing (a) with (b) and (c) reveals that the flexibility of the OSL generally leads to higher magnitudes for relative distances smaller than 0.3, while similar traveling wave magnitudes are reached at positions towards the apex. This trend aligns with differences observed in CP stiffness under the different scenarios, as shown in Figure 3.3 (black lines).

Instead of evaluating the velocity at the radial BM center, Figure 3.7 (a) depicts the longitudinal velocity distribution at the OSL-CPB junction in the same representation as Figure 3.6 for the condition with flexible OSL. Comparing Figure 3.7 (a) with Figure 3.6 (a), similarities are evident in the lower part of the panels for relative distances below approximately 0.3, which corresponds to similar stiffness in this CP region at these radial locations (Figure 3.3).

Figure 3.7 (b) displays the differential velocity between the BM center and the OSL-CPB junction, normalized to the differential pressure. Unlike (a), the diagonal color gradient around the characteristic frequencies indicates a traveling wave in the BM/CPB section of the CP that propagates along the OSL.

To compare BM and OSL velocities, Figure 3.7 (c) presents the magnitude of the ratio of the velocity at the BM center to the velocity at the OSL-CPB junction. Up to approximately 0.3 relative distance along the CP, the dark blue colors denote similar magnitudes in BM motion compared to CP motion at the

OSL-CPB junction, a phenomenon primarily dependent on position and largely independent of frequency within the traveling wave region. Towards the apex and below the characteristic frequencies, the velocity at the BM center associated with the traveling wave progressively surpasses that at the OSL-CPB junction by up to 90 dB at maximum, as depicted by the vertical shift towards yellow colors in Figure 3.7 (c). This difference again corresponds to the position-dependent difference in CP stiffness in Figure 3.3 (black solid vs. orange solid line).

3.4 Discussion

The numerical model of the inner ear should be regarded more as representative of an individual specimen rather than a predictive model for average data. Its primary objective is to qualitatively assess mechanisms associated with the flexibility of the CP and to highlight their fundamental implications. Consequently, the magnitudes of these mechanisms and related quantities, such as transition frequencies, will naturally vary among individual ears, as evidenced by the variability in experimental data (e.g., Aibara et al., 2001; Frear et al., 2018; Merchant et al., 1996; Nakajima et al., 2009; Puria, 2003; Puria et al., 1997; Raufer et al., 2019). Nevertheless, the simulations presented in this chapter have enabled the identification of distinct phenomena related to the flexibility of the CP in the inner ear's response to input at the OW. These phenomena contribute to the understanding of cochlear impedances, CP stiffness, and the longitudinal and radial distribution of CP motion.

3.4.1 Cochlear impedances

Differential impedance

In their study, Frear et al. (2018) utilized experimental intracochlear pressure data from multiple specimens to deduce a lumped element model of the differential impedances across the CP, Z_{diff}, incorporating a resistor representing "the wave impedance of the CP and surrounding fluid" (Frear et al., 2018) in parallel to an inductance representing the cochlear fluid at the apex. However, when considering typical material properties for the cochlear fluid (see Table 3.1), the resulting wave impedance $\rho c/A_{\text{ow}}$ would be approximately $470\,\text{GPa}\,\text{s/m}^3$ (equivalent to 233 dB in Figure 3.2), exceeding experimental maximum values (Lynch et al., 1982). Additionally, Raufer et al. (2019) showed that the CP at the base behaves spring-like, a behavior not incorporated in the lumped element model.

The simulations presented here help to reconcile these initially contradictory findings. The results depicted in Figure 3.2 confirm that the cochlear fluid predominantly influences Z_{diff} at the lowest frequencies. However, the OSL at

the cochlear base acts like a damped spring, shunting the inertial cochlear fluid above a resonance frequency, which is approximately 400 Hz in the model. At low and mid-frequencies, the OSL motion and the motion in the BM/CPB section are of similar magnitude [see Figure 3.5 (a)]. Due to its width being much larger than the widths of the CPB and BM in this region, the flexible OSL significantly contributes to the volume velocity flow between SV and ST (Raufer et al., 2019), causing a reduction of Z_{diff} compared to when considering the OSL as rigid. When the OSL contribution is missing, the fluid flow between SV and ST happens via the cochlear fluid moving along the CP, resulting in the inertial characteristic of Z_{diff} in these scenarios, reaching the magnitude of the fluid's wave impedance with rigid OSL and rigid CPB above 3 kHz.

Due to its impact on Z_{diff}, transitions observed in the radial motion profile of the OSL close to the base [Figure 3.5 (g)] result in a phase alternation of Z_{diff} around zero. Consequently, when averaged over individual curves (Frear et al., 2018), the characteristic of Z_{diff} becomes predominantly resistive. The contribution of the CPB to the volume velocity flow is minor, as indicated by the small differences between Z_{diff} with flexible and rigid CPB. Thus, it is mainly the motion of the OSL close to the base that is represented by the resistivity in the differential impedance.

Round window impedance

The simulation results concerning the RW impedance Z_{rw} in Figure 3.2 diverge above about 3 kHz between the conditions, even though Z_{rw} should, at first glance, remain unaffected by the CP motion. Upon examining the three-dimensional sound pressure data (not presented here), it became apparent that the OSL motion at the base and the modal break-up of the RW, as discussed by (Stenfelt et al., 2004b), result in a complex pressure distribution in the basal part of the ST, where p_{st} is assessed. Since Z_{rw} is determined based on this sound pressure at a specific location, these effects elucidate the influence of the OSL's flexibility on Z_{rw}. Similar effects have been observed in terms of an increased variability of p_{st} with frequency (Nakajima et al., 2009), and a phase divergence between individually determined RW impedances towards higher frequencies (Frear et al., 2018). Consequently, it appears that some of the observed variability is more attributable to the determination method of Z_{rw} rather than being an inherent property of the impedance itself.

Cochlear input impedance

The cochlear input impedance [Figure 3.2 (c)], which characterizes the load of the stapes at the OW, shows only a slight influence by Z_{rw}, but is mostly dominated

by Z_{diff}. Hence, the considerations regarding Z_{diff} are equally applicable to Z_{c}, suggesting a separation into different frequency ranges to be meaningful. Below about 400 Hz the primary load at the OW arises from the inertia of the cochlear fluid in SV and ST in conjunction with the compliance of the RW membrane. At higher frequencies, Z_{c} is predominated by the motion of the CP at the cochlear base, which exhibits resistive behavior on average.

Without considering the flexibility of the OSL and the CPB in cochlear models, the importance of the fluid may be overestimated, because it is not shunted by the moving OSL at the base. This omission could explain why the phase data of input impedances of cochlear models often indicates inertial effects, for example, in the models used in Gan et al. (2007) or Kim et al. (2014).

3.4.2 Cochlear partition stiffness

Békésy (1960) conducted measurements of the CP compliance at nine positions along the CP of a human inner ear, revealing a change by a factor of about 100 between the base and the apex. However, cochlear models typically require a stiffness change of approximately 10,000 to obtain a frequency map on the BM which covers the frequency range of hearing (Naidu and Mountain, 1998). Figure 3.3 provides an explanation which integrates both findings. With rigid OSL, the model reproduces the typical factor of more than four orders of magnitude between CP stiffness at the base and the apex. However, the simulations indicate that towards the base, CP stiffness is primarily influenced by the flexibility of the OSL, whereas towards the apex, it is influenced by the properties of the BM and CPB. Consequently, incorporating a flexible OSL led to variations in CP stiffness between the base and the apex, which align more closely with the experimentally determined values (Békésy, 1960; Olson et al., 2012).

The results demonstrate that the CPB consistently contributes to the stiffness of the CP across all positions along the CP. Given that the widths of the CPB and the BM are approximately equal (Raufer et al., 2020), the CPB's influence on CP stiffness is primarily due to effectively increasing the width of the flexible BM/CPB section by nearly a factor of two compared to the BM alone.

In essence, these findings suggest that CP stiffness measurements reflect the combined stiffness of the BM, CPB, and OSL, rather than solely that of the BM. Upon inspection of the BM and differential velocity, these effects do not contradict the formation of a traveling wave along the CP. However, it is important to note that these findings may not apply to mammals with stiff OSL and without CPB, such as gerbils (Naidu and Mountain, 1998; Raufer et al., 2019). In these cases, reported discrepancies can be attributed to the measurement procedure involving point loading rather than pressure loading (Kapuria et al., 2017). Here,

pressure loading was applied to determine CP stiffness, which more closely mimics the natural loading conditions of the cochlear fluid and better aligns with the experimental method used in the reference study of a human cochlea (Békésy, 1960; Olson et al., 2012).

3.4.3 Cochlear partition motion

Frequency dependence and traveling-wave characteristics

When normalized to the cochlear input, models typically predict a traveling wave behavior at fixed positions along the CP that is characterized by an increase in the magnitude of the BM velocity with a constant slope below the characteristic frequency, followed by a sharp decrease above it, and accompanied by a continuously decreasing phase (e.g., Kim et al., 2011; Ren et al., 2021; X. Wang et al., 2014; Zweig et al., 1976; Zwislocki, 1950). Similar curves were obtained with rigid OSL in Figure 3.4 (d)–(f).

However, experimental data from Gundersen et al. (1978) and Stenfelt et al. (2003a), measured at 12 mm from the cochlear base, diverge from these classical predictions by exhibiting a frequency range with constant magnitude before reaching a maximum. Remarkably, the simulations replicate this behavior when the OSL is modeled flexible [Figure 3.4 (e)]. A comparison between these velocity curves normalized to the cochlear input at the OW with those normalized to the differential cochlear pressure [Figure 3.4 (b)] and the differential impedance [Figure 3.2 (a)] reveals that this behavior arises from the interaction between the BM traveling-wave characteristics and the frequency-dependent properties of the differential impedance. Thus, these results highlight the need to consider differential impedance characteristics when analyzing BM motion as a transfer function relative to the input at the OW.

However, this differentiation is not commonly addressed in the literature, likely because classical models often assume there is no OSL motion, and studies on animals with stiff OSL have been widely used as experimental references (Raufer et al., 2019). While the present results with a rigid OSL are consistent with those predictions, the findings with a flexible OSL underscore the significant role of the OSL's flexibility. This flexibility influences the relation between the differential cochlear pressure and the OW input, coupled through a damped, spring-like motion of the OSL rather than the inertial behavior of the cochlear fluid above a certain frequency (approximately 400 Hz in the model), as captured by the differential impedance Z_{diff}.

Position dependence

In addition to the frequency dependence, the CP's flexibility influences BM velocity in a position-dependent manner. The differential velocity analysis along the CP [Figure 3.7 (b)] suggests that the flexibility of the OSL and the presence of the CPB only slightly affect frequency mapping characteristics. Nevertheless, the boundary condition at the OSL-CPB junction for the traveling wave in the BM/CPB section varies from base to apex. Up to a relative distance of about 0.3, the stiffness at the BM center reflects the combined mechanical characteristics of the OSL (Figure 3.3), resulting in OSL and BM motion of comparable magnitude in this region [Figure 3.7 (c)]. However, as the stiffness difference between the BM center and OSL-CPB junction increases towards the apex, the influence of the OSL's flexibility on the traveling wave characteristics diminishes.

Moreover, the velocity profiles in Figure 3.5 demonstrate significant variability in CP motion along the radial direction, where even small positional differences on the BM and CPB can lead to magnitude changes of 5–10 dB at the cochlear base Raufer et al. (cf. 2019, Fig. 2). These differences can become even more pronounced at positions closer to the apex [Figure 3.5 (g)–(i)].

Additional motion component

Beyond the BM traveling wave's decay, the flexibility of the OSL introduces an additional motion component into the BM and CPB. This is evident from increased BM velocities with a flexible OSL compared to a rigid OSL in Figure 3.4 (c) and (e) and in the upper right parts of Figure 3.6, as well as from similar radial magnitudes above the characteristic frequencies in Figure 3.5 (h) and (i). The decreasing phase at higher frequencies at the OSL-CPB junction for relative distances of 0.3 and 0.7 [Figure 3.4 (b) and (c)], suggests that this additional motion component involves traveling-wave propagation in the OSL (Stenfelt et al., 2003a). However, due to the OSL's layered structure and its decrease in width from base to apex (Raufer et al., 2020), the OSL traveling wave is less distinctly characterized than the BM traveling wave, which shows more clearly defined magnitude and phase patterns [Zweig et al. (1976); see Figure 3.6 (a) versus Figure 3.7 (a)]. Notable examples illustrating this complexity are the velocity increase across the OSL between 1–2 kHz at 0.7 relative distance [Figure 3.5 (f)], and its lever-like motion in response to a uniform load leading to non-meaningful stiffness values (Section 3.3.2). Thus, regarding the additional component of BM motion induced by the OSL, it may be more useful to conceptualize the OSL motion as a complex, frequency-dependent bending pattern in both radial (Figure 3.5) and longitudinal directions [Figure 3.7 (a)], which is coupled to the BM motion through the CPB and via the cochlear fluid. Toward

the apex, this motion component is further complicated by a radial break-up of the BM motion [Figure 3.5 (i) and (l)], which accounts for phase differences between the BM center and the OSL edge [Figure 3.4 (c)].

Role of the cochlear partition bridge

The flexibilities of both the OSL and the CPB contribute to an increase in phase lag in BM velocity, consistent with predictions by Taber and Steele (1981). However, the CPB's flexibility only contributes in terms of a slight increase in the magnitude of the BM motion compared to the OSL's flexibility, as indicated by the high similarity between BM velocity distributions with a rigid OSL [Figure 3.6 (b) and (c)]. Additionally, the radial velocity profiles underscore the CPB's role as a flexible connection between the OSL and BM (Raufer et al., 2019), an effect which varies little from base to apex.

Implications for interpreting cochlear partition motion

Further experimental data on CP motion is needed to improve its understanding, as the present findings, in line with Raufer et al. (2019), partially diverge from the classical view on inner ear mechanics. The results highlight the importance of considering the flexibility of the CP, particularly of the OSL, when interpreting CP velocity data, because this flexibility influences the differential pressure driving the traveling wave, alters the combined mechanical characteristics of the entire CP, and introduces additional BM motion through the OSL.

Furthermore, it is important to not interpret the simulated CP velocities and the reference data measured from temporal bone specimens (Gundersen et al., 1978; Raufer et al., 2019; Stenfelt et al., 2003a) as equivalent to the input converted by inner hair cells into neural signals. While these investigations focussed on macro mechanics and linear passive mechanisms, in living ears, auditory nerve fibers show frequency tuning and active nonlinear mechanisms lead to an amplitude gain at the characteristic locations (Robles and Ruggero, 2001). These processes lead to a sharper tuning of auditory nerve responses compared to the BM velocity observed in passive models and dead specimens, where such active processes are absent. Notably, both the amplification by outer hair cells and the nerve response initiated by inner hair cells depend on the relative motion between the tectorial membrane and the hair cell stereocilia, which can be affected by the motion of the OSL and CPB (Raufer et al., 2019). At present, it remains unclear how the flexibility of the OSL influences both the transformation of BM motion into hair bundle displacement and the mechanisms behind cochlear amplification, particularly in terms of the level-dependent dynamics in BM versus OSL motion.

Moreover, when the sound pressure in the ear canal is used as a reference, rather than the OW volume velocity [Figure 3.4 (d)–(f)] or stapes velocity (Stenfelt et al., 2003a), the ME transfer function introduces an additional frequency dependence, typically with a band-pass characteristic centered around 1 kHz (Koch et al., 2022). This frequency dependence would need to be added up to the characteristics observed in the CP motion in Figure 3.4 (d)–(f).

3.4.4 Limitations and suggestions for future work

The material parameters utilized for the FE simulations were derived from experimental sources and other models to the extent possible (see Table 3.1). In cases where no references were available, reasonable values were assumed, leading to generally satisfactory agreements with experimental data in Section 3.3. A detailed parameter sensitivity analysis has not been conducted for the sake of brevity. Instead, focusing the simulations on a specific set of material parameters while varying between rigid and flexible OSL and CPB conditions helped to identify the mechanisms by which CP motion influences cochlear macromechanics for stimulation via the OW. This understanding provides a basis for estimating the impact of influencing factors. For example, inter- or intraindividual variations in the Young's moduli of the VP and TP are expected to affect OSL stiffness (Figure 3.3), with a proportional relationship at maximum, as approximated using the theory for sandwich structures (Zenkert, 1995). Such variations result in shifts in the resonances of the differential impedance [Figure 3.2 (a)], which scale with the square root of the stiffness. These resonance shifts, in turn, affect the characteristics of CP motion when normalized to the OW input [Figure 3.4 (d)–(f)].

In this chapter, the flexible OSL and the two windows were the only structures allowing fluid flow, while all other boundaries were considered rigid. However, it is important to note that fluid flow effects associated with small channels and other compliant structures in the inner ear have been demonstrated, e.g., in terms of leakage impedances (Frear et al., 2018). Similarly, the medial side of the OSL has been assigned with a fixed boundary condition within the model. Given that the modiolus consists of spongy bone encompassing the cochlear nerve and spiral ganglion, and that thin walls between different cochlear turns have been revealed by MicroCT scans (Bom Braga et al., 2023), additional flexibility and losses may be present through these boundaries in real ears. With an improved understanding of the role of the thin OSL structure achieved through this work, these structures could be explored in future investigations.

Furthermore, future models could integrate both linear/passive and nonlinear/active approaches (cf. mouse cochlea model by Motallebzadeh et al. (2018),

Motallebzadeh and Puria (2021)) while incorporating the OSL as a flexible structure. In such models, it would be reasonable to distinguish between the structural damping and the viscous damping in the fluid, which were both captured by effective loss factors in the model. These studies could also enhance our understanding of the experimental variation related to these mechanisms, particularly in the cochlear impedances, by accounting for variations in inner ear shapes.

3.5 Summary

In this chapter, a FE model of the human inner ear was used to investigate how the flexibility of the CP, specifically the OSL and CPB, influences the inner ear's response to OW input by modeling these structures as either rigid or flexible. The results underscore that the motion of the OSL close to the base plays a crucial role in the resistive behavior observed in both the differential impedance across the CP and the related cochlear input impedance. This, in turn, impacts the differential intracochlear sound pressure, which initiates a traveling wave propagation in the BM/CPB section along the flexible OSL. Above characteristic frequencies, an additional motion component enters the BM and CPB via the OSL. Radial velocity profiles highlighted frequency-dependent bending characteristics of the OSL towards the base, resulting in comparable magnitudes of BM and OSL motion at lower frequencies. Towards higher frequencies and closer to the apex, maximum magnitudes are reached in the BM/CPB section, aligning well with experimental measurements. Furthermore, the flexibility of the OSL was found to dominate the CP stiffness at the base relative to the stiffness of the BM itself, potentially elucidating discrepancies between model predictions and experimental data. The CPB consistently contributes to stiffness and motion along the CP's length, effectively increasing the width of the flexible BM/CPB section compared to when considering the BM only.

In essence, the findings of this chapter suggest that the flexibility of the OSL and the presence of the CPB significantly influence cochlear macro mechanisms. They emphasize the need for caution when interpreting CP motion based on classical models with rigid OSL and without CPB, highlighting the complexity introduced by these structures and the importance of additional experimental validation. These insights are important for understanding the response of the inner ear to AC stimulation and the BC pathways via the OW.

4

Contribution of the osseous spiral lamina to bone conduction hearing

4.1 Introduction

The preceding Chapter 3 investigates the inner ear's response to input at the OW, with particular emphasis on the role of the CP's flexibility. However, in BC hearing, the inner ear is also stimulated via vibration of its surrounding structures (Stenfelt and Goode, 2005a; Tonndorf, 1966, 1968). This vibrational input induces two effects: inertial forces within the cochlear fluid due to the rigid body motion component of the vibration and pressure responses resulting from a deformation component (Dobrev et al., 2025, 2023; Stenfelt, 2015; Tonndorf, 1962). Both mechanisms are influenced by the impedances of the two windows and the CP (Tonndorf, 1966). Additionally, "third-window" mechanisms have been proposed in BC hearing, based on experimentally observed inequalities in fluid flow between the OW and RW (Stenfelt et al., 2004a) and sound pressure transmission from the skull interior (Dobrev et al., 2022; Freeman et al., 2000; Sohmer and Freeman, 2004).

Cadaver head measurements and numerical simulations indicate that the inner ear predominantly undergoes rigid body motion up to approximately 7–10 kHz (Dobrev et al., 2025, 2023). This finding aligns with the notion that, in this frequency range, structural wavelengths in the surrounding bone are significantly larger than the inner ear's dimensions. Such motion is closely linked to cochlear fluid inertia effects, which have been predicted as the most important mechanism driving the inner ear's response during BC (Stenfelt, 2016, 2020; Taschke, 2005).

Building on the analysis of CP flexibility in Chapter 3, this chapter incorporates the effects of rigid body motion as a BC stimulation mechanism. This stimulation is applied in a direction perpendicular to the OW, with the ME accounted for solely as a passive load and no sound entering through the OW. By separately analyzing OW input and rigid body stimulation, this chapter aims to provide a more comprehensive understanding of the mechanisms influencing inner ear fluid dynamics during BC, focusing on volume velocity responses at the OW and RW (Stenfelt et al., 2004a) and intracochlear sound pressures (Stieger et al., 2018).

Consistent with Chapter 3, the role of the CP is examined by modeling the CPB and OSL in the FE model either as flexible or rigid, using the same geometry (Figure 3.1) and material properties (Table 3.1). In contrast to Chapter 3, varying the flexibility of the CPB had no significant impact on the volume velocities and sound pressures when the OSL was modeled as rigid. Therefore, this chapter focuses on results related to the OSL, with the CPB kept flexible throughout.

4.2 Methods

For a detailed description of the FE model of the human inner ear, refer to Section 3.2.1. The following sections outline the modifications made to the simulation setup compared to Chapter 3.

4.2.1 Oval window input

To relate the BC contributions entering the inner ear via the OW to the vibration of the cochlear bone, the approach of Stenfelt (2016, 2020) is adopted. This approach utilized a measured differential velocity between the stapes footplate and the adjacent bone, normalized to the velocity of the bone:

$$\gamma_{\mathrm{ow}} = \frac{v_{\mathrm{stap}} - v_{\mathrm{prom}}}{v_{\mathrm{prom}}} = \frac{v_{\mathrm{stap}}}{v_{\mathrm{prom}}} - 1, \tag{4.1}$$

where v_{stap} is the velocity of the stapes footplate, and v_{prom} is the velocity of the cochlear promontory, both measured in the same direction (Stenfelt et al., 2002). In Stenfelt (2016, 2020), γ_{ow} was multiplied by the area of the stapes footplate to define the OW volume velocity as an input to a lumped element model of the inner ear, characterizing the BC sound that enters the inner ear via the ME. For this work, γ_{ow} was directly applied as the input velocity at the OW, accounting for these BC contributors while the surroundings remained fixed. To obtain γ_{ow}, 1 was subtracted from the complex-valued average data for $v_{\mathrm{stap}}/v_{\mathrm{prom}}$ measured

across 26 temporal bone specimens with intact MEs reported in Stenfelt et al. (2002, Fig. 3a).

In experimental setups, separating BC sound entering via the OW from the response to inner ear motion is not feasible. Using the measured differential velocity to predict the response to BC contributors entering via the OW, as similarly done by Stenfelt (2016), implicitly assumes that these contributors were the dominant source of differential stapes motion compared to internal sound pressure acting on the stapes footplate in the average experimental data (Stenfelt et al., 2002).

For implementation, rather than directly applying γ_{ow} as velocity boundary condition at the OW, the linearity of the model was leveraged. This linearity allows scaling the simulation results obtained with a unit inward velocity of $1\,\mathrm{m/s}$ by γ_{ow} during post-processing, remaining with the identical OW boundary condition in the FE simulations as in Chapter 3.

4.2.2 Rigid body stimulation

As a second stimulation condition, rigid body motion was applied as a unit velocity of $1\,\mathrm{m/s}$ to the structures surrounding the inner ear (Kim et al., 2011, 2014). This approach captures the fluid inertia BC mechanism and the pressure release at the two windows (Tonndorf, 1968), while excluding the effects of cochlear bone deformation (see Section 4.4 for potential impacts on the results). Experimental studies (Zhao et al., 2021) and numerical simulations (Kim et al., 2014) have demonstrated the directional sensitivity of the inner ear to BC stimulation. To align with the experimental reference (Stenfelt et al., 2004a), the translation direction was set perpendicular to the OW, corresponding to the primary direction of stapes motion under AC stimulation. In a subset of the simulations, the OSL was modeled as rigid by also applying rigid body motion to this structure. By normalizing the amplitude of the stimulation velocity vector to unity, the results for OW input and rigid body stimulation could be directly compared, as both were referenced to the same quantity.

During the rigid body stimulation, a lumped model of the reverse ME impedance $Z_{\mathrm{me'}}$ was applied at the OW, derived from experimental data during RW stimulation by dividing SV pressure through OW volume velocity (Frear et al., 2018). $Z_{\mathrm{me'}}$ was modeled as a series resonator with parameters $R_{\mathrm{me'}} = 4.76 \times 10^{10}\,\mathrm{Pas/m^3}$, $L_{\mathrm{me'}} = 7.78 \times 10^5\,\mathrm{Pas^2/m^3}$, and $C_{\mathrm{me'}} = 2.56 \times 10^{-15}\,\mathrm{Pa/m^3}$ (Frear et al., 2018). In the FE model, the impedance boundary condition at the OW was implemented as a velocity condition:

$$v_{\mathrm{ow}}(\mathbf{x}) = -\left[\frac{\langle p \rangle_{\mathrm{ow}}}{Z_{\mathrm{me'}} \times A_{\mathrm{ow}}} + \mathbf{v}_{\mathrm{bc}} \cdot \mathbf{n}(\mathbf{x}) \right], \tag{4.2}$$

where $v_{\mathrm{ow}}(\mathbf{x})$ represents the inward acoustic particle velocity at positions $\mathbf{x}$ on the OW surface, and $\langle p\rangle_{\mathrm{ow}}$ the surface-averaged sound pressure at the OW (equal to the force acting on the stapes footplate divided by the OW area, A_{ow}). The dot product $\mathbf{v}_{\mathrm{bc}} \cdot \mathbf{n}(\mathbf{x})$ captures the local normal component of the stimulation velocity vector $\mathbf{v}_{\mathrm{bc}}$, calculated using the unit vector $\mathbf{n}(\mathbf{x})$ perpendicular to the surface in outward direction from the fluid.

This boundary condition resembles the boundary condition already introduced in Chapter 2 for impedances at the EC, applied here to the OW to represent the load on the cochlear fluid. To illustrate Equation 4.2, consider a scenario where the inner ear's surroundings are fixed in position (i.e., $\mathbf{v}_{\mathrm{bc}} = \mathbf{0}$). In this case, Equation 4.2 reduces to the classical impedance equation for $Z_{\mathrm{me}'}$, consistent with its measurement during RW stimulation (Frear et al., 2018) and its use in previous BC studies (Guan et al., 2020; Ren et al., 2021; Stenfelt, 2015, 2016). However, during BC stimulation, the temporal bone structures adjacent to the OW are in motion, necessitating the inclusion of this velocity in the impedance boundary condition (cf. Chapter 2). This is highlighted, for example, at a frequency where $Z_{\mathrm{me}'}$ is acoustically rigid. In this case, Equation 4.2 simplifies to $v_{\mathrm{ow}}(\mathbf{x}) \approx -\mathbf{v}_{\mathrm{bc}} \cdot \mathbf{n}(\mathbf{x})$, indicating that the stapes footplate moves with the adjacent bone (the negative sign reflects inward versus outward velocity definitions). Omitting $\mathbf{v}_{\mathrm{bc}}$ would incorrectly imply that $v_{\mathrm{ow}}(\mathbf{x}) = 0$, suggesting that the OW surface remains fixed in position despite the motion of the inner ear.

Thus, this OW boundary condition conceptually incorporates the ME as part of the moving system, preserving the acoustic reaction to lymph pressure at the OW while excluding BC contributors entering the inner ear via the OW.

4.2.3 Volume velocities

Two types of volume velocities were evaluated, illustrated in Figure 4.1. *Total volume velocities* q_{ow}, q_{rw}, q_{vp} and q_{tp} were calculated by integrating the normal component of the acoustic particle velocity vector $\mathbf{v}$ over the surfaces in contact with the fluid:

$$q_k = \iint_{S_k} \mathbf{v}(\mathbf{x}) \cdot \mathbf{n}(\mathbf{x})\, \mathrm{d}S, \quad k \in \{\mathrm{rw, ow, vp, tp}\}. \tag{4.3}$$

Here, S_k represents the surface, and $\mathbf{v}(\mathbf{x}) \cdot \mathbf{n}(\mathbf{x})$ is the normal component of the acoustic particle velocity in outward direction of the fluid at a position $\mathbf{x}$ on the surface. *Differential volume velocities* $q_{\mathrm{ow,diff}}$, $q_{\mathrm{rw,diff}}$, $q_{\mathrm{vp,diff}}$ and $q_{\mathrm{tp,diff}}$ were determined by integrating the normal component of the differential velocity

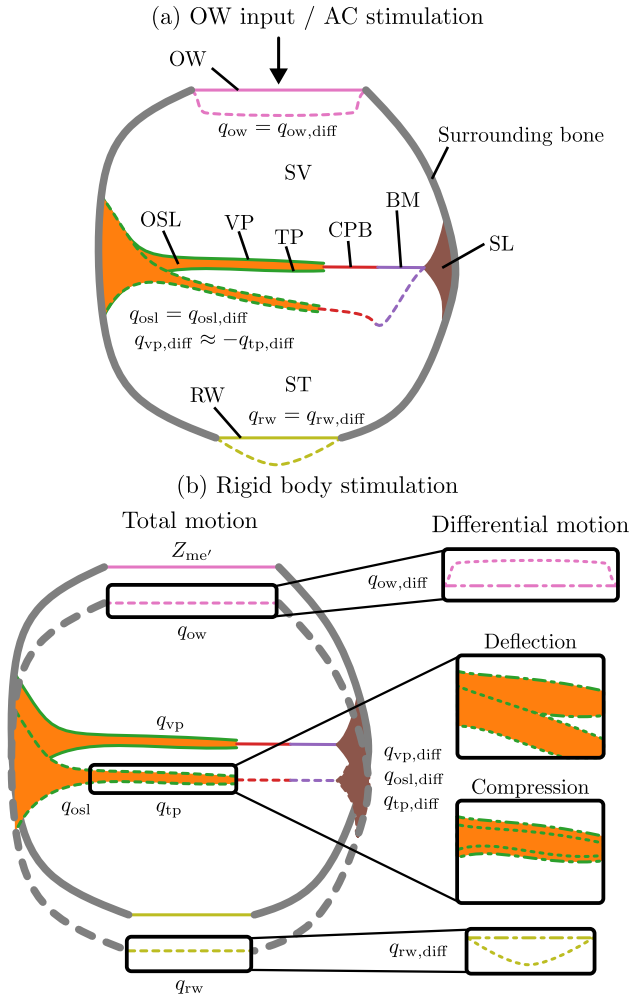(a) OW input / AC stimulation

(b) Rigid body stimulation

Figure 4.1: Schematic cross-sectional illustration of the motion types of the OW, RW, and OSL for (a) OW input and (b) rigid body stimulation. For rigid body stimulation, the total motion (long dashed lines) is described by the total volume velocities q_{ow}, q_{rw}, q_{vp} and q_{tp}, while the differential motion components (short dashed lines) are defined relative to the translational motion (dash-dotted lines) and quantified by $q_{\text{ow,diff}}$, $q_{\text{rw,diff}}$, $q_{\text{vp,diff}}$, and $q_{\text{tp,diff}}$. OSL volume velocities are calculated as $q_{\text{osl}} = q_{\text{vp}} + q_{\text{tp}}$ and $q_{\text{osl,diff}} = q_{\text{vp,diff}} + q_{\text{tp,diff}}$. For the OSL, the two distinct types comprising the differential motion are shown: deflection, which arises from the pressure difference between the VP and TP, and compression, which results from common pressure in SV and ST. For OW input, total and differential motion are identical.

between the acoustic particle velocity $\mathbf{v}$ and the stimulation velocity $\mathbf{v}_{\mathrm{bc}}$:

$$q_{k,\mathrm{diff}} = \iint_{S_k} [\mathbf{v}(\mathbf{x}) - \mathbf{v}_{\mathrm{bc}}] \cdot \mathbf{n}(\mathbf{x})\,\mathrm{d}S, \quad k \in \{\mathrm{rw}, \mathrm{ow}, \mathrm{vp}, \mathrm{tp}\}. \qquad (4.4)$$

This calculation method for differential volume velocities is comparable to the experimental approach of Stenfelt et al. (2004a) for the OW and RW, though here the integrations were performed numerically.

While the OW and RW differential volume velocities allow for comparison with AC stimulation (Stenfelt et al., 2004a), the total volume velocities quantify the overall motion of surfaces.[1] Since the OSL surface in contact with the fluid comprises the VP and TP, the OSL volume velocities are calculated as $q_{\mathrm{osl}} = q_{\mathrm{vp}} + q_{\mathrm{tp}}$ and $q_{\mathrm{osl,diff}} = q_{\mathrm{vp,diff}} + q_{\mathrm{tp,diff}}$. It is important to note that, because the unit vector $\mathbf{n}(\mathbf{x})$ points outward from the inner ear, a zero-phase condition of the volume velocities defined in Equation 4.3 and Equation 4.4 corresponds to fluid flow in the outward direction.

To illustrate, consider AC stimulation where $\mathbf{v}_{\mathrm{bc}} = \mathbf{0}$. In this case, total and differential volume velocities are identical, as surface deformation is solely due to fluid pressure loading on the boundaries or, at the OW, due to the stimulation condition itself [Figure 4.1 (a)]. For rigid body stimulation applied to the inner ear's surroundings, the total motion of fluid surfaces coupled to structures not directly assigned the stimulation velocity – namely, the OW, RW, CP, and SL – includes both translation induced by the stimulation and deformation caused by sound pressure loading [Figure 4.1 (b)]. In this case, the differential volume velocities are solely governed by the sound pressure acting on the surfaces and represent the deformation relative to the translational motion. In addition, since the cochlear fluid is nearly incompressible, mass conservation ensures that the sum of the differential volume velocities across all cochlear boundaries equals zero.

The RW and OSL responses to sound pressure are implicitly handled by the fluid-structure interaction in the model, consistent with real ears. For the OW, using $v_{\mathrm{ow}}(\mathbf{x}) = -\mathbf{v}(\mathbf{x}) \cdot \mathbf{n}(\mathbf{x})$ and substituting Equation 4.2 into Equation 4.4 yields:

$$q_{\mathrm{ow,diff}} = \frac{\langle p \rangle_{\mathrm{ow}}}{Z_{\mathrm{me}'}}, \qquad (4.5)$$

---

[1]Analogous to Chapter 2, *structural volume velocities* can be defined as

$$q_{k,\mathrm{s}} = \iint_{S_k} \mathbf{v}_{\mathrm{bc}} \cdot \mathbf{n}(\mathbf{x})\,\mathrm{d}S,$$

such that $q_k = q_{k,\mathrm{diff}} + q_{k,\mathrm{s}}$, with $k \in \{\mathrm{rw}, \mathrm{ow}, \mathrm{vp}, \mathrm{tp}\}$. For this chapter, however, it is sufficient to limit the analyses to the total and differential volume velocities.

demonstrating that $q_{\text{ow,diff}}$ results of the sound pressure acting on the reverse ME impedance.

As illustrated in Figure 4.1, the differential motion of the OSL comprises two distinct types: deflection and compression. Deflection arises from the pressure difference between the SV and ST or from inertial effects of the OSL, while compression is driven by the common pressure within the SV and ST. For OW input, deflection is expected to dominate, resulting in $q_{\text{vp,diff}} \approx -q_{\text{tp,diff}}$. Conversely, when compression is the primary mode of motion, $q_{\text{vp,diff}} \approx q_{\text{tp,diff}}$. These effects will be further discussed based on the simulation results.

4.2.4 Intracochlear sound pressure

Consistent with Chapter 3, intracochlear sound pressures in the SV and ST were assessed using virtual sound probes within the fluid domains. This method follows experimental setups from prior studies (Borgers et al., 2019; Dobrev et al., 2022; Frear et al., 2018; Nakajima et al., 2009; Olson, 1998; Stieger et al., 2018). Additionally, following Equation 4.5, the average sound pressure over the OW surface, $\langle p \rangle_{\text{ow}}$, was evaluated.

4.2.5 Simulation parameters and post-processing

The simulations were conducted using Comsol Multiphysics® version 6.2, covering frequencies from 100 Hz to 10 kHz with a resolution of 12 frequencies per octave. The meshing parameters were kept as in Chapter 3.

The volume velocities and sound pressures were exported in .csv format and analyzed using custom Python scripts. The updated version of the FE model including the rigid body stimulation, the simulation results, and Python code used for the analysis are provided at `https://doi.org/10.5281/zenodo.14850065`.

4.3 Results

The results are structured to systematically investigate the influence of the OSL's flexibility on inner ear fluid dynamics. First, total and differential volume velocities at the OW, RW, and OSL are presented for both stimulation conditions to characterize the types of motion occurring at these boundaries. The differential volume velocity associated with the SL was found to be negligible compared to these boundaries, indicating that it behaves as a rigid structure and is therefore not discussed further. Comparisons of OW and RW differential volume velocities are made with experimental data from Stenfelt et al. (2004a). Next, the individual contributions of the OSL (divided into VP and TP) and OW to the RW differential volume velocity are analyzed in more detail. Since the

differential volume velocities are driven by sound pressure loading, intracochlear sound pressures are subsequently examined. These include probe evaluations compared to experimental data from Stieger et al. (2018) as well as visualizations of three-dimensional sound pressure distributions.

4.3.1 Volume velocities

Figure 4.2 presents the total and differential volume velocities for (a) the RW, (b) the OW, (c) the VP, and (d) the TP. Black and green lines represent differential and total volume velocities, respectively, under rigid body stimulation, while orange lines correspond to BC input at the OW. As detailed in Section 4.2.3, the total and differential volume velocities are identical for the OW input condition. The differential volume velocity magnitudes at the OW and RW are compared against experimental data obtained by Stenfelt et al. (2004a) from measurements on eight temporal bones. These experimental results were converted from volume displacements to volume velocities. In these measurements, the ME structures were removed, leaving only the stapes footplate and annular ligament at the OW. The BC stimulation directions were perpendicular to the stapes footplate, consistent with the rigid body stimulation direction applied in the model. The experimental data is shown as the mean ± standard deviation. According to an error analysis in Stenfelt et al. (2004a), these results are considered valid above approximately 300 Hz, as indicated by the vertical dotted lines.

General observations

The magnitudes of the differential volume velocities under rigid body stimulation with a flexible OSL (solid black lines) exhibit similar trends for the surfaces in Figure 4.2 (a)–(d). These curves increase with a slope of approximately 40 dB per decade up to about 1 kHz, followed by alternating behavior around constant values above 2 kHz. For the OW, VP, and TP [Figure 4.2 (b)–(d)], the total volume velocity magnitudes under rigid body stimulation (green lines) remain nearly constant with frequency and are similar for both the flexible and rigid OSL conditions. The differential volume velocity magnitudes in these cases are at least 10–20 dB lower than the total volume velocities, indicating that surface deformation due to sound pressure loading is minor compared to the rigid body motion along with the inner ear surroundings. The phases of the total velocities at either zero or $\pm\pi$ indicate whether the spatial angle between the stimulation and the average surface normals in outward direction from the fluid is within 90° or exceeds this range.
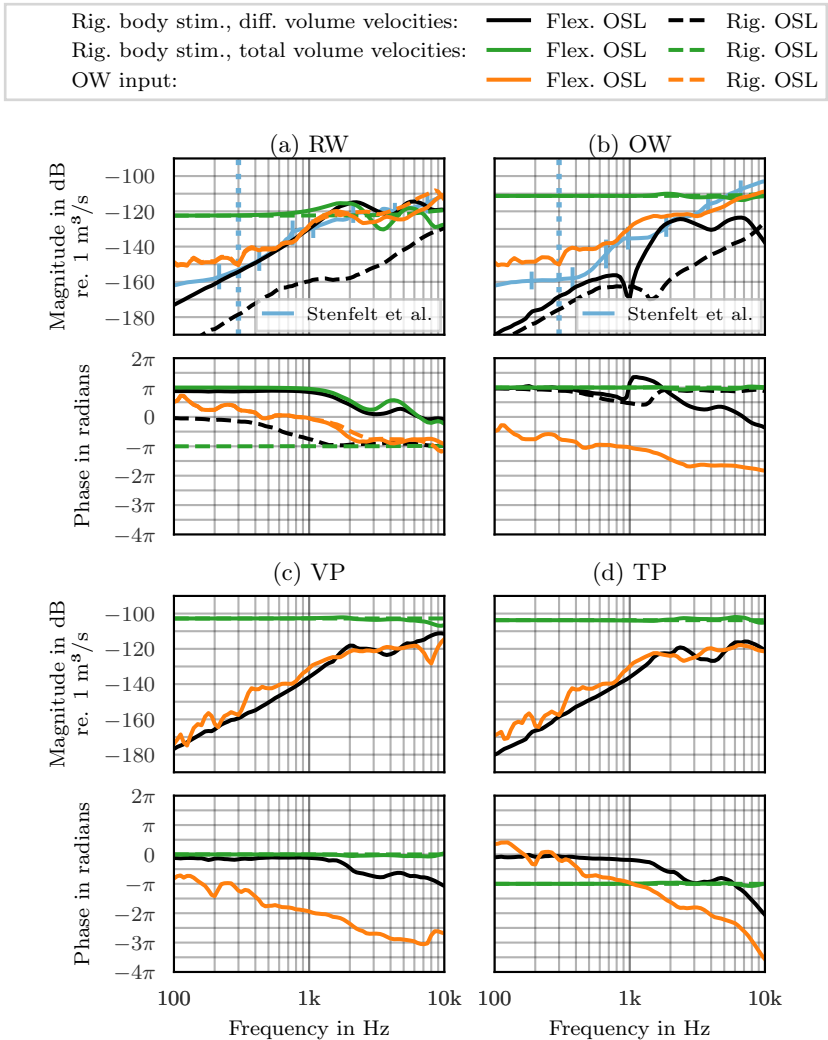
Figure 4.2: Magnitude and phase of the volume velocities associated with the (a) RW, (b) OW, (c) VP, and (d) TP. Black lines indicate differential and green lines total volume velocities with rigid body stimulation. Orange lines represent the volume velocities for BC input at the OW, where total and differential volume velocities are identical. Solid lines represent results with flexible OSL, and dashed lines with rigid OSL. The OW and RW differential volume velocity magnitudes are compared to the experimental data from Stenfelt et al. (2004a) (blue, mean and standard deviation), which were recalculated to volume velocities instead of volume displacements. The vertical dotted lines indicate the lower frequency limit (300 Hz) for the validity of the experimental data.

Round window volume velocities

A significant impact of the OSL's flexibility is visible for the RW volume velocities in Figure 4.2 (a). The differential and total volume velocities under rigid body stimulation with flexible OSL (solid black and green lines) show similar magnitudes above approximately 1 kHz, indicating comparable contributions of rigid body motion and deformation due to sound pressure loading on the RW in this frequency range. The RW differential volume velocities under both rigid body stimulation and OW input (solid black and orange lines) align with the experimental data from Stenfelt et al. (2004a) within the standard deviation.

In contrast, under rigid body stimulation with a rigid OSL (dashed black line), the RW differential volume velocities are 30–40 dB lower than those for the flexible OSL up to 2 kHz. Above this frequency, the difference between the conditions reduces to 10 dB towards 10 kHz due to a continuous increase for the rigid OSL condition. Additionally, except between approximately 500 Hz and 2 kHz the differential velocity results with flexible versus rigid OSL show phase differences close to π, indicating opposite directions of RW motion relative to the rigid body stimulation. As a result, the total velocity curves with flexible OSL alternate with frequency in a range of ± 10 dB around the constant value of the rigid OSL condition above 1 kHz.

For OW input (orange lines), RW volume velocities match the experimental magnitudes above approximately 400 Hz, and the differential volume velocities for rigid body stimulation and flexible OSL above 500 Hz. The impact of OSL flexibility is limited to a reduction of approximately 5 dB in magnitude above 2 kHz.

Differential volume velocity at the oval window

The OW differential volume velocity under rigid body stimulation (solid black line) exhibits a distinct notch near 1 kHz [Figure 4.2 (b)]. This minimum corresponds to a minimum in the sound pressure distribution, as further inspected in Section 4.3.3. Similarly, the rigid OSL condition (dashed black line) shows a notch at approximately 1.5 kHz.

The flexible OSL condition exhibits higher magnitudes between 1 kHz and 8 kHz, with a maximum difference of approximately 35 dB around 2 kHz. Below 800 Hz, both conditions show similar phase and increase with a 40 dB per decade slope, though the magnitudes with flexible OSL are about 5 dB higher.

The experimental data (blue lines) aligns with the simulation results for a flexible OSL within standard deviation between approximately 300–500 Hz and 1.5–3 kHz. Above 3 kHz, the simulation results are 10–35 dB lower than the

experimental data. For the rigid OSL condition (dashed black line), the difference from the experimental values is at least 20 dB above 1 kHz.

Since the OW volume velocity is the input for the corresponding OW stimulation condition (orange), the OW differential volume velocities are equal for the two OSL conditions. These results align with the experimental data above approximately 500 Hz.

Volume velocities at the vestibular and tympanic plates

The VP and TP volume velocities [Figure 4.2 (c)–(d)] show that the deformation of these structures is small compared to their overall motion for both the BC input at the OW (orange) and the rigid body stimulation (black). The phase difference of π between the VP and TP total volume velocities (green) reflects their opposing positions on the OSL, though both move in the same direction [see Figure 4.1].

4.3.2 Differential volume velocities referenced to the round window

From Figure 4.2 it is difficult to directly relate the differential volume velocities to each other. Since the RW impedance is significantly lower than the reverse ME impedance at the OW (Frear et al., 2018), differential fluid flow from both the OW and within the inner ear is predominantly directed toward the RW (Stenfelt et al., 2004a). To facilitate comparison, Figure 4.3 presents the differential volume velocities normalized to the RW differential volume velocity for (a) OW input and (b) rigid body stimulation. Solid lines indicate the ratios $q_{\mathrm{ow,diff}}/q_{\mathrm{rw,diff}}$ (black), $q_{\mathrm{osl,diff}}/q_{\mathrm{rw,diff}}$ (orange), $q_{\mathrm{vp,diff}}/q_{\mathrm{rw,diff}}$ (green), and $q_{\mathrm{tp,diff}}/q_{\mathrm{rw,diff}}$ (red) for a flexible OSL. The dashed black lines represent $q_{\mathrm{ow,diff}}/q_{\mathrm{rw,diff}}$ with a rigid OSL, while all other ratios are zero ($-\infty$ dB) for this condition. By normalizing to the RW outlet, the OW results can directly be compared to experimental data from Stenfelt et al. (2004a, Fig. 6 and 10). The experimental magnitudes, corresponding to AC and BC stimulation in the original study, are shown in blue, including both mean curves and individual data.

Oval window input

For BC input at the OW [Figure 4.3 (a)], the magnitude of $q_{\mathrm{ow,diff}}/q_{\mathrm{rw,diff}}$ (black lines) remains within 3 dB up to approximately 2 kHz independent of the OSL condition. Along with the phases at $\pm\pi$, this indicates that the inward fluid flow at the OW is nearly equal to the outward flow, consistent with the experimental data for AC stimulation reported by Stenfelt et al. (2004a). Between 2 kHz and 8 kHz, the simulation results with a flexible OSL show an increase of up to 8 dB,
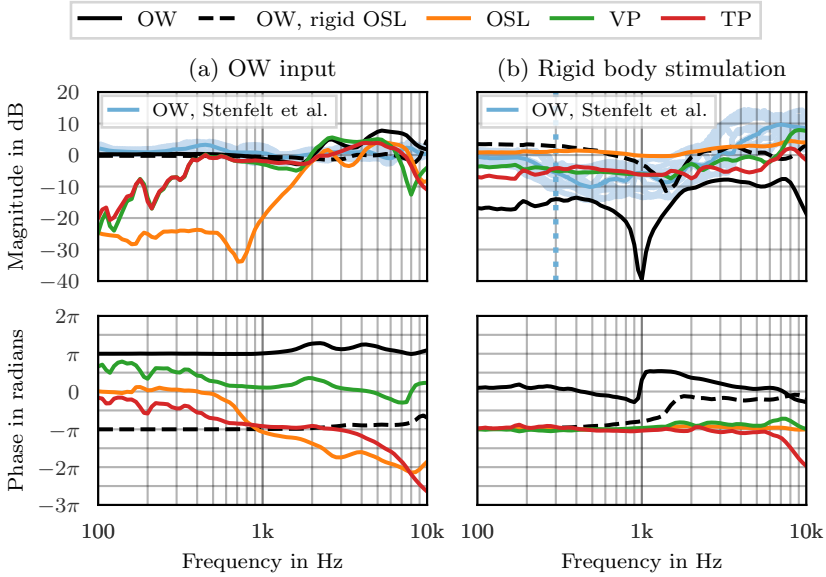
Figure 4.3: Magnitude and phase of the differential volume velocity contributions to the RW differential volume velocity for (a) input at the OW with fixed surroundings and (b) rigid body stimulation in the direction of the OW. Solid lines indicate the ratios $q_{\mathrm{ow,diff}}/q_{\mathrm{rw,diff}}$ (black), $q_{\mathrm{osl,diff}}/q_{\mathrm{rw,diff}}$ (orange), $q_{\mathrm{vp,diff}}/q_{\mathrm{rw,diff}}$ (green), and $q_{\mathrm{tp,diff}}/q_{\mathrm{rw,diff}}$ (red) with flexible OSL. Dashed black lines represent $q_{\mathrm{ow,diff}}/q_{\mathrm{rw,diff}}$ with a rigid OSL, while the other ratios are zero ($-\infty$ dB) under this condition. Experimental OW magnitude ratios from Stenfelt et al. (2004a) are shown in blue, corresponding to AC and BC stimulation in the original study, including individual data and mean values. The vertical dotted line indicates the lower frequency limit (300 Hz) for the validity of the experimental data in (b).

whereas the rigid OSL results align more closely with the experimental data, typically within 5 dB.

The VP and TP ratios (green and red lines) exhibit similar magnitudes below approximately 1 kHz, with a phase difference of π. This indicates that the VP and TP volume velocities largely cancel each other out. As sketched in Figure 4.1 (a), this cancellation results from their synchronous motion driven by the differential cochlear pressure acting on the OSL (Raufer et al., 2019). This synchronous motion leads to a differential OSL volume velocity (orange line) that is approximately 20–35 dB lower than the RW differential volume velocity in this frequency range. Above 2 kHz, the phase difference between the VP and TP curves diverges from π, indicating that the synchronous motion is partially superimposed by a deformation that varies between the VP and TP. This leads

to an increase of the OSL volume velocity with a slope of 60 dB per decade between 1–2 kHz, reaching values within 5 dB of the RW differential volume velocity between 2–8 kHz.

Rigid body stimulation

For rigid body stimulation [Figure 4.3 (b)], the RW differential volume velocity closely matches that of the OSL, as indicated by the orange line remaining near 0 dB in magnitude and zero in phase throughout the entire frequency range. This suggests that the RW differential volume velocity originates primarily from the OSL, which differs fundamentally from the case of OW input.

The VP and TP contributions (green and red lines) remain between −10 dB and 0 dB up to approximately 7 kHz, with a phase close to zero. This indicates a predominantly compressional differential motion of the OSL rather than deflection [Figure 4.1 (b)], such that the VP and TP contribute constructively to the overall OSL volume velocity without significant cancellation. Figure 4.2 (c) and (d) show that this compressional motion component is at least 10–20 dB lower than the translational motion component, with differences of up to 80 dB at low frequencies.

The OW differential volume velocity with flexible OSL (solid black line) is 10–20 dB lower than the RW differential volume velocity for rigid body stimulation. The notch at about 1 kHz from Figure 4.2 (b) – related to a pressure minimum inspected in more detail in Section 4.3.3 – reappears in Figure 4.3 (b). In contrast, with rigid OSL (dashed black lines), the RW and OW differential volume velocities are nearly equal in magnitude and phase, except for the notch at 1.5 kHz.

The experimental OW-to-RW differential volume velocity ratio reported by Stenfelt et al. (2004a) ranges between −5 dB and −10 dB on average from 400 Hz–2 kHz, with values increasing up to 10 dB toward 10 kHz. These differences between the OW and RW differential fluid flow are less pronounced than those observed in the simulations with flexible OSL, reflecting the discrepancies in OW differential volume velocity between measurement and simulation results already evident in Figure 4.2 (b).

4.3.3 Intracochlear sound pressure

To further investigate how the differential volume velocities are governed by intracochlear sound pressure, Figure 4.4 presents the sound pressure results in (a) the SV, and (b) the ST. Black lines indicate point probe evaluations for rigid body stimulation with flexible (solid) and rigid OSL (dashed), while green lines represent the average sound pressure over the OW surface under the same stimulation condition. Orange lines depict probe sound pressure data for BC
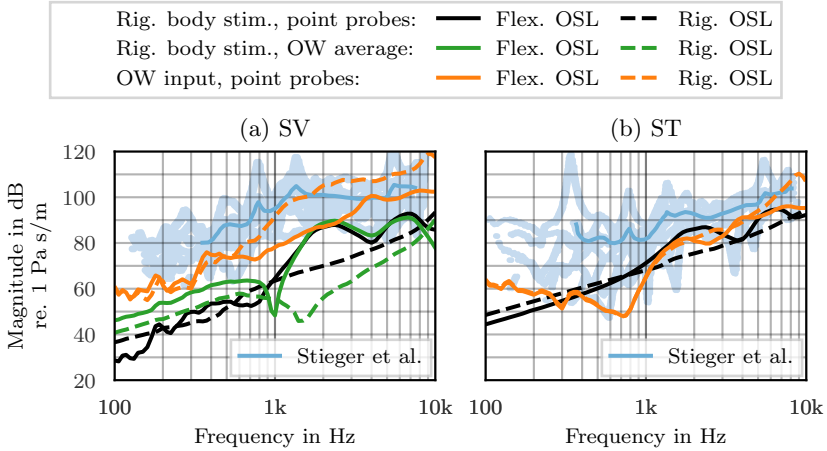
Figure 4.4: Magnitude of the sound pressure in (a) the SV and (b) the ST. Black and green lines show results for the rigid body stimulation condition, evaluated using point probes and pressure averaged over the OW surface, respectively. Orange lines present the sound pressure for BC input at OW. Solid lines indicate a flexible and dashed lines a rigid OSL. Experimental data from Stieger et al. (2018), measured using fiberoptic sensors in eight temporal bone specimens with intact MEs, is shown in blue (mean and individual data).

input at OW. The point probe positions correspond to those used in Chapter 3, consistent with experimental studies (Frear et al., 2018; Stieger et al., 2018). Experimental data from Stieger et al. (2018, Fig. 11), measured using fiberoptic sensors in SV and ST of temporal bone specimens with intact MEs under BC excitation, are included in blue as mean curves and individual data.

For rigid body stimulation with a rigid OSL (dashed black lines), the sound pressure in both the SV (a) and ST (b) increases with a slope of approximately 20 dB per decade. This indicates that the sound pressure is driven by the inertial behavior of the cochlear fluid. With a flexible OSL (solid black lines), the sound pressures remain within 5 dB of the rigid OSL condition up to 1 kHz. Above 1 kHz, they exhibit pronounced increases, with local maxima near 2 kHz and 7 kHz, reaching comparable magnitudes in both SV and ST.

These simulation results align with the lower range of values of the experimental data range (blue) in the SV above 2 kHz and in the ST across the entire frequency range. However, in the SV at frequencies below 1 kHz, the simulation results fall approximately 10–20 dB below the experimental values. This discrepancy arises because the experimental data represent the inner ear's response to BC stimulation without distinguishing between OW input and rigid body stim-

ulation. Indeed, the simulation results for BC input at the OW (orange lines) remain with the experimental range throughout the frequency range in both SV and ST. For this input, the OSL's flexibility reduces the SV sound pressure above approximately 500 Hz, consistent with the findings regarding the cochlear input impedance (Section 3.3.1). The ST sound pressure is less affected, with differences attributable to local pressure variations near the cochlear base, as observed for the RW impedance (cf. Section 3.4.1).

The OW average pressure for rigid body stimulation with a flexible OSL (solid green line) aligns with the SV probe pressure above approximately 1.5 kHz, but it is about 10 dB higher below 800 Hz. Comparing the OW average pressure characteristics to the OW differential volume velocity in Figure 4.2 (b) highlights that the OW volume velocity reflects the OW sound pressure, as enforced through the OW boundary condition detailed in Section 4.2.2. Accordingly, the notches observed at 1 kHz (flexible OSL) and 1.5 kHz (rigid OSL) in the volume velocity data Figure 4.2 (b) reappear in the OW average pressure in Figure 4.4 (a). Differences between OW average and probe pressures further illustrate the position dependence of the sound pressure under rigid body stimulation.

Figure 4.5 depicts the intracochlear pressure distributions for rigid body stimulation with flexible OSL in (b) and rigid OSL in (c). These correspond to the notch frequencies in Figure 4.2 (b) and Figure 4.4 (a). The pressure magnitudes (top row) are normalized to the respective intracochlear maximum.

For comparison, Figure 4.5 (a) shows the pressure distribution for OW input with flexible OSL at 1 kHz. In this case, the sound pressure is highest in the vestibule and basal part of the SV, showing a spatially uniform magnitude and phase distribution in this portion of the inner ear. The lowest pressure occurs near the RW, about 10–20 dB below the maximum, consistent with experimental ratios (Stieger et al., 2018, Fig. 12). Near the best frequency position, the sound pressure varies between SV and ST before converging to a constant value towards the apex [right in Figure 4.5 (a)].

For rigid body stimulation shown in Figure 4.5 (b) and (c), pressure minima form on planes perpendicular to the stimulation direction. The tangential alignments of these planes with the RW correspond to the notches in OW differential volume velocity and average pressure [Figure 4.2 (b), Figure 4.4 (a)]. The level differences between minima and maxima range from 30–60 dB, much greater than for OW input. The phase data (bottom row) reveal a π phase difference across these minima. Additionally, an inspection of the fluid particle velocity distribution (results not shown here) confirmed that the fluid motion largely follows the applied rigid body stimulation, as already observed in Figure 4.2.

Animations of these pressure distributions across frequencies are available at https://doi.org/10.5281/zenodo.14850065. These animations show that
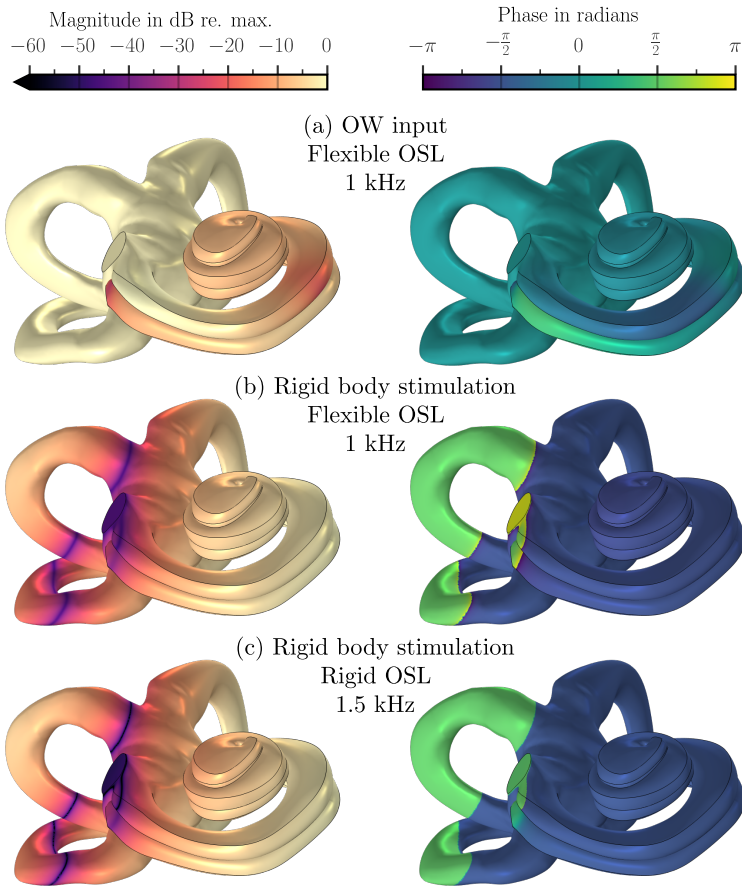
Figure 4.5: Sound pressure distributions on the outer surface of the inner ear for (a) input at the OW with flexible OSL at 1 kHz, (b) rigid body stimulation and flexible OSL at 1 kHz, and (c) rigid body stimulation and rigid OSL at 1.5 kHz. Magnitudes (top row) are normalized to the maximum pressure in the inner ear, the phase data is presented relative to the stimulation velocity.

with rigid OSL, the plane of minimum pressure perpendicular to the stimulation direction persist up to about 6 kHz, with slight frequency-dependent shifts in its position relative to the OW. With flexible OSL, similar patterns appear up to approximately 1.1 kHz, after which the distribution alternates between uniform and complex patterns, occasionally forming a minimum plane.

4.4 Discussion

As emphasized in Section 3.4, the numerical model of the inner ear should be viewed as a representation of an individual specimen rather than as a predictive model for average data. Its primary aim is to assess mechanisms and identify distinct phenomena related to the flexibility of the CP, with the understanding that the magnitudes of these effects and related quantities will naturally vary between individual ears. Additionally, a model-based approach necessarily simplifies the complex anatomy and physiology of the inner ear, especially of the OSL, so the results may not reflect all aspects of real-world behavior in precise detail. The complexity of assessing the inner ear's response to BC stimulation arises from the multiple pathways through which sound reaches the cochlea (Stenfelt and Goode, 2005a; Tonndorf, 1966, 1968). To address this, the mechanisms were separated between (1) contributions that enter the inner ear via the OW, modeled by applying measured average OW input while keeping the surroundings fixed (see Section 4.2.1), and (2) the fluid dynamics induced by rigid body motion of the surrounding structures (see Section 4.2.2). The investigations in this chapter focus on the fluid flow within the inner ear, assessed either by total volume velocities, reflecting the motion of the OW, RW and OSL surfaces, or by differential volume velocities, which capture the relative motion of these surfaces due to sound pressure loading. Furthermore, the relationship between volume velocities and intracochlear sound pressures has been examined, evaluating sound pressure in the SV and ST as well as spatial pressure distributions.

4.4.1 Total and differential motion of the osseous spiral lamina

A critical factor in evaluating the model predictions is recognizing the fundamentally different mechanisms driving OSL motion for OW input compared to rigid body motion of the inner ear's surroundings. For AC stimulation and BC contributors entering via the OW, the OSL reacts to the pressure difference between the SV and ST (Figure 4.5). This differential pressure leads to similar deflections of the VP and TP [schematic in Figure 4.1], resulting in a significant cancellation of their respective volume velocities [Figure 4.3 (a)]. These findings are consistent with measurements by Raufer et al. (2019), who reported a bend-

ing of the OSL similar to a plate hinged at the medial side. The simulations with AC stimulation in Chapter 3 demonstrated behavior consistent with these experimental observations.

In contrast, during rigid body stimulation, the OSL's motion involves two components: (1) translational motion with the inner ear's surroundings, and (2) deformation caused by fluid pressure induced by the stimulation. For rigid body stimulation, the sound pressures on both sides of the OSL are – in contrast to OW input – nearly equal (Figure 4.5). This results in a slight compression of the OSL [illustrated in Figure 4.1 (b)]. While only this compressional component contributes to the differential volume velocity, its magnitude is substantially smaller than that of the translational motion. This is evident from the differences of 20–80 dB between the VP and TP total and differential volume velocities below 4 kHz (Figure 4.2). Consequently, the VP and TP move largely synchronously during rigid body stimulation, which may explain why a differential volume velocity contribution of the OSL has not yet been recognized.

Thus, understanding the OSL's contribution to fluid flow in the inner ear under BC stimulation requires separately analyzing the motions of the VP and TP. Unfortunately, there is currently no experimental data available on these motions or for the OSL's volume velocity contribution. Experimentally assessing these effects poses significant challenges. The 20–80 dB differences between VP and TP total and differential volume velocities [Figure 4.2 (c) and (d)] provide an estimate of the signal-to-noise ratio needed to capture differential motion of the OSL (cf. Equation 4.3 and Equation 4.4). This dynamic range exceeds the capabilities of most current measurement methods. Additionally, high-resolution measurements of velocity distributions in both radial and longitudinal directions of the CP, separately for the VP and TP, would be necessary. These considerations highlight the significant experimental limitations that currently impede direct verification of the OSL's contribution to the fluid flow during BC stimulation, motivating the model-based approach.

4.4.2 Volume velocity contribution of the osseous spiral lamina

The equality in volume velocity between the OW and RW observed for OW input in Figure 4.3 (a) resembles experimental findings for AC stimulation (Kringlebotn, 1995; Stenfelt et al., 2004a). It results from the incompressibility of the fluid and the rigid boundaries of the inner ear, where an inward flow at the OW generates an equal outward flow at the RW (Frear et al., 2018; Stenfelt et al., 2004a).

In contrast, under BC stimulation, Stenfelt et al. (2004a) observed unequal volume velocities at the OW and RW in temporal bone specimens where ME structures, aside from the stapes footplate, had been removed. At frequencies

below 4 kHz, this inequality was later attributed to "third-window" effects in healthy ears, referring to fluid leakage through small channels or compliant structures within the cochlea (Stenfelt and Goode, 2005a). Notably, these studies did not specifically mention the OSL as one of the compliant structures when discussing this phenomenon.

Although other openings than the OW and RW have been excluded, simulations with rigid body stimulation and flexible OSL produced differences in both magnitude and phase between the differential volume velocities at the two windows [Figure 4.3 (b)], which are phenomenologically consistent with the experimental observations by Stenfelt et al. (2004a). The simulations further demonstrated a 0 dB ratio between the OSL and RW differential volume velocities [Figure 4.3 (b)], identifying the flexible OSL as the dominant contributor to RW volume velocity for the rigid body stimulation condition. In contrast, with a rigid OSL, the OW-to-RW volume velocity ratio remained near 0 dB, indicating equal differential fluid flow at both windows, similar to AC stimulation. These results suggest that the flexible OSL likely contributed to the experimentally measured inequality between OW and RW volume velocities below 4 kHz.

Above 4 kHz, Stenfelt et al. (2004a) observed larger differential volume velocities at the OW than at the RW, a phenomenon primarily attributed to deformations of the surrounding bone (Stenfelt and Goode, 2005a). Since the rigid body stimulation excluded such deformations, this limitation likely explains the discrepancies in the OW-to-RW volume velocity ratios at higher frequencies compared to the experimental results [Figure 4.3 (b)].

Despite these differences in the volume velocity ratios, the quantitative agreement between the simulated and measured RW differential volume velocities [Figure 4.2 (a)] is noteworthy, particularly given the substantial 30–40 dB increase due to OSL flexibility compared to the rigid OSL condition. This suggests that the magnitude discrepancies in the OW-to-RW volume velocity ratio below 4 kHz may primarily stem from differences in the OW differential volume velocities when compared to the measurements by Stenfelt et al. (2004a).

4.4.3 Oval window volume velocities and intracochlear sound pressure

By separating BC stimulation into input at the OW and rigid body stimulation, the approach highlights two distinct mechanisms contributing to the OW differential volume velocity during BC: (1) sound pressure acting on the stapes footplate as a reaction to inner ear motion, and (2) differential stapes motion due to sound originating from the ME or ear canal.

For rigid body stimulation, the total volume velocities [Figure 4.2 (b)] indicate that the OW surface primarily moves synchronously with the adjacent structures. The differential volume velocity, in this case, is exclusively driven by intracochlear pressure acting against the reverse ME impedance (Equation 4.5). This behavior is confirmed by the agreement between the characteristics of OW average pressure and OW differential volume velocity curves [Figure 4.4 (a) and Figure 4.2 (b)]. A notable difference between the simulation results and experimental data is the appearance of a notch in the OW differential volume velocity for rigid body stimulation [Figure 4.2 (b)]. This feature arises from pressure distribution patterns with a plane of minimum pressure normal to the stimulation direction (Figure 4.5). The position of this minimum plane varies slightly with frequency (cf. animations at `https://doi.org/10.5281/zenodo.14850065`) and aligns with the OW at approximately 1 kHz with flexible OSL and 1.5 kHz with rigid OSL. These variations, along with the disappearance of the pressure minimum in certain frequency ranges, can be attributed to the motion of the OSL, which modifies the pressure boundary conditions in the part of the inner ear comprising the SV and ST. Above approximately 1 kHz, the flexibility of the OSL increases the magnitude of both the OW average pressure and the OW differential volume velocity [Figure 4.4 and Figure 4.2 (b)].

For BC input at the OW, the OSL's flexibility does not influence the OW differential volume velocity by definition. The differential stapes motion used as input data for this stimulation condition (Section 4.2.1) was derived from measurements with intact middle and inner ears (Stenfelt et al., 2002). Following Stenfelt (2016), it has been assumed that the contributors entering via the OW dominate this measured differential motion. However, in these experiments, BC sound transmission from the ME and the reaction to intracochlear pressure were inseparable, so this input data may already contain an unknown contribution from the inner ear fluid pressure.

Up to 20 dB higher magnitudes were observed in the sound pressure probe evaluations in the simulation results for OW input compared to the rigid body stimulation (Section 4.3.3). This reflects how a small differential motion of the stapes footplate during OW input can generate a significantly higher pressure in the cochlear fluid than the pressure caused by the rigid body motion of the inner ear driving the stapes footplate from the inside. However, since the corresponding pressure distributions are uniquely different (Figure 4.5), the relationship of these pressure components is location dependent.

When comparing the simulated pressure results with experimental data, it is important to consider that the vibration directions for intracochlear sound pressure measurements vary across specimens and fluctuate with frequency (Dobrev et al., 2023; Stieger et al., 2018), resulting in significant experimental variability

(e.g., Borgers et al., 2019; Dobrev et al., 2023; Stieger et al., 2018). Even in temporal bone measurements with well-controlled primary stimulation directions (Stenfelt et al., 2004a, 2003a), stimulation velocity ratios of 3–10 (equivalent to 10–20 dB) were reported (Stenfelt et al., 2003a). Consequently, the pressure ranges of 30–60 dB and corresponding notches observed in the present simulations with strictly unidirectional excitation may appear less distinct in experiments due to additional pressure contributions from other directions. These considerations help explain why the simulated sound pressures for rigid body stimulation fall at the lower end – or below – the experimental values at the probe locations, while simulations for BC input at the OW remain within the experimental range (Figure 4.4).

It is also important to note that the experimental reference for OW differential volume velocity under BC stimulation was obtained after removal of the malleus, incus, and portions of the stapes (Stenfelt et al., 2004a), likely altering the mechanical impedance at the OW compared to intact ears. Additionally, sound pressure induced by inner ear deformation – excluded in the present simulations – may have influenced the OW differential volume velocity, particularly above 4 kHz (Stenfelt and Goode, 2005a). Considering these complexities, it is plausible that the experimental OW differential volume velocity magnitudes lie between the simulated results for OW input and rigid body stimulation below 3 kHz [Figure 4.2 (b)].

4.4.4 Role of the osseous spiral lamina in bone conduction hearing

The role of OSL motion has received limited attention in studies of BC hearing mechanisms. Stenfelt et al. (2003a) investigated BM and OSL motion under AC and BC stimulation, identifying relative motion between the OSL and the inner ear's surroundings. They concluded that the effect of OSL motion on BC hearing – termed "inertial OSL BC sound" – may contribute at higher frequencies but is likely not significant in healthy ears. However, the present findings suggest a more substantial role for the flexible OSL in BC hearing. Firstly, the impact of the OSL on BC hearing should be considered in light of the findings from Chapter 3 for BC sound entering via the OW. These results demonstrated that the OSL's flexibility affects the differential sound pressure and contributes an additional motion component to BM motion. Secondly, the results in this chapter suggest a significant contribution of the OSL to the fluid flow in the inner ear in response to vibrational stimulation.

Tonndorf (1966) listed the impedance of the CP – which is significantly influenced by the OSL's flexibility, see Chapter 3 – as a factor affecting the fluid

inertia effects during BC. This insight has been incorporated into lumped-element models of the inner ear (Guan et al., 2020; Stenfelt, 2015, 2016). However, the findings on the OSL's motion and volume velocity contribution suggest that the consideration of the CP via a single impedance should be revisited.

The RW, VP, and TP differential volume velocities exhibited similar magnitudes for both OW input and rigid body stimulation conditions (Figure 4.2), and the relation of these mechanisms in the intracochlear sound pressure responses was highly dependent on frequency (Figure 4.4) and position (Figure 4.5). These findings highlight that, while the OSL likely plays a substantial role in differential fluid flow during BC stimulation, quantitatively predicting its contribution remains challenging due to the uncertain and variable interactions between the BC mechanisms in real ears.

To further clarify the OSL's role, it is crucial to distinguish the different effects that have been regarded as "third windows" in BC hearing: sound transmission from the skull interior via the vestibular and cochlear aqueducts (Dobrev et al., 2022; Freeman et al., 2000; Sohmer and Freeman, 2004), leakage during RW simulation (Frear et al., 2018; Stieger et al., 2013), and inequality in fluid flow between the OW and RW during BC stimulation (Stenfelt et al., 2004a). Rosowski et al. (2018) pointed out that distinguishing the compressibility of the inner ear's content from anatomical "third windows" is challenging. In the present work, additional openings beyond the OW and RW were excluded, yet the simulation reproduced the fluid flow inequality observed by Stenfelt et al. (2004a). This result suggests that the flexibility of the OSL may play a significant role in this phenomenon. However, to the author's knowledge, the contribution of anatomical "third windows" to this effect has not been quantified for healthy ears.

4.4.5 Limitations and suggestions for future work

The limitations already identified in Chapter 3 – particularly, the use of a specific set of model parameters, the absence of active cochlear mechanisms, and the lack of representation of individual anatomical differences – are applicable to the present chapter, as the model remained essentially unchanged.

A key limitation specific to the current investigation is the simplified representation of the OSL. In the model, the OSL was treated as a sandwich-like solid structure, while in reality, both the VP and TP, along with the softer core, may be partially fluid-filled due to their porosity and semi-permeable nature. While the bending stiffness of the OSL – its most critical property influencing the inner ear's response to input at the OW – is likely governed primarily by its solid properties, this modeling approach may not fully capture its compress-

ibility, which could behave more fluid-like. Although this is unlikely to affect the identified mechanisms related to the OSL's compressibility, it may influence the magnitudes of the differential volume velocities observed during rigid body stimulation [Figure 4.2 (c) and (d)].

The simulations in this chapter focus on a specific direction of rigid body stimulation, aligning with the experimental conditions in Stenfelt et al. (2004a). While primary rigid body motion of the inner ear has been observed in these experiments (Stenfelt et al., 2004a) and cadaver head measurements (Dobrev et al., 2023), other studies highlighted the complexity related to such stimulation. Kim et al. (2014) and Zhao et al. (2021) reported directionality in the inner ear's BC response, while Dobrev et al. (2023) found no singular direction of motion in their cadaver head measurements. These findings underscore the need for future studies to incorporate multiple directions of stimulation to fully capture the OSL's effect on inner ear responses.

The BC stimulation was limited to two mechanisms, BC sound entering via the OW and rigid body stimulation, excluding deformation of the inner ear's surroundings (Dobrev et al., 2023; Stenfelt, 2015; Tonndorf, 1962). Two findings suggest the need for further investigation of compression and expansion of the inner ear. First, the differential volume velocity contribution of the OSL observed in the simulations arose from differences in VP and TP velocity distributions, but these velocities fall below current measurement thresholds. This highlights the importance of even minimal compressibilities in cochlear structures, which should be incorporated into future models. Particularly, rigid boundary conditions could be reconsidered by including structures such as the spongy bone of the modiolus and potential flexibility of the thin walls between cochlear turns (cf. Raufer et al., 2020, Fig. 2a). Secondly, the experimental observation of greater OW than RW differential velocities for BC stimulation above 4 kHz (Stenfelt et al., 2004a) was attributed to cochlear bone deformation (Stenfelt and Goode, 2005a). The simulations presented here could not replicate this phenomenon through either of the two stimulation conditions or the OSL's role as a "third window", supporting hypotheses that cochlear bone deformation plays an important role at higher frequencies.

4.5 Summary

This chapter investigates how the flexibility of the CP affects the fluid flow in the inner ear during BC stimulation by modeling the OSL as either rigid or flexible structure in a FE model of the human inner ear. Accounting for the OSL's sandwich-like anatomy enabled to separate the contributions from the VP and TP. Additionally, two BC stimulations were accounted for: (1) BC contributors

entering via the OW and (2) rigid body stimulation, while excluding inner ear deformation and OW input for the latter.

During rigid body stimulation, the OSL significantly contributes to the differential volume velocity at the RW, resulting in an increased differential fluid flow at the RW compared to the OW. This phenomenon aligns with experimental observations previously interpreted as "third-window" effects. Analysis of the OSL motion indicated that its contribution arises from compressional motion. However, this motion component is several orders of magnitude smaller than the motion associated with the rigid body stimulation. In contrast, under OW input, the OSL's flexibility had only minor influence on the differential volume velocities at the two windows. Comparisons of the simulation results for the two types of stimulation and experimental data, where responses inherently reflect a mixture of BC mechanisms, provided insights into the interaction of BC sound entering via the OW and the stapes' reaction to complex sound pressure distributions within the inner ear.

Together with the findings from Chapter 3, these results suggest a more important role for the OSL in AC and BC hearing than previously recognized.

5

Conclusion and outlook

5.1 Summary

Hearing involves various vibroacoustic mechanisms, interactions, and pathways. To further improve the user experience with hearing technologies, a more detailed understanding of the physics behind these complex phenomena is needed. These investigations require not only examining sound and vibration at the EC but also investigating the vibroacoustic behavior of the inner ear, which serves as the sensor for all AC and BC pathways. Given the challenges of experimentally assessing these mechanisms, modeling and numerical simulations are essential tools for advancing our understanding of hearing.

This thesis adopts a focused modeling approach, systematically "zooming in" on AC and BC mechanisms across auditory subsystems to gain detailed insights into the underlying vibroacoustic phenomena. One application of such modeling is the perception of one's own voice, which arises from a combination of AC and BC hearing. The alteration of this perception is a prominent example of the OE, a major source of dissatisfaction among users of hearing aids (Dillon, 2012b; Hengen et al., 2020; Winkler et al., 2016) and hearing protection devices (Doutres et al., 2019). Beyond self-perception, these simulations have important applications in other areas of audiology, such as BC hearing aids (Kompis and Caversaccio, 2011).

Chapter 2 examines how non-deforming motion of parts of the EC affects the sound pressure at the TM and contributes to the OE. This motion complements EC wall vibrations in generating BC-stimulated sound pressure, especially at low frequencies. An impedance boundary condition was introduced to account for this phenomenon. The results show that the motions of the EC entrance and TM reduce the EC sound pressure at low frequencies, particularly in occluded conditions, leading to a reduction in the OE. These mechanisms may contribute to

higher variability of experimental OE data (Reinfeldt et al., 2013; Saint-Gaudens et al., 2022) and to discrepancies between OE simulations and measurements (Brummund et al., 2014; Carillo et al., 2021b; Xu et al., 2021)

Chapter 3 presents an anatomical FE model of the human inner ear to investigate the role of the CP's flexibility, focussing on input at the OW. The results suggest that the motion of the OSL significantly influences cochlear impedances (Frear et al., 2018), CP stiffness (Békésy, 1960), and overall CP motion (Gundersen et al., 1978; Raufer et al., 2019; Stenfelt et al., 2003a). These findings highlight the importance of accounting for the flexibilities of the OSL and CPB when interpreting experimental data, challenging classical modeling approaches that assume a rigid OSL and neglect the CPB.

Chapter 4 extends the inner ear simulations to include the rigid body motion component in the BC stimulation of the inner ear, focusing on the contribution of the OSL to intracochlear fluid flow. The simulations suggest that compressional motion of the OSL significantly contributes to an increased differential volume velocity at the RW compared OW during BC, potentially explaining experimental observations previously interpreted as "third-window" effects (Stenfelt et al., 2004a).

5.2 Suggestions for future work

Relative importance of air and bone conduction mechanisms

The strength of the approach in this thesis lies in isolating specific mechanisms of AC and BC hearing by focusing separately on different parts of the auditory system. However, this approach also presents a key limitation: it does not resolve the relative importance of these mechanisms.

To address this, Stenfelt (2016, 2020) combined experimental data with a lumped-element model of the inner ear. While insightful, these predictions were limited to a single stimulation condition with a BC transducer positioned at the mastoid. Moreover, as discussed in Chapter 4, the experimental input data introduces uncertainties due to the inherent mixing of BC mechanisms. Additionally, many findings from the FE simulations in Chapter 3 and Chapter 4 cannot be captured by lumped-element inner ear models.

To overcome these limitations, full-head FE models have been developed, integrating all relevant structures such as the EC, middle ear, and inner ear (Lim et al., 2022; Taschke, 2005). The model by Lim et al. (2022) is particularly effective for interpreting experimental data from BC hearing aids (Dobrev et al., 2025; Lim et al., 2023, 2022, 2024). However, a key finding of this thesis is the critical role of OSL flexibility and the presence of the CPB in inner ear mechanics, suggesting that the OSL contributes more substantially to both AC

and BC hearing than previously recognized. To the author's knowledge, current full-head models do not incorporate these structures as flexible components, pointing towards an important area for model refinement.

Moreover, interpreting inner ear responses in these simulations is challenging because the BC pathways cannot be separated. Therefore, revisiting the FE approach by Taschke (2005) offers a promising direction for future research. A unique feature of this approach was the strategic separation of the auditory system at the TM and OW, enabling isolated analysis of the BC mechanisms without altering the system's vibroacoustic behavior. This concept significantly inspired the approach adopted in this thesis.

Mechanisms contributing to ear canal sound pressure

The findings in Chapter 2 highlight the need to distinguish between various mechanisms that contribute to the EC sound pressure under open and occluded conditions. Among these, only one mechanism – the motions of the EC entrance and TM – was examined in detail. Discrepancies in the open TM sound pressure remain between the proposed circuit model (Figure 2.2) and the FE model by Xu et al. (2021) with radiation impedance at the EC entrance (Figure A.2), as well as in FE stimulations between radiation impedance and surrounding air conditions (Figure A.3). To address these discrepancies, the circuit model introduced in Chapter 2 could be extended to incorporate additional factors, including:

- sound pressure radiated into the open EC, resulting from BC-stimulated head vibrations (Stenfelt et al., 2003b; Xu et al., 2021) or one's own voice (Pörschmann, 2000);
- deformation of occluding devices relative to the EC motion (i.e., Poisson's effect) (Carillo et al., 2021b);
- radiation from ME structures into the EC (Ravicz et al., 2019; Schroeter and Poesselt, 1986; Stenfelt et al., 2003b); and
- sound pressure in the tympanic cavity causing TM deflection (Dobrev et al., 2020; Stenfelt et al., 2002; Tonndorf, 1968).

Additionally, the frequency-dependent positioning of the wall vibration source (Carillo et al., 2020, 2021c), modeled as frequency-independent in Chapter 2, may help in further resolving discrepancies between circuit and FE models. To clarify the relative contributions of the different mechanisms and refine OE models, further numerical simulations and measurements of EC vibrations are indispensable, particularly to gain more insights into the interactions between the structural motion of the EC, the occluding device, and the sound pressure at the TM (Carillo et al., 2021b). These investigations should also consider excitation dependencies

(Reinfeldt et al., 2013; Saint-Gaudens et al., 2022) and the influence of the jaw (Denk et al., 2022; Franke et al., 1952; Stenfelt et al., 2003a).

Modeling the subjective occlusion effect and own-voice perception

Integrating the insights into the BC pathways and the EC sound pressure into comprehensive full-head FE models could enhance our understanding of the subjective perception of the OE. This approach may help resolve discrepancies between measured EC sound pressures and subjective perception in both open and occluded conditions (Reinfeldt et al., 2013; Saint-Gaudens et al., 2022; Stenfelt and Reinfeldt, 2007). Including – at some point – also the physics of voice production or non-linear cochlear mechanisms would bring the models even closer to the real-world physics, however, while introducing entirely new levels of complexity. In this regard, this thesis has only begun to address these challenges, focusing on the mechanisms at the "receiver side" of the sound transmission during vocalization.

Improvements in hearing technology

While this thesis primarily focuses on fundamental research, it is the author's desire that these findings, along with the future efforts outlined above, will contribute to practical advances in hearing technology. Potential applications include physics-driven algorithms for hearing devices, improved designs for earmolds and earplugs, and optimizations in BC hearing aids. These advancements will support individuals with hearing impairment, or reduce the occurrence of hearing loss by enhancing hearing protection.

A

Appendix

A.1 Finite element simulations to obtain ear canal volume velocities

To obtain volume velocities associated with the EC entrance, TM and EC wall, an open and perfectly occluded condition were applied at the EC entrance in the full-head FE model developed by Xu et al. (2021), at the position termed "E1" in the original study. The same impedances were used for the FE simulations and the circuit calculations, both at the EC entrance and TM. The circuit impedances (in $\mathrm{Pa\,s/m^3}$) were multiplied with the area of the corresponding boundary surfaces to apply them locally as specific acoustic impedances (in $\mathrm{Pa\,s/m}$) in the FE model. To account for the structural motion at the boundaries represented by acoustic impedances, the underlying equations in the software COMSOL Multiphysics® v.6.1 (COMSOL AB, Stockholm, Sweden), which was used for the FE simulations, were manually modified as described in Section 2.2.2. Given these simulation parameters, the volume velocities $q_{\mathrm{w,s}}^{\mathrm{open}}$ and $q_{\mathrm{w,s}}^{\mathrm{occl}}$ were extracted according to Equation 2.2, and $q_{\mathrm{e,s}}^{\mathrm{open}}$, $q_{\mathrm{e,s}}^{\mathrm{occl}}$, $q_{\mathrm{tm,s}}^{\mathrm{open}}$, and $q_{\mathrm{tm,s}}^{\mathrm{occl}}$ were obtained according to Equation 2.6. The volume velocities are shown in Figure A.1. The inspected frequency range included the third octave bands from 0.1–1 kHz. The frequency resolution was set to 24 frequencies per octave.
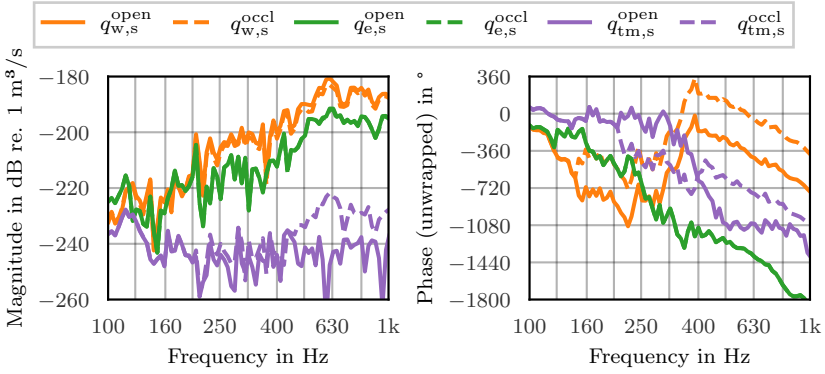
Figure A.1: Magnitude and unwrapped phase of the volume velocities extracted from the FE simulations for BC stimulation of 1 N at the ipsilateral mastoid (right ear).

A.2 Validation of occlusion effect circuit calculations

To ensure the circuit calculations to be representative in highlighting the OE mechanisms involved, the calculations were verified using the full-head FE model (Xu et al., 2021) by simulating the TM pressure for the open-ear condition with radiation impedance and perfectly occluded condition with infinite impedance at the EC entrance. The comparison is shown in Figure A.2.
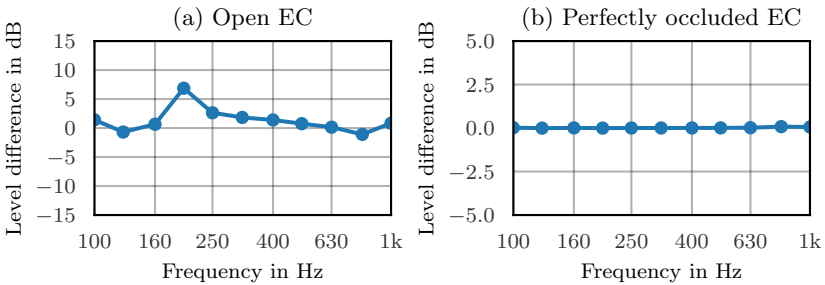
Figure A.2: Comparison between the TM sound pressure from the circuit calculations and the FE simulations with a full-head model (Xu et al., 2021) for the open and perfectly occluded impedance conditions at the EC entrance.

With perfectly occluded EC, the sound pressure level difference between the FE simulation and circuit calculation is generally negligible within the examined frequency range. For the open EC, the level difference is relatively small except in the 200 Hz third octave band, where the circuit calculated sound pressure is about 6 dB higher than in the FE simulation. This difference may be attributed to the assumption of a constant length for the EC segments (8 mm and 19.7 mm) across all frequencies. This is a simplification of the potentially frequency-dependent effect where the air in the EC is split up into an inertia-dominated part towards the EC entrance and a compliant section towards the TM (Carillo et al., 2021a). However, it is crucial to note that this simplification does not compromise the fundamental findings in Chapter 2 regarding the impact of the motions of the EC entrance plane and TM on TM sound pressure. This is best illustrated by the negligible difference between the circuit calculation and FE simulation for the perfectly occluded EC in Figure A.2, though the effect of the different contributors to the TM sound pressure is most pronounced in this case [Figure 2.4 (b)].

A.3 Radiation into the open ear canal

In addition to the radiation impedance at the EC entrance, a FE simulation with the full-head developed by Xu et al. (2021) and a "perfectly matched layer" around the head was conducted. This setup matched the corresponding setup in Xu et al. (2021, Fig. 8), but with including the impedance boundary condition at the TM according to Section 2.2.2. Compared to the radiation impedance at the EC entrance, this simulation condition also accounts for the exterior radiation of the BC-stimulated head vibrations into the EC. The difference between the resulting TM pressure simulations is shown in Figure A.3. The main effect of the sound propagation from the exterior into the EC is an increase of the TM sound pressure below approximately 300 Hz. This effect further reduces the resulting OE compared to Figure 2.3. Note that this contribution to the TM sound pressure in the open ear is not represented within the circuit model utilized for the investigations in this thesis.
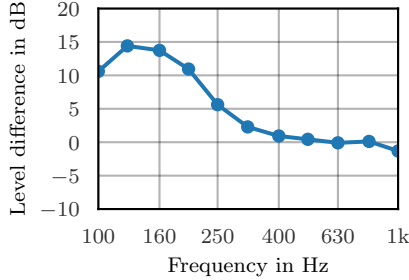
Figure A.3: Comparison between the TM sound pressure from the FE simulations with radiation impedance conditions at the EC entrance and a "perfectly match layer" around the head following Xu et al. (2021).

A.4 Cochlear partition coordinates

The CP coordinates in the FE model of the inner ear introduced in Chapter 3, u_s and u_r, were derived numerically by solving a series of differential equations. Initially, the equation $\Delta u_s = 0$ was solved on the mutual edge of the BM/CPB boundary and the SL with boundary conditions $u_s = 0$ at the base and $u_s = 1$ at the apex, yielding a linear mapping along the longitudinal direction of the CP. This mapping was extended onto the BM/CPB boundary, into the OSL, and SL domain by sequentially solving $\Delta u_s = 0$ in each domain. The initial solution served as the boundary condition on the OSL edge, supplemented by a prescribed value of $u_s = 1$ at edges at the apex. Radial coordinates u_r were determined along the BM/CPB boundary by solving $\Delta u_r = 0$, with boundary conditions set
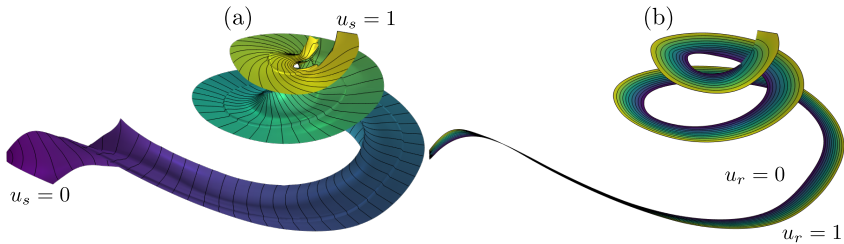
Figure A.4: Illustration of longitudinal CP coordinates (u_s) from 0 (dark blue) at the base to 1 (yellow) at the apex (a), and radial coordinates (u_r) from 0 at the medial edge to 1 at the lateral edge of the BM/CPB boundary (b). Black contour lines represent distances of 0.01 (a) and 0.1 (b), respectively.

to $u_r = 0$ at the medial edge connected to the OSL and $u_r = 1$ at the lateral edge connected to the SL. The coordinates are illustrated in Figure A.4.

Local unit vectors of the CP coordinate system (r, s, and t) were defined to implement anisotropic material properties (Fleischer et al., 2010). Here, s points longitudinally from base to apex, calculated as the normalized gradient of u_s, while t points perpendicularly from ST to SV. r points radially from OSL to SL, obtained as the cross product of s and t.

Glossary

Acronyms

AC	air conduction
BC	bone conduction
BM	basilar membrane
CP	cochlear partition
CPB	cochlear partition bridge
EC	ear canal
FE	finite element
ME	middle ear
OE	occlusion effect
OSL	osseous spiral lamina
OW	oval window
RW	round window
SL	spiral ligament
ST	scala tympani
SV	scala vestibuli
TM	tympanic membrane
TP	tympanic plate
VP	vestibular plate

Notation

$\langle \mathbf{v} \rangle$	Component wise average of a vector over a surface or line
$\mathbf{M}$	Matrix
$\mathbf{v}$	Vector
$\lvert v \rvert$	Absolute value of a (complex-valued) quantity

Symbols

A	Area
E	Young's modulus
G	Shear modulus
S	Surface
T	Volume velocity transfer function
Z	Acoustic impedance
$\mathbf{K}$	Two-port matrix representing an acoustical transmission line
$\mathbf{v}_\mathrm{s}$	Structural velocity vector
$\mathbf{v}$	Acoustic particle velocity vector
$\mathbf{x}$	Position in space
η	Structural loss factor
γ	Normalized differential velocity
$\mathbf{n(x)}$	Unit vector perpendicular to a surface at position $\mathbf{x}$ directed outward from a fluid
ν	Poisson's ratio
ω	Angular frequency
ρ	Density
c	Speed of sound
d	Thickness
l	Length
p	Sound pressure
q	Volume velocity
r	Radius
u_r, u_s	Radial and longitudinal CP coordinates
v_s	Normal component of structural velocity vector
$v_\mathrm{stap}, v_\mathrm{prom}$	Measured velocities of stapes footplate and cochlear promontory
v	Normal component of acoustic particle velocity
x, y, z	Cartesian coordinates
z	Specific acoustic impedance

Bibliography

Agrawal, S., Schart-Morén, N., Liu, W., Ladak, H. M., Rask-Andersen, H., and Li, H. (2018). "The Secondary Spiral Lamina and Its Relevance in Cochlear Implant Surgery". In: *Upsala J. Med. Sci.* 123.1, pp. 9–18. DOI: 10.1080/03009734.2018.1443983.

Aibara, R., Welsh, J. T., Puria, S., and Goode, R. L. (2001). "Human Middle-Ear Sound Transfer Function and Cochlear Input Impedance". In: *Hear. Res.* 152.1, pp. 100–109. DOI: 10.1016/S0378-5955(00)00240-9.

Akhmanova, M., Osidak, E., Domogatsky, S., Rodin, S., and Domogatskaya, A. (2015). "Physical, Spatial, and Molecular Aspects of Extracellular Matrix of In Vivo Niches and Artificial Scaffolds Relevant to Stem Cells Research". In: *Stem Cells Int.* 2015, p. 167025. DOI: 10.1155/2015/167025.

Anson, B. and Donaldson, J. (1981). *Surgical Anatomy of the Temporal Bone*. Philadelphia, London, Toronto: W.B. Saunders company.

Atalla, N. and Sgard, F. (2015). *Finite Element and Boundary Methods in Structural Acoustics and Vibration*. CRC Press. 466 pp.

Atturo, F., Barbara, M., and Rask-Andersen, H. (2014a). "On the Anatomy of the 'hook' Region of the Human Cochlea and How It Relates to Cochlear Implantation". In: *Audiol. Neurotol.* 19.6, pp. 378–385. DOI: 10.1159/000365585.

— (2014b). "Is the Human Round Window Really Round? An Anatomic Study With Surgical Implications". In: *Otol. Neurotol.* 35.8, p. 1354. DOI: 10.1097/MAO.0000000000000332.

Auperrin, A., Delille, R., Lesueur, D., Bruyère, K., Masson, C., and Drazétic, P. (2014). "Geometrical and Material Parameters to Assess the Macroscopic Mechanical Behaviour of Fresh Cranial Bone Samples". In: *J. Biomech.* 47.5, pp. 1180–1185. DOI: 10.1016/j.jbiomech.2013.10.060.

Békésy, G. von (1960). *Experiments in Hearing*. McGraw-Hill Series in Psychology. New York: McGraw-Hill.

Bennett, B., Bothe, E., and Ferguson, M. (2023). "A New Service Delivery Model for Hearables". In: *The Hearing Journal* 76.07, p. 21. DOI: 10.1097/01.HJ.0000946080.87791.78.

Bhatt, K. A., Liberman, M. C., and Nadol, J. B. (2001). "Morphometric Analysis of Age-Related Changes in the Human Basilar Membrane". In: *Ann. Otol. Rhinol. Laryngol.* 110.12, pp. 1147–1153. DOI: 10.1177/000348940111001212.

Böhnke, F. and Arnold, W. (1999). "3D-Finite Element Modelof the Human Cochlea Including Fluid-Structure Couplings". In: *ORL* 61.5, pp. 305–310. DOI: 10.1159/000027688.

Bom Braga, G. O., Parrilli, A., Zboray, R., Bulatović, M., and Wagner, F. (2023). "Quantitative Evaluation of the 3D Anatomy of the Human Osseous Spiral Lamina Using MicroCT". In: *J. Assoc. Res. Otolaryngol.* 24.4, pp. 441–452. DOI: 10.1007/s10162-023-00904-3.

Borgers, C., Fierens, G., Putzeys, T., van Wieringen, A., and Verhaert, N. (2019). "Reducing Artifacts in Intracochlear Pressure Measurements to Study Sound Transmission by Bone Conduction Stimulation in Humans". In: *Otol. Neurotol.* 40.9, e858. DOI: 10.1097/MAO.0000000000002394.

Borges, R. C., Costa, M. H., Cordioli, J. A., and Assuiti, L. F. C. (2013). "An Adaptive Occlusion Canceller for Hearing Aids". In: *21st European Signal Processing Conference (EUSIPCO 2013)*. 21st European Signal Processing Conference (EUSIPCO 2013), pp. 1–5. URL: https://ieeexplore.ieee.org/abstract/document/6811584.

Brummund, M. K., Sgard, F., Petit, Y., and Laville, F. (2014). "Three-Dimensional Finite Element Modeling of the Human External Ear: Simulation Study of the Bone Conduction Occlusion Effect". In: *J. Acoust. Soc. Am.* 135.3, pp. 1433–1444. DOI: 10.1121/1.4864484.

Brummund, M. K., Sgard, F., Petit, Y., Laville, F., and Nélisse, H. (2015). "An Axisymmetric Finite Element Model to Study the Earplug Contribution to the Bone Conduction Occlusion Effect". In: *Acta Acust. united Ac.* 101.4, pp. 775–788. DOI: 10.3813/AAA.918872.

Carillo, K., Doutres, O., and Sgard, F. (2020). "Theoretical Investigation of the Low Frequency Fundamental Mechanism of the Objective Occlusion Effect Induced by Bone-Conducted Stimulation". In: *J. Acoust. Soc. Am.* 147.5, pp. 3476–3489. DOI: 10.1121/10.0001237.

— (2021a). "On the Removal of the Open Earcanal High-Pass Filter Effect Due to Its Occlusion: A Bone-Conduction Occlusion Effect Theory". In: *Acta Acust.* 5. DOI: 10.1051/aacus/2021029.

— (2021b). "Numerical Investigation of the Earplug Contribution to the Low-Frequency Objective Occlusion Effect Induced by Bone-Conducted Stimulation". In: *J. Acoust. Soc. Am.* 150.3, pp. 2006–2023. DOI: 10.1121/10.0006209.

— (2021c). "Principle of an Acoustical Method for Estimating the Centroid Position of the Earcanal Wall Normal Velocity Induced by Bone-Conducted Stimulation: Numerical Evaluation". In: *Appl. Acoust.* 182, p. 108245. DOI: 10.1016/j.apacoust.2021.108245.

Carillo, K., Sgard, F., Dazel, O., and Doutres, O. (2022). "Reduction of the Occlusion Effect Induced by Earplugs Using Quasi Perfect Broadband Absorption". In: *Sci. Rep.* 12.1, p. 15336. DOI: 10.1038/s41598-022-19641-3.

— (2023). "Passive Earplug Including Helmholtz Resonators Arranged in Series to Achieve Broadband near Zero Occlusion Effect at Low Frequencies". In: *J. Acoust. Soc. Am.* 154.4, pp. 2099–2111. DOI: 10.1121/10.0021185.

Chang, Y., Kim, N., and Stenfelt, S. (2016). "The Development of a Whole-Head Human Finite-Element Model for Simulation of the Transmission of Bone-Conducted Sound". In: *J. Acoust. Soc. Am.* 140.3, pp. 1635–1651. DOI: 10.1121/1.4962443.

Cohen, D., Blinder, G., Perez, R., and Raveh, D. (2005). "Standardized Computed Tomographic Imaging and Dimensions of the Round-Window Niche". In: *Int. Tinnitus J.* 11.2, pp. 158–162.

Dallos, P. (1992). "The Active Cochlea". In: *J. Neurosci.* 12.12, pp. 4575–4585. DOI: 10.1523/JNEUROSCI.12-12-04575.1992.

De Proost, M., Segers, S., and Mertes, H. (2024). "Age-Related Hearing Loss and "Hearables": An Agenda for Moral Considerations". In: *Bioethics* 38.9, pp. 778–786. DOI: 10.1111/bioe.13327.

Denk, F., Hieke, T., Roberz, M., and Husstedt, H. (2022). "Occlusion and Coupling Effects with Different Earmold Designs – All a Matter of Opening the Ear Canal?" In: *Int. J. Audiol.* DOI: 10.1080/14992027.2022.2039966.

Denk, F., Jürgensen, L., and Husstedt, H. (2024). "Evaluation of Active Occlusion Effect Cancellation in Earphones by Subjective, Real-Ear and Coupler Measurements". In: *J. Audio Eng. Soc.* 72.3, pp. 145–160. DOI: 10.17743/jaes.2022.0124.

Dillon, H. (2012a). *Hearing Aids*. Second. Sydney: Boomerang Press. 608 pp.

— (2012b). "Venting and the Occlusion Effect". In: *Hearing Aids*. Second. Sydney: Boomerang Press, pp. 140–144.

Dobrev, I., Farahmandi, T., Pfiffner, F., and Röösli, C. (2022). "Intracochlear Pressure in Cadaver Heads under Bone Conduction and Intracranial Fluid Stimulation". In: *Hear. Res.*, p. 108506. DOI: 10.1016/j.heares.2022.108506.

Dobrev, I., Farahmandi, T. S., and Röösli, C. (2020). "Experimental Investigation of the Effect of Middle Ear in Bone Conduction". In: *Hear. Res.* 395, p. 108041. DOI: 10.1016/j.heares.2020.108041.

Dobrev, I., Lim, J., Kim, N., Niermann, J., Röösli, C., and Pfiffner, F. (2025). "Exploration of the Dynamics of Otic Capsule and Intracochlear Pressure: Numerical Insights with Experimental Validation". In: *J. Acoust. Soc. Am.* 157.1, pp. 554–568. DOI: 10.1121/10.0034859.

Dobrev, I., Pfiffner, F., and Röösli, C. (2023). "Intracochlear Pressure and Temporal Bone Motion Interaction under Bone Conduction Stimulation". In: *Hear. Res.* 435, p. 108818. DOI: 10.1016/j.heares.2023.108818.

Dobrev, I. and Sim, J. H. (2018). "Magnitude and Phase of Three-Dimensional (3D) Velocity Vector: Application to Measurement of Cochlear Promontory Motion during Bone Conduction Sound Transmission". In: *Hear. Res.* 364, pp. 96–103. DOI: 10.1016/j.heares.2018.03.022.

Doutres, O., Sgard, F., Terroir, J., Perrin, N., Jolly, C., Gauvin, C., and Negrini, A. (2019). "A Critical Review of the Literature on Comfort of Hearing Protection Devices: Definition of Comfort and Identification of Its Main Attributes for Earplug Types". In: *Int. J. Audiol.* 58.12, pp. 824–833. DOI: 10.1080/14992027.2019.1646930.

Fleischer, M., Schmidt, R., and Gummer, A. (2010). "Compliance Profiles Derived from a Three-Dimensional Finite-Element Model of the Basilar Membrane". In: *J. Acoust. Soc. Am.* 127.5, pp. 2973–2991. DOI: 10.1121/1.3372752.

Franke, E. K., von Gierke, H. E., Grossman, F. M., and von Wittern, W. W. (1952). "The Jaw Motions Relative to the Skull and Their Influence on Hearing by Bone Conduction". In: *J. Acoust. Soc. Am.* 24.2, pp. 142–146. DOI: 10.1121/1.1906868.

Frear, D. L., Guan, X., Stieger, C., Rosowski, J. J., and Nakajima, H. H. (2018). "Impedances of the Inner and Middle Ear Estimated from Intracochlear Sound Pressures in Normal Human Temporal Bones". In: *Hear. Res.* 367, pp. 17–31. DOI: 10.1016/j.heares.2018.06.019.

Freeman, S., Sichel, J.-Y., and Sohmer, H. (2000). "Bone Conduction Experiments in Animals – Evidence for a Non-Osseous Mechanism". In: *Hear. Res.* 146.1, pp. 72–80. DOI: 10.1016/S0378-5955(00)00098-8.

Gan, R. Z., Reeves, B. P., and Wang, X. (2007). "Modeling of Sound Transmission from Ear Canal to Cochlea". In: *Ann. Biomed. Eng.* 35.12, pp. 2180–2195. DOI: 10.1007/s10439-007-9366-y.

Goycoolea, M. V. and Lundman, L. (1997). "Round Window Membrane. Structure Function and Permeability: A Review". In: *Microsc. Res. Tech.* 36.3, pp. 201–211. DOI: 10.1002/(SICI)1097-0029(19970201)36:3<201::AID-JEMT8>3.0.CO;2-R.

Gray, H. and Lewis, W. H. (1918). *Anatomy of the Human Body.* Lea & Febiger. 1402 pp.

Greenwood, D. D. (1990). "A Cochlear Frequency-position Function for Several Species—29 Years Later". In: *J. Acoust. Soc. Am.* 87.6, pp. 2592–2605. DOI: 10.1121/1.399052.

Guan, X., Cheng, Y., Galaiya, D., Rosowski, J., Lee, D., and Nakajima, H. (2020). "Bone-Conduction Hyperacusis Induced by Superior Canal Dehiscence in Human: The Underlying Mechanism". In: *Sci. Rep.* 10.1. DOI: 10.1038/s41598-020-73565-4.

Gundersen, T., Skarstein, ø., and Sikkeland, T. (1978). "A Study of the Vibration of the Basilar Membrane in Human Temporal Bone Preparations by the Use of the Mossbauer Effect". In: *Acta Oto-Laryngol.* 86.1–6, pp. 225–232. DOI: 10.3109/00016487809124740.

Haile, L. M. et al. (2021). "Hearing Loss Prevalence and Years Lived with Disability, 1990–2019: Findings from the Global Burden of Disease Study 2019". In: *The Lancet* 397.10278, pp. 996–1009. DOI: 10.1016/S0140-6736(21)00516-X.

Hammond, E. and Diedesch, A. C. (2023). "Usability and Perceived Benefit of Hearing Assistive Features on Apple AirPods Pro". In: *Proceedings of Meetings on Acoustics* 51.1, p. 050004. DOI: 10.1121/2.0001771.

Hansen, M. Ø. (1998). "Occlusion Effects, Part II: A Study of the Occlusion Effect Mechanism and the Influence of the Earmould Properties". PhD thesis. Lyngby, Denmark: Technical University of Denmark.

EuroTrack (2020). *Hearing Aids Improve Hearing - and a LOT More Trends Derived from the EuroTrack Databases 2009 - 2020*. European Hearing Instrument Manufacturers Association (EHIMA). URL: https://www.ehima.com/wp-content/uploads/2020/07/EuroTrak-Trends-2009-2020-June-2020.pdf.

Heim, A. J., Matthews, W. G., and Koob, T. J. (2006). "Determination of the Elastic Modulus of Native Collagen Fibrils via Radial Indentation". In: *Appl. Phys. Lett.* 89.18, p. 181902. DOI: 10.1063/1.2367660.

Hengen, J., Hammarström, I. L., and Stenfelt, S. (2020). "Perception of One's Own Voice After Hearing-Aid Fitting for Naive Hearing-Aid Users and Hearing-Aid Refitting for Experienced Hearing-Aid Users". In: *Trends Hear.* 24, p. 2331216520932467. DOI: 10.1177/2331216520932467.

Homma, K., Du, Y., Shimizu, Y., and Puria, S. (2009). "Ossicular Resonance Modes of the Human Middle Ear for Bone and Air Conduction". In: *J. Acoust. Soc. Am.* 125.2, pp. 968–979. DOI: 10.1121/1.3056564.

Hudde, H. and Engel, A. (1998a). "Measuring and Modeling Basic Properties of the Human Middle Ear and Ear Canal. Part I: Model Structure and Measuring Techniques". In: *Acta Acust. united Ac.* 84.4, pp. 720–738.

— (1998b). "Measuring and Modeling Basic Properties of the Human Middle Ear and Ear Canal. Part II: Ear Canal, Middle Ear Cavities, Eardrum, and Ossicles". In: *Acta Acust. united Ac.* 84.5, pp. 894–913.

— (1998c). "Measuring and Modeling Basic Properties of the Human Middle Ear and Ear Canal. Part III: Eardrum Impedances, Transfer Functions and Model Calculations". In: *Acta Acust. united Ac.* 84.6, pp. 1091–1108.

Hudde, H. and Schmidt, S. (2009). "Sound Fields in Generally Shaped Curved Ear Canals". In: *J. Acoust. Soc. Am.* 125.5, pp. 3146–3157. DOI: 10.1121/1.3097446.

IEC 61260-1 (2014). *IEC 61260-1:2014, Electroacoustics – Octave-band and Fractional-Octave-Band Filters – Part 1: Specifications.*

ISO 8253-1 (2010). *ISO 8253-1:2010, Acoustics - Audiometric Test Methods - Part 1: Pure-tone Air and Bone Conduction Audiometry.* URL: https://www.iso.org/standard/43601.html.

Kapuria, S., Steele, C., and Puria, S. (2017). "Unraveling the Mystery of Hearing in Gerbil and Other Rodents with an Arch-Beam Model of the Basilar Membrane". In: *Sci. Rep.* 7.1. DOI: 10.1038/s41598-017-00114-x.

Kerkhofs, L., Starovoyt, A., Wouters, J., Putzeys, T., and Verhaert, N. (2023). "Optical Coherence Tomography-Based Atlas of the Human Cochlear Hook Region". In: *J. Clin. Med.* 12.1 (1), p. 238. DOI: 10.3390/jcm12010238.

Kersten, S., Sgard, F., and Vorländer, M. (2024a). "Impact of the Ear Canal Motion on the Impedance Boundary Conditions in Models of the Occlusion Effect". In: *J. Acoust. Soc. Am.* 155.1, pp. 56–67. DOI: 10.1121/10.0024244.

Kersten, S., Taschke, H., and Vorländer, M. (2024b). "Influence of the Cochlear Partition's Flexibility on the Macro Mechanisms in the Inner Ear". In: *Hear. Res.* 453, p. 109127. DOI: 10.1016/j.heares.2024.109127.

Kersten, S., Taschke, H., and Vorländer, M. (2025). "Finite Element Analysis of the Osseous Spiral Lamina's Influence on Inner Ear Fluid Flow during Bone Conduction Stimulation". In: *Hear. Res.* 459, p. 109205. DOI: 10.1016/j.heares.2025.109205.

Kim, N., Homma, K., and Puria, S. (2011). "Inertial Bone Conduction: Symmetric and Anti-Symmetric Components". In: *J. Assoc. Res. Otolaryngol.* 12.3, pp. 261–279. DOI: 10.1007/s10162-011-0258-3.

Kim, N., Steele, C. R., and Puria, S. (2014). "The Importance of the Hook Region of the Cochlea for Bone-Conduction Hearing". In: *Biophys. J.* 107.1, pp. 233–241. DOI: 10.1016/j.bpj.2014.04.052.

Koch, M., Eßinger, T. M., Maier, H., Sim, J. H., Ren, L., Greene, N. T., Zahnert, T., Neudert, M., and Bornitz, M. (2022). "Methods and Reference Data for Middle Ear Transfer Functions". In: *Sci. Rep.* 12.1, p. 17241. DOI: 10.1038/s41598-022-21245-w.

Kohllöffel, L. (1983). "Problems in Aural Sound Conduction". In: *Mechanics of Hearing: Proceedings of the IUTAM/ICA Symposium.* Ed. by E. de Boer and M. A. Viergever. The Hague ; Boston : Delft: Martinus Nijhoff ; Delft University Press, pp. 211–217.

Koike, T., Sakamoto, C., Sakashita, T., Hayashi, K., Kanzaki, S., and Ogawa, K. (2012). "Effects of a Perilymphatic Fistula on the Passive Vibration Response of the Basilar Membrane". In: *Hear. Res.* 283.1, pp. 117–125. DOI: 10.1016/j.heares.2011.10.006.

Kompis, M. and Caversaccio, M.-D. (2011). *Implantable Bone Conduction Hearing Aids.* Vol. 71. Advances in Oto-Rhino-Laryngology. Basel: Karger Medical and Scientific Publishers.

Kringlebotn, M. (1995). "The Equality of Volume Displacements in the Inner Ear Windows". In: *J. Acoust. Soc. Am.* 98.1, pp. 192–196. DOI: 10.1121/1.413746.

Kuk, F., Keenan, D., and Lau, C.-c. (2009). "Comparison of Vent Effects between a Solid Earmold and a Hollow Earmold". In: *J. Am. Acad. Audiol.* 20.8, pp. 480–491. DOI: 10.3766/jaaa.20.8.3.

Lampton, M. (1978). "Transmission Matrices in Electroacoustics". In: *Acustica* 39.4, pp. 239–251.

Li, P. M. M. C., Wang, H., Northrop, C., Merchant, S. N., and Nadol, J. B. (2007). "Anatomy of the Round Window and Hook Region of the Cochlea With Implications for Cochlear Implantation and Other Endocochlear Surgical Procedures". In: *Otol. Neurotol.* 28.5, pp. 641–648. DOI: 10.1097/mao.0b013e3180577949.

Liebich, S., Jax, P., and Vary, P. (2016). "Active Cancellation of the Occlusion Effect in Hearing Aids by Time Invariant Robust Feedback". In: *Speech Communication; 12. ITG Symposium.* VDE, pp. 1–5.

Lim, J., Dobrev, I., and Kim, N. (2023). "Reference Velocity of a Human Head in Bone Conduction Hearing: Finite Element Study". In: *Hear. Res.* 429. DOI: 10.1016/j.heares.2023.108699.

Lim, J., Dobrev, I., Röösli, C., Stenfelt, S., and Kim, N. (2022). "Development of a Finite Element Model of a Human Head Including Auditory Periphery for Understanding of Bone-Conducted Hearing". In: *Hear. Res.* 421. DOI: 10.1016/j.heares.2021.108337.

Lim, J., Kim, N., and Yoon, Y.-J. (2024). "Exploring the Impact of Force Direction and Phase on Bone Conduction Hearing with Bone Conduction Actuator". In: *Hear. Res.*, p. 109164. DOI: 10.1016/j.heares.2024.109164.

Liu, W., Atturo, F., Aldaya, R., Santi, P., Cureoglu, S., Obwegeser, S., Glueckert, R., Pfaller, K., Schrott-Fischer, A., and Rask-Andersen, H. (2015). "Macromolecular Organization and Fine Structure of the Human Basilar Membrane - RELEVANCE for Cochlear Implantation". In: *Cell Tissue Res.* 360.2, pp. 245–262. DOI: 10.1007/s00441-014-2098-z.

Lynch, T. J., Nedzelnitsky, V., and Peake, W. T. (1982). "Input Impedance of the Cochlea in Cat". In: *J. Acoust. Soc. Am.* 72.1, pp. 108–130. DOI: 10.1121/1.387995.

Marburg, S. and Anderssohn, R. (2011). "Fluid Structure Interaction and Admittance Boundary Conditions: Setup of an Analytical Example". In: *J. Comp. Acous.* 19.01, pp. 63–74. DOI: 10.1142/S0218396X11004274.

Mattingly, J. K., Banakis Hartl, R. M., Jenkins, H. A., Tollin, D. J., Cass, S. P., and Greene, N. T. (2020). "A Comparison of Intracochlear Pressures During Ipsilateral and Contralateral Stimulation With a Bone Conduction Implant". In: *Ear. Hear.* 41.2, pp. 312–322. DOI: 10.1097/AUD.0000000000000758.

McCormack, A. and Fortnum, H. (2013). "Why Do People Fitted with Hearing Aids Not Wear Them?" In: *Int. J. Audiol.* 52.5, pp. 360–368. DOI: 10.3109/14992027.2013.769066.

Meenderink, S. W. F., Shera, C. A., Valero, M. D., Liberman, M. C., and Abdala, C. (2019). "Morphological Immaturity of the Neonatal Organ of Corti and Associated Structures in Humans". In: *J. Assoc. Res. Otolaryngol.* 20.5, pp. 461–474. DOI: 10.1007/s10162-019-00734-2.

Mejia, J., Dillon, H., and Fisher, M. (2008). "Active Cancellation of Occlusion: An Electronic Vent for Hearing Aids and Hearing Protectors". In: *J. Acoust. Soc. Am.* 124.1, pp. 235–240. DOI: 10.1121/1.2908279.

Merchant, S. N., Ravicz, M. E., and Rosowski, J. J. (1996). "Acoustic Input Impedance of the Stapes and Cochlea in Human Temporal Bones". In: *Hear. Res.* 97.1, pp. 30–45. DOI: 10.1016/S0378-5955(96)80005-0.

Motallebzadeh, H. and Puria, S. (2021). "Mouse Middle-Ear Forward and Reverse Acoustics". In: *J. Acoust. Soc. Am.* 149.4, pp. 2711–2731. DOI: 10.1121/10.0004218.

Motallebzadeh, H., Soons, J. A. M., and Puria, S. (2018). "Cochlear Amplification and Tuning Depend on the Cellular Arrangement within the Organ of Corti". In: *Proceedings of the National Academy of Sciences* 115.22, pp. 5762–5767. DOI: 10.1073/pnas.1720979115.

Naidu, R. C. and Mountain, D. C. (1998). "Measurements of the Stiffness Map Challenge a Basic Tenet of Cochlear Theories". In: *Hear. Res.* 124.1, pp. 124–131. DOI: 10.1016/S0378-5955(98)00133-6.

Nakajima, H. H., Dong, W., Olson, E. S., Merchant, S. N., Ravicz, M. E., and Rosowski, J. J. (2009). "Differential Intracochlear Sound Pressure Measurements in Normal Human Temporal Bones". In: *J. Assoc. Res. Otolaryngol.* 10.1, pp. 23–36. DOI: 10.1007/s10162-008-0150-y.

Olson, E. S. (1998). "Observing Middle and Inner Ear Mechanics with Novel Intracochlear Pressure Sensors". In: *J. Acoust. Soc. Am.* 103.6, pp. 3445–3463. DOI: 10.1121/1.423083.

— (1999). "Direct Measurement of Intra-Cochlear Pressure Waves". In: *Nature* 402.6761, pp. 526–529. DOI: 10.1038/990092.

Olson, E. S., Duifhuis, H., and Steele, C. R. (2012). "Von Békésy and Cochlear Mechanics". In: *Hear. Res.* "Good Vibrations" A Special Issue to Honor the 50 Year Jubilee for Georg von Békésy´s Nobel Prize "The Physical Mechanisms of Stimulation within the Cochlea" 293.1, pp. 31–43. DOI: 10.1016/j.heares.2012.04.017.

Pörschmann, C. (2000). "Influences of Bone Conduction and Air Conduction on the Sound of One's Own Voice". In: *Acta Acust. united Ac.* 86.6, pp. 1038–1045.

Puria, S. (2003). "Measurements of Human Middle Ear Forward and Reverse Acoustics: Implications for Otoacoustic Emissions". In: *J. Acoust. Soc. Am.* 113.5, pp. 2773–2789. DOI: 10.1121/1.1564018.

Puria, S., Peake, W. T., and Rosowski, J. J. (1997). "Sound-Pressure Measurements in the Cochlear Vestibule of Human-Cadaver Ears". In: *J. Acoust. Soc. Am.* 101.5, pp. 2754–2770. DOI: 10.1121/1.418563.

Rabbitt, R. D. and Holmes, M. H. (1988). "Three-dimensional Acoustic Waves in the Ear Canal and Their Interaction with the Tympanic Membrane". In: *J. Acoust. Soc. Am.* 83.3, pp. 1064–1080. DOI: 10.1121/1.396051.

Raufer, S., Guinan, J. J., and Nakajima, H. H. (2019). "Cochlear Partition Anatomy and Motion in Humans Differ from the Classic View of Mammals". In: *Proc. Natl. Acad. Sci. U.S.A.* 116.28, pp. 13977–13982. DOI: 10.1073/pnas.1900787116.

Raufer, S., Idoff, C., Zosuls, A., Marino, G., Blanke, N., Bigio, I. J., O'Malley, J. T., Burgess, B. J., Nadol, J. B., Guinan, J. J., and Nakajima, H. H. (2020). "Anatomy of the Human Osseous Spiral Lamina and Cochlear Partition Bridge: Relevance for Cochlear Partition Motion". In: *J. Assoc. Res. Otolaryngol.* 21.2, pp. 171–182. DOI: 10.1007/s10162-020-00748-1.

Ravicz, M. E., Cheng, J. T., and Rosowski, J. J. (2019). "Sound Pressure Distribution within Human Ear Canals: II. Reverse Mechanical Stimulation". In: *J. Acoust. Soc. Am.* 145.3, p. 1569. DOI: 10.1121/1.5094776.

Reinfeldt, S., Stenfelt, S., and Håkansson, B. (2013). "Estimation of Bone Conduction Skull Transmission by Hearing Thresholds and Ear-Canal Sound Pressure". In: *Hear. Res.* 299, pp. 19–28. DOI: 10.1016/j.heares.2013.01.023.

Ren, L.-J., Hua, C., Ding, G.-H., Yang, L., Dai, P.-D., and Zhang, T.-Y. (2018). "Three-Dimensional Finite Element Hydrodynamical Modeling of Straight and Spiral Cochlea". In: *AIP Conf. Proc.* 1965.1, p. 030003. DOI: 10.1063/1.5038456.

Ren, L.-J., Yu, Y., Fang, Y.-Q., Hua, C., Dai, P.-D., and Zhang, T.-Y. (2021). "Finite Element Simulation of Cochlear Traveling Wave under Air and Bone Conduction Hearing". In: *Biomech. Model. Mechanobiol.* 20.4, pp. 1251–1265. DOI: 10.1007/s10237-021-01443-7.

Robles, L. and Ruggero, M. A. (2001). "Mechanics of the Mammalian Cochlea". In: *Physiol. Rev.* 81.3, pp. 1305–1352. DOI: 10.1152/physrev.2001.81.3.1305.

Rosowski, J. J., Bowers, P., and Nakajima, H. H. (2018). "Limits on Normal Cochlear 'Third' Windows Provided by Previous Investigations of Additional Sound Paths into and out of the Cat Inner Ear". In: *Hear. Res.* Computational Models of the Auditory System 360, pp. 3–13. DOI: 10.1016/j.heares.2017.11.003.

Rosowski, J. J., Cheng, J. T., Ravicz, M. E., Hulli, N., Hernandez-Montes, M., Harrington, E., and Furlong, C. (2009). "Computer-Assisted Time-Averaged Holograms of the Motion of the Surface of the Mammalian Tympanic Membrane with Sound Stimuli of 0.4–25kHz". In: *Hear. Res.* 253.1, pp. 83–96. DOI: 10.1016/j.heares.2009.03.010.

Saint-Gaudens, H., Nélisse, H., Sgard, F., and Doutres, O. (2022). "Towards a Practical Methodology for Assessment of the Objective Occlusion Effect Induced by Earplugs". In: *J. Acoust. Soc. Am.* 151.6, pp. 4086–4100. DOI: 10.1121/10.0011696.

Schroeter, J. and Poesselt, C. (1986). "The Use of Acoustical Test Fixtures for the Measurement of Hearing Protector Attenuation. Part II: Modeling the External Ear, Simulating Bone Conduction, and Comparing Test Fixture and Real-ear Data". In: *J. Acoust. Soc. Am.* 80.2, pp. 505–527. DOI: 10.1121/1.394046.

Shaw, E. A. G. and Stinson, M. R. (1983). "The Human External and Middle Ear: Models and Concepts". In: *Mechanics of Hearing.* Ed. by E. de Boer and M. A. Viergever. Dordrecht, Netherlands: Springer, pp. 3–10. DOI: 10.1007/978-94-009-6911-7_1.

Sohmer, H. and Freeman, S. (2004). "Further Evidence for a Fluid Pathway during Bone Conduction Auditory Stimulation". In: *Hear. Res.* 193.1, pp. 105–110. DOI: 10.1016/j.heares.2004.03.015.

Stenfelt, S. (2015). "Inner Ear Contribution to Bone Conduction Hearing in the Human". In: *Hear. Res.* 329, pp. 41–51. DOI: 10.1016/j.heares.2014.12.003.

— (2016). "Model Predictions for Bone Conduction Perception in the Human". In: *Hear. Res.* 340, pp. 135–143. DOI: 10.1016/j.heares.2015.10.014.

— (2020). "Investigation of Mechanisms in Bone Conduction Hyperacusis with Third Window Pathologies Based on Model Predictions". In: *Front. Neurol.* 11. DOI: 10.3389/fneur.2020.00966.

Stenfelt, S. and Goode, R. L. (2005a). "Bone-Conducted Sound: Physiological and Clinical Aspects". In: *Otol. Neurotol.* 26.6, pp. 1245–1261. DOI: 10.1097/01.mao.0000187236.10842.d5.

Stenfelt, S. and Goode, R. L. (2005b). "Transmission Properties of Bone Conducted Sound: Measurements in Cadaver Heads". In: *J. Acoust. Soc. Am.* 118.4, pp. 2373–2391. DOI: 10.1121/1.2005847.

Stenfelt, S., Hato, N., and Goode, R. L. (2002). "Factors Contributing to Bone Conduction: The Middle Ear". In: *J. Acoust. Soc. Am.* 111.2, pp. 947–959. DOI: 10.1121/1.1432977.

— (2004a). "Fluid Volume Displacement at the Oval and Round Windows with Air and Bone Conduction Stimulation". In: *J. Acoust. Soc. Am.* 115.2, pp. 797–812. DOI: 10.1121/1.1639903.

— (2004b). "Round Window Membrane Motion with Air Conduction and Bone Conduction Stimulation". In: *Hear. Res.* 198.1, pp. 10–24. DOI: 10.1016/j.heares.2004.07.008.

Stenfelt, S., Puria, S., Hato, N., and Goode, R. L. (2003a). "Basilar Membrane and Osseous Spiral Lamina Motion in Human Cadavers with Air and Bone Conduction Stimuli". In: *Hear. Res.* 181.1, pp. 131–143. DOI: 10.1016/S0378-5955(03)00183-7.

Stenfelt, S. and Reinfeldt, S. (2007). "A Model of the Occlusion Effect with Bone-Conducted Stimulation". In: *Int. J. Audiol.* 46.10, pp. 595–608. DOI: 10.1080/14992020701545880.

Stenfelt, S., Wild, T., Hato, N., and Goode, R. L. (2003b). "Factors Contributing to Bone Conduction: The Outer Ear". In: *J. Acoust. Soc. Am.* 113.2, pp. 902–913. DOI: 10.1121/1.1534606.

Stieger, C., Guan, X., Farahmand, R. B., Page, B. F., Merchant, J. P., Abur, D., and Nakajima, H. H. (2018). "Intracochlear Sound Pressure Measurements in Normal Human Temporal Bones During Bone Conduction Stimulation". In: *J. Assoc. Res. Otolaryngol.* 19.5, pp. 523–539. DOI: 10.1007/s10162-018-00684-1.

Stieger, C., Rosowski, J. J., and Nakajima, H. H. (2013). "Comparison of Forward (Ear-Canal) and Reverse (Round-Window) Sound Stimulation of the Cochlea". In: *Hear. Res.* MEMRO 2012 – Middle-Ear Bridge between Science and Otology 301, pp. 105–114. DOI: 10.1016/j.heares.2012.11.005.

Stinson, M. R. (1985). "The Spatial Distribution of Sound Pressure within Scaled Replicas of the Human Ear Canal". In: *J. Acoust. Soc. Am.* 78.5, pp. 1596–1602. DOI: 10.1121/1.392797.

Stinson, M. R. and Lawton, B. W. (1989). "Specification of the Geometry of the Human Ear Canal for the Prediction of Sound-pressure Level Distribution". In: *J. Acoust. Soc. Am.* 85.6, pp. 2492–2503. DOI: 10.1121/1.397744.

Stinson, M. R., Shaw, E. A. G., and Lawton, B. W. (1982). "Estimation of Acoustical Energy Reflectance at the Eardrum from Measurements of Pressure Distribution in the Human Ear Canal". In: *J. Acoust. Soc. Am.* 72.3, pp. 766–773. DOI: 10.1121/1.388257.

Surendran, S., Prodanovic, S., and Stenfelt, S. (2023). "Hearing Through Bone Conduction Headsets". In: *Trends in Hearing* 27, p. 23312165231168741. DOI: 10.1177/23312165231168741.

Surendran, S. and Stenfelt, S. (2021). "The Outer Ear Pathway during Hearing by Bone Conduction". In: *Hear. Res.* 421. DOI: 10.1016/j.heares.2021.108388.

Suzuki, S., Maruyama, S., and Ido, H. (1989). "Boundary Element Analysis of Cavity Noise Problems with Complicated Boundary Conditions". In: *J. Sound Vib.* 130.1, pp. 79–96. DOI: 10.1016/0022-460X(89)90521-X.

Taber, L. A. and Steele, C. R. (1981). "Cochlear Model Including Three-dimensional Fluid and Four Modes of Partition Flexibility". In: *J. Acoust. Soc. Am.* 70.2, pp. 426–436. DOI: 10.1121/1.386785.

Taschke, H. (2005). "Mechanismen Der Knochenschallleitung (Mechanisms of Bone-Conducted Sound)". Bochum, Germany: Ruhr University Bochum. DOI: 10.13154/294-10197.

Tonndorf, J. (1962). "Compressional Bone Conduction in Cochlear Models". In: *J. Acoust. Soc. Am.* 34.8, pp. 1127–1131. DOI: 10.1121/1.1918259.

— (1966). "Synopsis a Revised Theory of Bone Conduction". In: *Acta Oto-Laryngol.* 61 (sup213), pp. 7–9. DOI: 10.3109/00016486609120796.

— (1968). "A New Concept of Bone Conduction". In: *Arch. Otolaryngol.* 87.6, pp. 595–600. DOI: 10.1001/archotol.1968.00760060597008.

Tonndorf, J. and Khanna, S. M. (1972). "Tympanic-Membrane Vibrations in Human Cadaver Ears Studied by Time-Averaged Holography". In: *J. Acoust. Soc. Am.* 52 (4B), pp. 1221–1233. DOI: 10.1121/1.1913236.

Wang, J., Stenfelt, S., Wu, S., Yan, Z., Sang, J., Zheng, C., and Li, X. (2022). "The Effect of Stimulation Position and Ear Canal Occlusion on Perception of Bone Conducted Sound". In: *Trends Hear.* 26, pp. 1–15. DOI: 10.1177/23312165221130185.

Wang, X., Wang, L., Zhou, J., and Hu, Y. (2014). "Finite Element Modelling of Human Auditory Periphery Including a Feed-Forward Amplification of the Cochlea". In: *Comput. methods Biomech. Biomed. Eng.* 17.10, pp. 1096–1107. DOI: 10.1080/10255842.2012.737458.

Wang, Y., Steele, C. R., and Puria, S. (2016). "Cochlear Outer-Hair-Cell Power Generation and Viscous Fluid Loss". In: *Sci. Rep.* 6.1, p. 19475. DOI: 10.1038/srep19475.

Wheatstone, C. (1827). "Experiments on Audition". In: *Q. J. Sci.*

Winkler, A., Latzel, M., and Holube, I. (2016). "Open Versus Closed Hearing-Aid Fittings: A Literature Review of Both Fitting Approaches". In: *Trends Hear.* 20, pp. 1–13. DOI: 10.1177/2331216516631741.

World Report on Hearing (2021). Geneva: World Health Organization.

Wright, C. G. and Roland, P. S. (2018). "Anatomy of the Helicotrema and Cochlear Apex". In: *Cochlear Anatomy via Microdissection with Clinical Implications: An*

Atlas. Ed. by C. G. Wright and P. S. Roland. Springer International Publishing, pp. 27–43. DOI: 10.1007/978-3-319-71222-2_2.

Xu, H., Sgard, F., Carillo, K., Wagnac, É., and de Guise, J. (2021). "Simulation of the Objective Occlusion Effect Induced by Bone-Conducted Stimulation Using a Three-Dimensional Finite-Element Model of a Human Head". In: *J. Acoust. Soc. Am.* 150.5, pp. 4018–4030. DOI: 10.1121/10.0007230.

Yang, L., Werf, K. O. van der, Fitié, C. F. C., Bennink, M. L., Dijkstra, P. J., and Feijen, J. (2008). "Mechanical Properties of Native and Cross-linked Type I Collagen Fibrils". In: *Biophys. J.* 94.6, pp. 2204–2211. DOI: 10.1529/biophysj.107.111013.

Zenkert, D. (1995). *An Introduction to Sandwich Structures*. URL: https://urn.kb.se/resolve?urn=urn:nbn:se:kth:diva-263054.

Zhao, M., Fridberger, A., and Stenfelt, S. (2021). "Vibration Direction Sensitivity of the Cochlea with Bone Conduction Stimulation in Guinea Pigs". In: *Sci. Rep.* 11.1 (1), p. 2855. DOI: 10.1038/s41598-021-82268-3.

Zurbrügg, T., Stirnemannn, A., Kuster, M., and Lissek, H. (2015). "Objective and Subjective Validation of an Active Control Approach to Reduce the Occlusion Effect in Hearing Aids". In: *Acta Acust. united Ac.* 101.3, pp. 502–509. DOI: 10.3813/AAA.918847.

Zurbrügg, T., Stirnemannn, A., Kuster, M., and Lissek, H. (2014). "Investigations on the Physical Factors Influencing the Ear Canal Occlusion Effect Caused by Hearing Aids". In: *Acta Acust. united Ac.* 100.3, pp. 527–536.

Zweig, G., Lipes, R., and Pierce, J. R. (1976). "The Cochlear Compromise". In: *J. Acoust. Soc. Am.* 59.4, pp. 975–982. DOI: 10.1121/1.380956.

Zwislocki, J. (1950). "Theory of the Acoustical Action of the Cochlea". In: *J. Acoust. Soc. Am.* 22.6, pp. 778–784. DOI: 10.1121/1.1906689.

— (1962). "Analysis of the Middle-Ear Function. Part I: Input Impedance". In: *J. Acoust. Soc. Am.* 34 (9B), pp. 1514–1523. DOI: 10.1121/1.1918382.

Curriculum Vitae

Personal Data

| | Simon Kersten |
| July 13, 1994 | born in Goch, Germany |

Education

August 1, 2025	Doctoral Examination for Dr.-Ing., Faculty of Electrical Engineering and Information Technology, RWTH Aachen University, Germany
10/2017 – 06/2020	M.Sc. Electrical Engineering, Information Technology and Computer Engineering, RWTH Aachen University, Germany
09/2014 – 07/2017	B.Eng. Electrical Engineering, FH Aachen University of Applied Sciences, Germany
06/2013	General Higher Education Entrance Qualification (Abitur), Städtisches Gymnasium Goch, Germany

Work Experience

07/2020 – today	Research assistant, Institute for Hearing Technology and Acoustics, RWTH Aachen University, Germany
09/2023 – 12/2023	Guest researcher, École de Technologie Supérieure, Montréal, Canada
04/2019 – 09/2019	Intern, Sennheiser electronic GmbH & Co. KG, Wedemark, Germany
01/2016 – 03/2019	Student assistant, FH Aachen University of Applied Sciences and Institute of Technical Acoustics, RWTH Aachen University, Germany
01/2014 – 07/2014	Employment, Brauner Microphones, Rees, Germany

September 8, 2025

Publications

Journal articles

Kersten, S., Taschke, H., and Vorländer, M. (2025). "Finite Element Analysis of the Osseous Spiral Lamina's Influence on Inner Ear Fluid Flow during Bone Conduction Stimulation". In: *Hear. Res.* 459, p. 109205. DOI: 10.1016/j.heares.2025.109205.

Kersten, S., Sgard, F., and Vorländer, M. (2024a). "Impact of the Ear Canal Motion on the Impedance Boundary Conditions in Models of the Occlusion Effect". In: *J. Acoust. Soc. Am.* 155.1, pp. 56–67. DOI: 10.1121/10.0024244.

Kersten, S., Taschke, H., and Vorländer, M. (2024b). "Influence of the Cochlear Partition's Flexibility on the Macro Mechanisms in the Inner Ear". In: *Hear. Res.* 453, p. 109127. DOI: 10.1016/j.heares.2024.109127.

Conference papers

Brinkmann, F., Berzborn, M., Heimes, A., Hoyer, A., Karakonstantis, X., Kersten, S., Lübeck, T., Palenda, P., Andrade, C., Arend, J. M., Hahn, N., Jüterbock, T., Meyer-Kahlen, N., Paskiewicz, A., Schlecht, S. J., Schultz, F., and Weinzierl, S. (2025). "Open Educational Resources for Acoustics and Audio Signal Processing Using Jupyter Notebooks and Pyfar". In: *Forum Acusticum / Euronoise 2025*. Forum Acusticum / Euronoise 2025 – 11th Convention of the European Acoustics Association. Málaga, Spain.

Kersten, S. and Vorländer, M. (2025). "Physical Mechanisms Underlying the Occlusion Effect". In: *DAS/DAGA 2025*. DAS|DAGA 2025 – 51st Annual Meeting on Acoustics. Copenhagen, Denmark. DOI: 10.71568/dasdaga2025.015.

Maeder, M., Buba, M., Dogu, M., Bárány, M. T., Breitkreutz, T., Heggemann, L., Roca Paz, L. E., Kersten, S., and Schmid, J. D. (2025). "Interactive Simulation Apps for Teaching Acoustical Phenomena and Vibration Effects". In: *Forum Acusticum / Euronoise 2025*. Forum Acusticum / Euronoise 2025 – 11th Convention of the European Acoustics Association. Málaga, Spain.

Rehman, R., Kersten, S., and Fels, J. (2025). "An Experimental Setup for the Estimation and Emulation of Bone and Air Conducted Components of One's Own Voice". In: *DAS/DAGA 2025*. DAS|DAGA 2025 – 51st Annual Meeting on Acoustics. Copenhagen, Denmark. DOI: 10.71568/dasdaga2025.201.

Sgard, F., Carillo, K., Kersten, S., Richert, R., and Doutres, O. (2025). "Virtual and Experimental Acoustic Comfort Testers for Earplugs". In: *Forum Acusticum /*

Euronoise 2025. Forum Acusticum / Euronoise 2025 – 11th Convention of the European Acoustics Association. Málaga, Spain.

Buba, M., Kersten, S., Schmid, J. D., Barany, M., Breitkreutz, T., Dogu, M., Heggemann, Y., and Roca Paz, L. E. (2024). "Kooperationsprojekt der jungen DEGA: Entwicklung interaktiver Akustik-Apps für die Lehre in der Akustik". In: *Fortschritte der Akustik - DAGA 2024*. DAGA 2024 - 50. Jahrestagung für Akustik. Hannover, Germany.

Kersten, S. and Vorländer, M. (2021). "FEM-Simulation of bone conduction in the human head: Influence of geometrical and material parameters". In: *Fortschritte der Akustik - DAGA 2021*. DAGA 2021 - 47. Jahrestagung für Akustik. Online/Wien, Austria.

Lamba, M., Kersten, S., Ewert, S. D., Vorländer, M., and Kollmeier, B. (2021). "Comparison of loudness perception mismatch with visual presentation of two anechoic rooms". In: *Fortschritte der Akustik - DAGA 2021*. DAGA 2021 - 47. Jahrestagung für Akustik. Online/Wien, Austria.

Oral presentations

Kersten, S. (2025). "Finite element analysis of the inner ear's vibroacoustic behavior". COMSOL Meeting an der RWTH Aachen (Aachen, Germany).

Kersten, S., Taschke, H., and Vorländer, M. (2025). "On the Sound Pressure Distribution in the Inner Ear during Bone Conduction Stimulation". 25th International Congress on Acoustics and 188th Meeting of the Acoustical Society of America (New Orleans, LA, USA).

Kersten, S., Sgard, F., and Vorländer, M. (2024a). "Impact of the ear canal motion on the occlusion effect for bone-conducted stimulation". DAGA 2024 - 50. Jahrestagung für Akustik (Hannover, Germany).

Kersten, S., Taschke, H., and Vorländer, M. (2024b). "Influence of the Osseous Spiral Lamina on the Inner Ear's Response to Air- and Bone-Conducted Stimulation". 187th Meeting of the Acoustical Society of America (Online).

Kersten, S. and Vorländer, M. (2024). "Decomposition of the vibroacoustic propagation through a fluid-structure coupling boundary". 29. DEGA-Workshop „Physikalische Akustik" (Bad Honnef, Germany).

Kersten, S., Möhlmann, C., and Vorländer, M. (2023a). "Finite Element Simulation of the Ear Canal Wall Vibrations". Acoustics Week in Canada (Montreal, QC, Canada).

Kersten, S., Taschke, H., and Vorländer, M. (2023b). "Directionality and Decomposition of the Bone Conduction Mechanisms at the Inner Ear". OSSEO 2023 8th International Congress on Bone Conduction and Related Technologies (Denver, CO, USA).

— (2023c). "Fluid motion and pressure distribution in the human inner rar during bone conduction hearing". DAGA 2023 - 49. Jahrestagung für Akustik (Hamburg, Germany).

Möhlmann, C., Kersten, S., and Vorländer, M. (2023). "Finite element simulation of the occlusion effect in the ear canal". DAGA 2023 - 49. Jahrestagung für Akustik (Hamburg, Germany).

Kersten, S., Taschke, H., and Vorländer, M. (2022a). "Finite Element Simulation of the Inner Ear Component in Bone Conduction Hearing". Hearing, Audio and Audiology Sciences Meeting 2022 (Southampton, UK).

— (2022b). "Finite-element simulation of bone conduction in the human head: The inner ear component". DAGA 2022 - 48. Jahrestagung für Akustik (Stuttgart, Germany).

Kersten, S. and Vorländer, M. (2022). "Influence of the Model Parameters for the Finite Element Simulation of Bone Conduction in the Human Head". 182nd Meeting of the Acoustical Society of America (Denver, CO, USA).

Lamba, M., Kersten, S., Ewert, S. D., Vorländer, M., and Kollmeier, B. (2022). "Does the loudness mismatch between free field and headphone depend on the visually presented scene?" DAGA 2022 - 48. Jahrestagung für Akustik (Stuttgart, Germany).

Salehi, M., Kersten, S., and Vorländer, M. (2022). "Equivalent circuit modelling of bone conduction hearing". DAGA 2022 - 48. Jahrestagung für Akustik (Stuttgart, Germany).

Poster presentations

Lamba, M., Kersten, S., Ewert, S. D., Vorländer, M., and Kollmeier, B. (2025). "Perceived Level Differences at Equal Loudness in Headphone-Based Comparisons of Virtual Room Acoustics and Diotic Stimuli". DAS|DAGA 2025 – 51st Annual Meeting on Acoustics (Copenhagen, Denmark).

Ohlmann, K., Kersten, S., Vorländer, M., and Kollmeier, B. (2025). "Perceptual Estimation of the Bone Conduction Path for One's Own Voice". DAS|DAGA 2025 – 51st Annual Meeting on Acoustics (Copenhagen, Denmark).

Berzborn, M., Brinkmann, F., Kersten, S., and Jurgeit, K.-P. (2021). "pyfar: Python packages for acoustics research". DAGA 2021 - 47. Jahrestagung für Akustik (Online/Wien, Austria).

Acknowledgements

This work cannot be viewed in isolation from the context in which it was created.

This work would not have been possible without Michael Vorländer. I am deeply grateful to Michael for giving me the freedom to pursue my research interests while providing me with unconditional support and advice whenever I needed it.

Michael also enabled me to work in the HAPPAA research project (funded by the Deutsche Forschungsgemeinschaft (DFG, German Research Foundation) – Project-ID 352015383 – SFB 1330 A4, https://uol.de/sfb1330). The project was far more than a source of funding. I greatly enjoyed the collaboration and learned a lot from the exchange. In particular, I would like to thank the A4 team members Birger Kollmeier, Kristin Ohlmann, and Manan Lamba.

Without Henning Taschke, this work would not have been possible either. In my opinion, his PhD work on numerical modeling of bone conduction hearing, completed about 20 years ago (Taschke, 2005), remains unmatched. When we first got in contact, I asked him for a PDF of his thesis. Not only did he send the file, but he also shared all his data, accompanied by the modest comment: "Vielleicht – so sagen wir bei Volkswagen – erhöht es die Absprungbasis." As if that weren't enough, Henning also became an invaluable discussion partner. We spent many hours of his free time debating the relationship between boundary impedances and vibrations – a concept central to this thesis (and on which Henning was, from the start, absolutely right). Most importantly, he offered all this without any personal gain, making him a true role model for scientific exchange. It is an honor to have met Henning, and I am deeply grateful for his contributions to this work.

Sometimes you just need the right input at the right time. At a DAGA conference, Bastian Epp gave me perhaps the most fundamental criticism of my work in recent years. This feedback proved very valuable and ultimately led to the detailed inner ear investigations presented here. I am pleased that Bastian agreed to serve as an examiner for this thesis, and I am grateful for his support as an attentive and thoughtful contact person in all aspects of research.

Speaking of right input at the right time and the importance of scientific exchange: I would like to thank Kévin Carillo, Franck Sgard, Olivier Doutres

and all the other fantastic people I met in Montréal. I consider my three months in Canada in 2023 to be the most exciting part of my PhD – a time when I grew up as a researcher.

As important as the work itself is, it is just as important that it is enjoyable. The last few years would not have been as much fun without all my friends, colleagues and students at the Institute for Hearing Technology and Acoustics, the pyfar family, and the many wonderful people I have worked with and met at conferences and workshops. I am grateful for being part of such a joyful and inspiring community.

Lastly, I would like to express my deepest gratitude.

I would like to thank my parents and my entire family for laying the foundations for who I am and what I do.

Karen, thank you for everything. Our love is my greatest joy and fortune, and it means everything to me.

The future is bright.